Advances in Mechanical Engineering

Advances in Additive Manufacturing Processes and Materials

Guest Editors: Dachamir Hotza, Cynthia M. Gomes, and Jens Günster

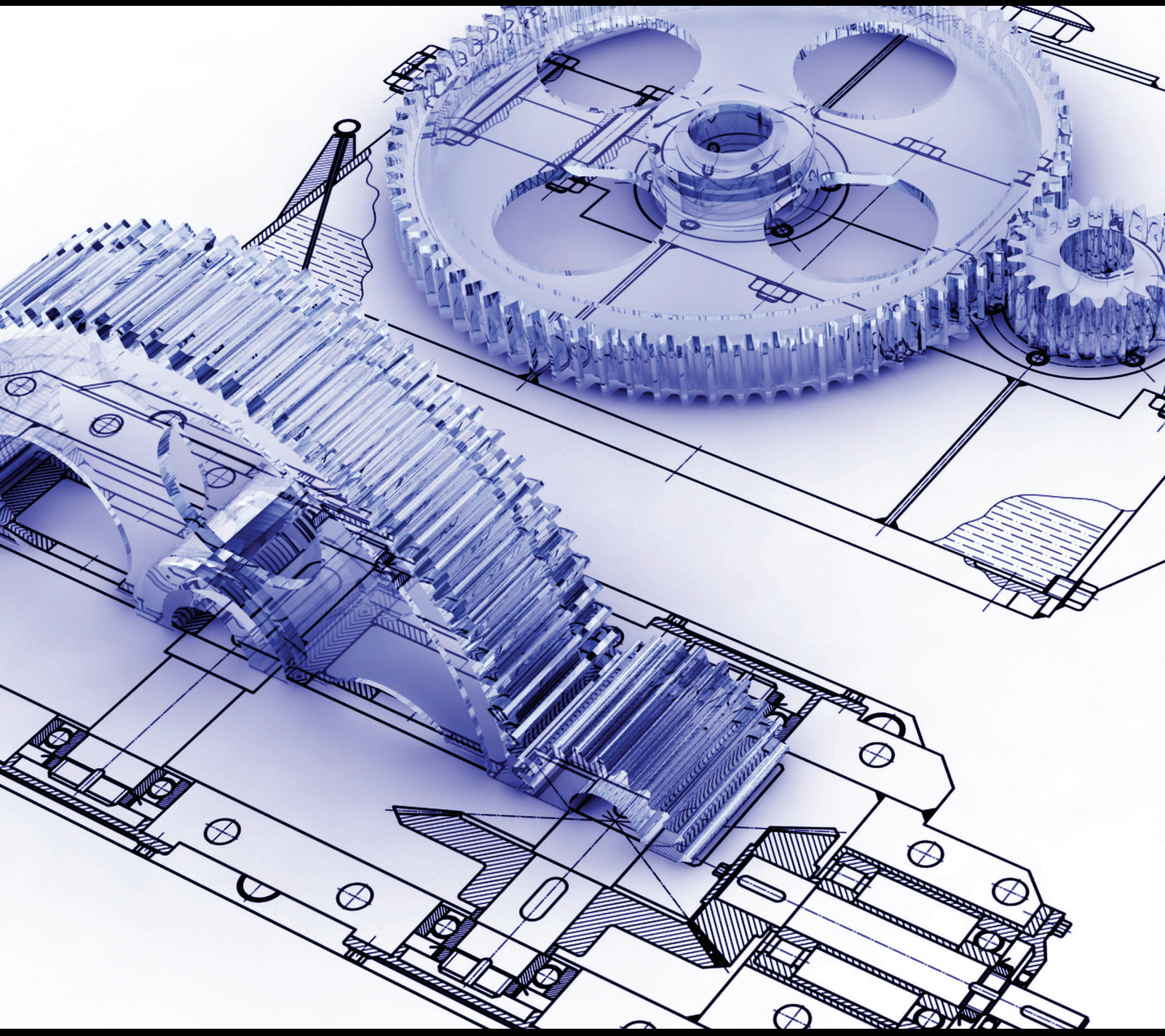

Advances in Additive Manufacturing Processes and Materials

Advances in Mechanical Engineering

Advances in Additive Manufacturing Processes and Materials

Guest Editors: Dachamir Hotza, Cynthia M. Gomes, and Jens Günster

Editorial Board

Contents

Advances in Additive Manufacturing Processes and Materials, Dachamir Hotza, Cynthia M. Gomes, and Jens Günster
Volume 2014, Article ID 645075, 1 page

Microstructural and Mechanical Characterization of a Custom-Built Implant Manufactured in Titanium Alloy by Direct Metal Laser Sintering, Maria Aparecida Larosa, André Luiz Jardini, Cecília Amélia de Carvalho Zavaglia, Paulo Kharmandayan, Davi Reis Calderoni, and Rubens Maciel Filho
Volume 2014, Article ID 945819, 8 pages

Manufacturing of Porous Polycaprolactone Prepared with Different Particle Sizes and Infrared Laser Sintering Conditions: Microstructure and Mechanical Properties, G. V. Salmoria, D. Hotza, P. Klauss, L. A. Kanis, and C. R. M. Roesler
Volume 2014, Article ID 640496, 7 pages

A Method to Characterize the Quality of a Polymer Laser Sintering Process, Stefan Rüsenberg, Stefan Josupeit, and Hans-Joachim Schmid
Volume 2014, Article ID 185374, 10 pages

Investigations on Temperature Fields during Laser Beam Melting by Means of Process Monitoring and Multiscale Process Modelling, J. Schilp, C. Seidel, H. Krauss, and J. Weirather
Volume 2014, Article ID 217584, 7 pages

Advanced Material Studies for Additive Manufacturing in terms of Future Gear Application, Jan Bräunig, Thomas Töppel, Bernhard Müller, Martin Burkhardt, Thomas Hipke, and Welf-Guntram Drossel
Volume 2014, Article ID 741083, 10 pages

Powder-Bed Stabilization for Powder-Based Additive Manufacturing, Andrea Zocca, Cynthia M. Gomes, Thomas Mühler, and Jens Günster
Volume 2014, Article ID 491581, 6 pages

Novel Prospects and Possibilities in Additive Manufacturing of Ceramics by means of Direct Inkjet Printing, Anja Mareike Wätjen, Philipp Gingter, Michael Kramer, and Rainer Telle
Volume 2014, Article ID 141346, 12 pages

Mathematical Model for the Selection of Processing Parameters in Selective Laser Sintering of Polymer Products, Ana Pilipović, Igor Drstvenšek, and Mladen Šercer
Volume 2014, Article ID 648562, 9 pages

Hindawi Publishing Corporation
Advances in Mechanical Engineering
Volume 2014, Article ID 645075, 1 page
http://dx.doi.org/10.1155/2014/645075

Editorial

Advances in Additive Manufacturing Processes and Materials

Dachamir Hotza,[1] Cynthia M. Gomes,[2] and Jens Günster[2]

[1] *Department of Chemical Engineering, Federal University of Santa Catarina (UFSC), 88040-900 Florianópolis, SC, Brazil*
[2] *Department of Materials Engineering, Federal Institute for Materials Research and Testing (BAM), Unter den Eichen 44-46, 12203 Berlin, Germany*

Correspondence should be addressed to Dachamir Hotza; dhotza@gmail.com

Received 28 September 2014; Accepted 28 September 2014; Published 21 December 2014

Additive manufacturing (AM), also known as rapid prototyping or 3D printing, generally refers to techniques that produce three-dimensional parts by adding material gradually in a layer by layer fashion. In this sense, AM differs fundamentally from forming and subtractive techniques. This special issue intends to put together research and developments in AM, particularly related to new manufacturing processes and/or to alternative feedstock materials and products. Polymer and metal-based raw materials and products have been extensively investigated in AM techniques. Recently, ceramic, glass, and composite materials have been additionally used both in commercial and in innovative AM processes. The material compositions and processing steps used for shaping or finishing the structure of AM products are responsible for final properties and performance. Recent advances in sensors, micromechanics, computational modelling, and simulation have enhanced AM technologies. As complex parts become easier to build and the equipment and skills needed to build them become more and more common, innovative approaches are achievable. Additionally, this evolution opens up new fields of application, moving it from being a prototyping tool to a final product manufacturing process (rapid manufacturing).

This special issue explores the development of new products and applications through AM processes. Selected investigations contributed to this issue with original research that analyze feedstock materials, process parameters, and their effects on mechanical, physical, and other properties in prototypes or customized parts fabricated by AM techniques.

The topics presented in this issue include diverse materials manufactured by representative AM processes, as summarized below:

(i) advanced ceramics by 3D Printing or Direct Inkjet Printing,

(ii) metals and alloys by Direct Metal Laser Sintering or Laser Beam Melting,

(iii) polymers by Selective Laser Sintering.

We hope that readers of Advances in Mechanical Engineering will find in this special issue not only accurate data and updated information on improvement of process steps and material systems for Additive Manufacturing, but also important questions addressed such as sustainability, affordability, and reliability issues.

Dachamir Hotza
Cynthia M. Gomes
Jens Günster

Hindawi Publishing Corporation
Advances in Mechanical Engineering
Volume 2014, Article ID 945819, 8 pages
http://dx.doi.org/10.1155/2014/945819

Research Article

Microstructural and Mechanical Characterization of a Custom-Built Implant Manufactured in Titanium Alloy by Direct Metal Laser Sintering

Maria Aparecida Larosa,[1,2] André Luiz Jardini,[1,2] Cecília Amélia de Carvalho Zavaglia,[1,3] Paulo Kharmandayan,[1,4] Davi Reis Calderoni,[1,4] and Rubens Maciel Filho[1,2]

[1] *Institute of Biofabrication (INCT-BIOFABRIS), 13083-852 Campinas, SP, Brazil*
[2] *School of Chemical Engineering, State University of Campinas, 13083-852 Campinas, SP, Brazil*
[3] *School of Mechanical Engineering, State University of Campinas, 13083-860 Campinas, SP, Brazil*
[4] *School of Medical Sciences, State University of Campinas, 13083-887 Campinas, SP, Brazil*

Correspondence should be addressed to Maria Aparecida Larosa; malarosa@gmail.com

Received 10 February 2014; Revised 23 June 2014; Accepted 8 July 2014; Published 26 August 2014

Academic Editor: Dachamir Hotza

Custom-built implants manufacture has always presented difficulties which result in high cost and complex fabrication, mainly due to patients' anatomical differences. The solution has been to produce prostheses with different sizes and use the one that best suits each patient. Additive manufacturing technology, incorporated into the medical field in the late 80's, has made it possible to obtain solid biomodels facilitating surgical procedures and reducing risks. Furthermore, this technology has been used to produce implants especially designed for a particular patient, with sizes, shapes, and mechanical properties optimized, for different areas of medicine such as craniomaxillofacial surgery. In this work, the microstructural and mechanical properties of Ti6Al4V samples produced by direct metal laser sintering (DMLS) are studied. The microstructural and mechanical characterizations have been made by optical and scanning electron microscopy, X-ray diffraction, and microhardness and tensile tests. Samples produced by DMLS have a microstructure constituted by hexagonal α' martensite with acicular morphology. An average microhardness of 370 HV was obtained and the tensile tests showed ultimate strength of 1172 MPa, yield strength of 957 MPa, and elongation at rupture of 11%.

1. Introduction

The malfunction or loss of total or partial functions of an organ or tissue, resulting from trauma or disease, is currently one of the most important and troubling public health problems affecting a significant number of people around the world. Annually in the US, the use of pins, plates, and screws for fixation of fractures reaches 1.5 million procedures and it is estimated that more than 500,000 joint replacement surgeries (hip and knee) are performed [1]. To meet the great demand for orthopedic surgical procedures to repair or replace body parts, it is necessary to develop biomaterials and more advanced surgical techniques.

The combination of high mechanical resistance, high toughness, manufacturing ease, good resistance to degradation by corrosion, and low cost makes some metallic materials the preferred biomaterials in the manufacture of orthopedic implants subjected to severe mechanical stresses within the human body.

Nowadays, pure titanium and its alloys are some of the most used metallic biomaterials in temporary or permanent orthopedic applications [2–5]. The temporary implants perform their function of fixing the fractures by a predetermined period, until the member is completely recovered so that the implant can be removed. The fixing plates, screws, wires, and intramedullary pins to repair broken bones are examples of temporary implants. The permanent implants replace body parts and need to play their role for the rest of the patient's life, such as the hip, knee, shoulder, elbow, or wrist prosthetics.

These implants, as well as other structural components, may fail due to mechanic fracture, wear, or corrosion. The combination of the electrochemical process of corrosion and

cyclical mechanical stress can speed up the release of particles and metal ions, leading to premature failure of the implant [1, 6]. As an example, the articulated implants that are exposed to high loads and severe wear due to the patient's movement can be mentioned. Moreover, the degradation of metallic implants inside the human body may not only impair the integrity of the material, but also generate biocompatibility problems such as infection or allergic reactions, leading to premature removal of the implant [7, 8]. The derived detritus are harmful to the tissues that are in contact with the implant and can be taken into the bloodstream, settling in organs and impairing their functions. Thus, the metallic biomaterials must have properties such as resistance to fatigue and wear, toughness to fracture, and mainly high corrosion resistance.

Titanium is particularly suitable for works in corrosive environments and for applications in which low density is essential. It has a high relation strength/weight, nonmagnetic properties, and high corrosion resistance due to the formation of a compact protective film on the metal surface, the titanium oxide (TiO_2). Due to its highly reactive nature in the presence of oxygen, the casting must be conducted in vacuum furnaces [1, 9].

Two types of crystalline formation can occur in titanium. The first one is called alpha and has a hexagonal close-packed (hcp) crystalline structure, while the second is termed beta with a body-centered cubic (bcc) crystalline structure. In pure titanium the alpha phase is stable at room temperature. The alloying elements are added to pure titanium and tend to modify the temperature at which the phase transformation occurs and the amount of each phase present. The alloying additions to titanium tend to stabilize the alpha or beta phase. The alpha phase is stabilized at higher temperatures, by elements called alpha stabilizers, as aluminum, tin, and zirconium, while the beta phase is stabilized by beta stabilizers at lower temperatures, as vanadium, molybdenum, niobium, chromium, iron, and manganese. There are three structural types of titanium alloys: alpha alloys (α), alpha-beta alloys ($\alpha + \beta$), and beta alloys (β) [10–14].

Among the titanium alloys, the most employed in the manufacture of surgical implants is Ti6Al4V. The standard that describes the requirements for this alloy is ASTM F136 [15]. The structure of this alloy is $\alpha + \beta$ type, in which the α phase stabilizing element is aluminum and the one in phase β is vanadium [16]. In the same way as other materials, this titanium alloy can be wrought, quenched, or annealed and can be machined by conventional means [17].

The marketed products for medical use must be strictly tested as far as their chemical composition and mechanical and structural features are concerned to ensure that they are in accordance with the standards established for implants such as ASTM F136 [15], ASTM F1798 [18], and ASTM F1800 [19] among others. The manufacture of metallic implant can include a series of procedures that depend on some factors such as shape and size of the final product, metal features, and manufacturing cost, among others. The methods employed are casting, machining, forging, and powder metallurgy. Usually, after the melting and mechanical forming of the material, an annealing thermal treatment is performed in order to relieve residual stresses, to make the material more ductile and tough, and to produce a specific microstructure [20].

Following the manufacturing step, the implant may be subjected to surface modification procedures and finishing as ionic implantation, nitriding, porous or microporous coating application, polishing, chemical cleaning, and passivation. The surface features of the implants are essential in their biological performance.

Additive manufacturing (AM) or rapid prototyping (RP) is a fabrication technique by the additive method, which is based on successive addition of flat layers of material. This technology allows the production of physical components (prototypes, models, molds, etc.) with information obtained directly from a three-dimensional geometric model CAD (Computer Aided Design) system. The process starts with the 3D computer model of the part, obtained by a CAD system, electronically sliced. From this slicing, 2D contour lines are obtained which will define, in each layer, where material is going to be added. These layers are sequentially processed, generating the physical part through stacking and adhesion of them, beginning at the bottom and going up to the top part [21, 22].

The construction of parts with complex geometry and in the most varied materials, the use of only one piece of equipment to build the part from the beginning to the end, and less time and cost to obtain prototypes are some advantages that rapid prototyping offers when compared to other manufacturing processes [23–25].

In the medicine field, additive manufacturing was integrated to digital imaging techniques of computed tomography (CT) and magnetic resonance (MR), making it possible to obtain solid biomodels that reproduce the anatomical structures of the body. The internal structures images, acquired by these techniques, are handled in a system for medical imaging. From these images, specific algorithms of segmentation are applied to the separation of the interest structure (bone or tissue). From these image data, a 3D model is generated on the specific computer software (InVesalius) and exported to be made by additive manufacturing, originating the biomodels (biomedical prototypes) [26, 27].

These biomodels can be used for surgical planning, didactic purposes, the diagnosis and treatment of patients, and communication between professionals and patients. As a result, the biomodels facilitate surgery and reduce infection and rejection risks, complications, and length of surgery [28–31]. Nowadays, the additive manufacturing allows also the design of customized prosthetic implants, suiting them directly to the patient's needs. It is possible to produce implants with optimized sizes, shapes, and mechanical properties. For this, digital information obtained from computed tomography and magnetic resonance is used, making it possible to obtain directly the final implant and reduce the manufacturing time.

The use of these integrated techniques for manufacture of custom implants offers a significant potential of cost savings for health systems as well as the possibility to provide a decent life for a huge number of people [32–34]. Additive manufacturing can be used by health professionals who work in orthopedics, neurosurgery, maxillofacial and orthognathic

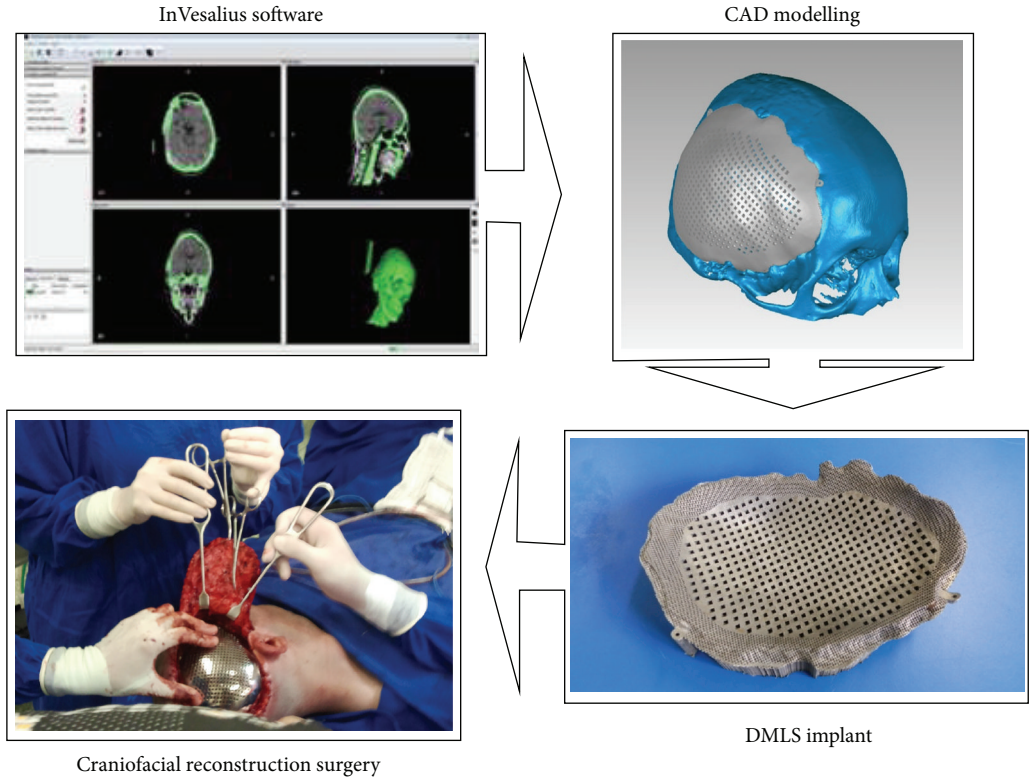

Figure 1: Application of additive manufacturing in craniofacial reconstruction surgery.

surgery, traumatology, craniofacial and plastic surgery, implant dentistry, and oncology, among others.

An application in the medical field to be considered is the bone reconstruction surgery, for instance, the craniofacial reconstruction [23, 29]. Among the congenital defects, craniofacial anomalies are a group of highly diverse and complex that affects a significant proportion of people in the world [10]. Besides the cases of congenital deformities, there is an occurrence of acquired craniofacial defects due to other diseases, as tumors. In the last four decades, an increasing volume of cases of facial trauma was also observed, which is closely related to the increase of traffic accidents and urban violence [11].

Additive manufacturing can also be used in dental implants because the models provide information about size, direction, and location of the implants, as well as anatomical information, such as the path of mandibular canals. In cases of bone abnormalities, it is important to notice that the gain in patient's functional and psychological terms and the increased quality of life after surgery justify the costs of the application of new technologies [24].

There are more than 20 types of additive manufacturing systems on the market which, in spite of using different technologies of addition material, are based on the same principle of manufacturing by layer. The main additive manufacturing technologies used are stereolithography (SLA), selective laser sintering (SLS), direct metal laser sintering (DMLS), selective laser melting (SLM), fused deposition modeling (FDM), 3D inkjet printing (3DP), and electron beam melting (EBM). These systems are classified according to the initial state of raw material, which can be liquid, solid, or powder form [35, 36].

The additive manufacturing technique used in this work is the direct metal laser sintering (DMLS). Among the advantages of this technique, there is the ability to process titanium and other metal powders directly on the machine, without the use of binders or the need for postcure. The manufacturing stage of a model and a mold for casting is not required, which reduces the cost and manufacture time of the implant. Furthermore, inadequate geometries to the casting process and hollow models can be produced. The sequence to obtain the prosthesis, from acquired data, to the custom-built design, until its construction using the DMLS technology, was carried out in a craniofacial reconstruction surgery (Figure 1).

The aim of this work is to study the mechanical and microstructural properties of samples produced by DMLS and compare them with the properties of a wrought and annealed commercial alloy.

2. Materials and Methods

The samples studied in this work were produced by the direct metal laser sintering (DMLS) technique using EOSINT M 270 machine (Figure 2(a)). In DMLS technique, the powder is spread and processed by the action of an Ytterbium fiber laser in an inert and thermally controlled environment inside a chamber. A system of scanning mirrors controls the laser beam describing the geometry of the layer on the surface

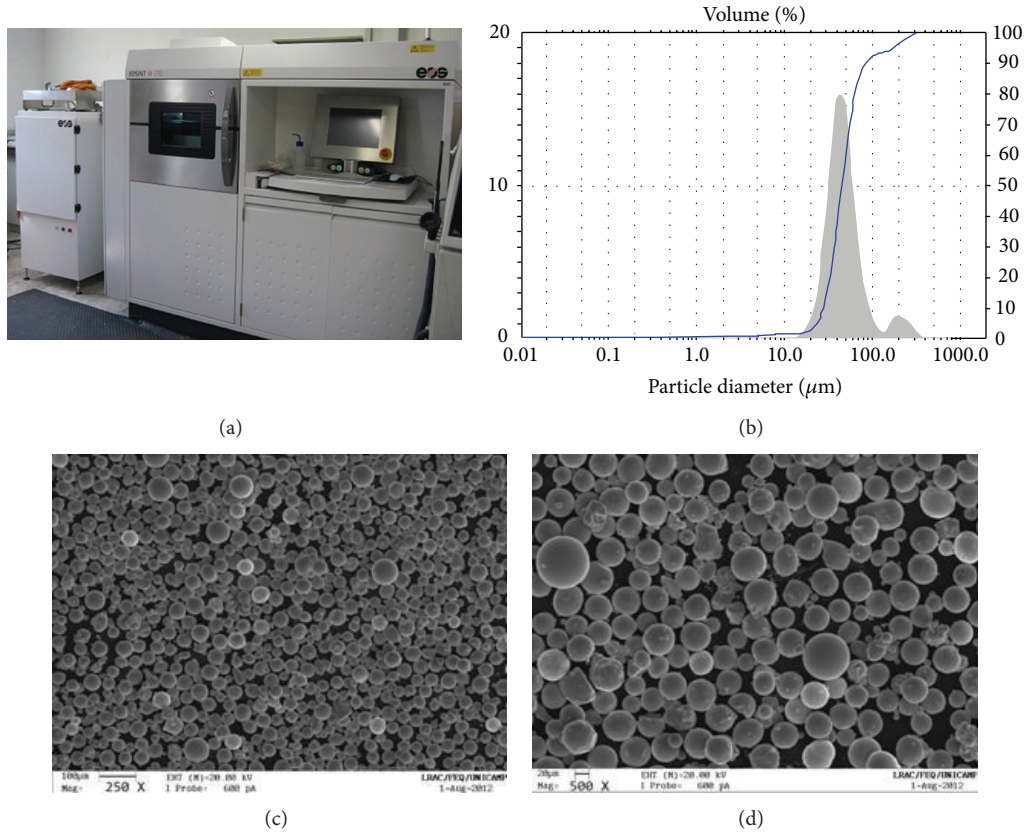

Figure 2: EOSINT M 270 machine (a), particle size distribution (b), and morphology of the commercial powder of the Ti6Al4V alloy used in the manufacturing of the samples ((c) and (d)).

of the spread material. With the incidence of the laser, the particles of material are heated and reach their melting point, joining each other and also to the previous layer. When the material solidifies, a new powder layer is added and the laser scans the desired areas once more; in other words, after the sintering of a layer, a new layer is deposited, and this process goes on until the construction of the part is finished. Thus, the solid model is built layer by layer [25, 27].

The material used for production of specimens was the commercial powder of the Ti6Al4V alloy. This powder has spherical morphology with a particle mean size of 57 μm and a size distribution with $D_{10} = 28\,\mu$m, $D_{50} = 45\,\mu$m, and $D_{90} = 85\,\mu$m (Figures 2(b), 2(c), and 2(d)). The processing parameters used to manufacture the specimens are shown in Table 1. During the processing, the argon gas was used to monitor the oxygen level within the chamber, acting also as protective gas.

For microstructural characterization and microhardness tests, three cylindrical samples measuring 12 mm diameter and 12 mm height were produced. The chemical composition of the samples was determined by the energy dispersive spectroscopy (EDS) technique using LEO-440i electron microscope with X-ray dispersive energy detector model 6070. The samples had their density measured according to the Archimedes principle and their porosity and microstructure analyzed by Olympus-BX60M optical microscope with Image Pro Plus 5.1 software and Zeiss-EVOMA15 scanning electron microscope with Smart SEM software, respectively.

Table 1: Processing parameters used in the DMLS process.

Parameters	Values
Laser power	170 W
Scan speed	1250 mm/s
Hatch spacing	100 μm
Layer thickness	30 μm

X-ray diffraction tests were performed with radiation source of Cu ($\lambda = 1.5406$ Å) and scanning angle 2 theta from 20° to 80°, using the Philips Analytical X Ray diffractometer, model X'Pert-MPD, and the X'Pert Data Collector software. Vickers microhardness tests were conducted according to the ASTM E384 standard [37] using Shimadzu digital microdurometer, model HMV-2T. The applied load was 500 gf for 10 seconds. 20 measurements were made and the shown results are the mean values.

Three specimens measuring 120 mm × 10 mm × 4 mm were manufactured by DMLS for tensile tests. These tests were conducted according to the ASTM E8/E8M standard [38] using the equipment MTS-810 and an extensometer MTS-632.24C-50. The mean values of ultimate tensile strength

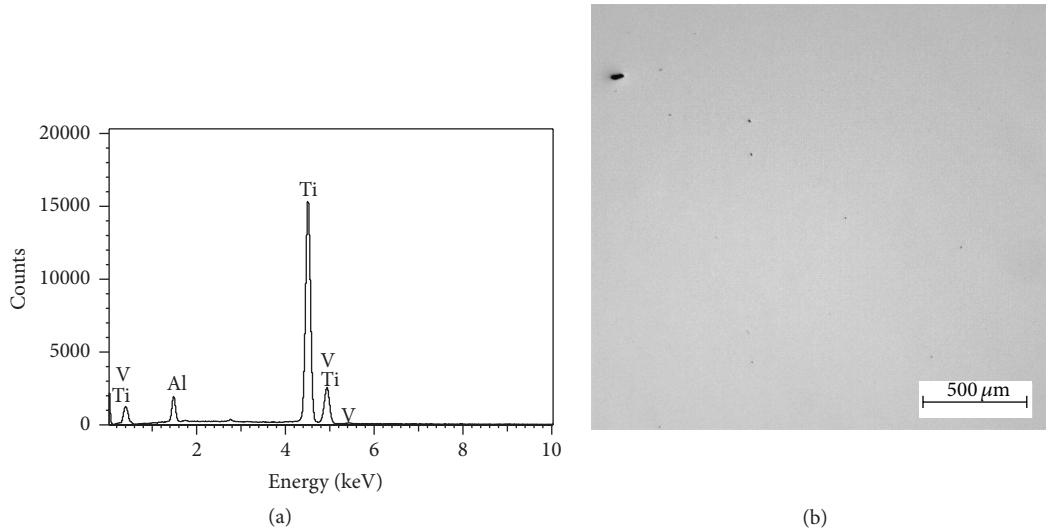

(a) (b)

Figure 3: Chemical elements (a) and pores (b) present in the samples produced by the DMLS process.

Table 2: Chemical composition of the samples produced by DMLS.

Elements	Chemical composition (%)	
	DMLS	ASTM F136
Al	5.79	5.50–6.50 ± 0.40
V	4.42	3.50–4.50 ± 0.15
Ti	89.79	Balance

Table 3: Tensile and microhardness tests results.

	Annealed	DMLS
Ultimate tensile strength (σ_u)	1045 MPa	1172 MPa
Yield strength (σ_e)	962 MPa	957 MPa
Young's modulus (E)	106 GPa	108 GPa
Elongation at rupture (Δl)	15%	11%
Vickers microhardness	314 HV	370 HV

(σ_u), yield strength (σ_e), Young's modulus (E), and elongation at rupture (Δl) of the material were determined. The microstructural and mechanical features of the samples produced by DMLS were compared to the samples features of the commercial Ti6Al4V alloy in the annealed condition.

3. Results and Discussion

The chemical composition of the samples produced by DMLS is according to the specification of the ASTM F136 standard [15], as shown in Table 2. The spectrum shown in Figure 3 confirms the presence of titanium, aluminum, and vanadium in the material. The processing parameters used in the process resulted in the production of samples at density 4.3785 g/cm^3, in other words, about 98%. This value shows that the samples produced by DMLS are very dense, even in the presence of some pores.

Figures 4(a) and 4(b) show that the microstructure of the annealed Ti6Al4V alloy consists of two phases, the α phase (dark phase) and the β phase (lighter phase), homogeneously distributed in the matrix α. The microstructure of the samples produced by DMLS is refined and constituted by hexagonal α' martensite with acicular morphology (Figures 4(c) and 4(d)). According to some authors [39, 40], the transformation of the bcc β phase to the α phase in the titanium alloys can occur martensitically or by nucleation and growth process, depending on the cooling rate and the alloy composition. During the fast cooling, the β phase can be transformed martensitically to the hexagonal α' phase. On slower cooling, the β phase can be transformed by nucleation and growth to the Widmanstätten α phase. In Figures 4(c) and 4(d), it is possible to observe the presence of orthogonally oriented martensite plates. The formation of martensite plates in the material means that the cooling rate during the laser sintering was high enough to induce the martensitic transformation. Since the DMLS process involves the melting of thin layers, with approximately 30 μm, the fast cooling favors this type of transformation [41].

The X-ray diffractograms shown in Figure 5 confirm the above described microstructural analysis. Concerning the annealed Ti6Al4V alloy, it is possible to observe the presence of not only the α phase but also the β phase in the $\langle 110 \rangle$ direction. For the DMLS sample, the only present phase is the α' phase. Since the α and α' martensite phases have the same crystalline structure, these phases show the same pattern in the diffractogram [42]. However, it is possible to observe in the sample produced by DMLS that the relative intensity of the peak of α' in the $\langle 110 \rangle$ direction is higher than the intensity of the other peaks, indicating a change in the preferential crystallographic orientation when compared to the annealed alloy.

Figure 6 and Table 3 show the results of the mechanical tests performed on both annealed and produced DMLS samples. There was no significant difference in the values of

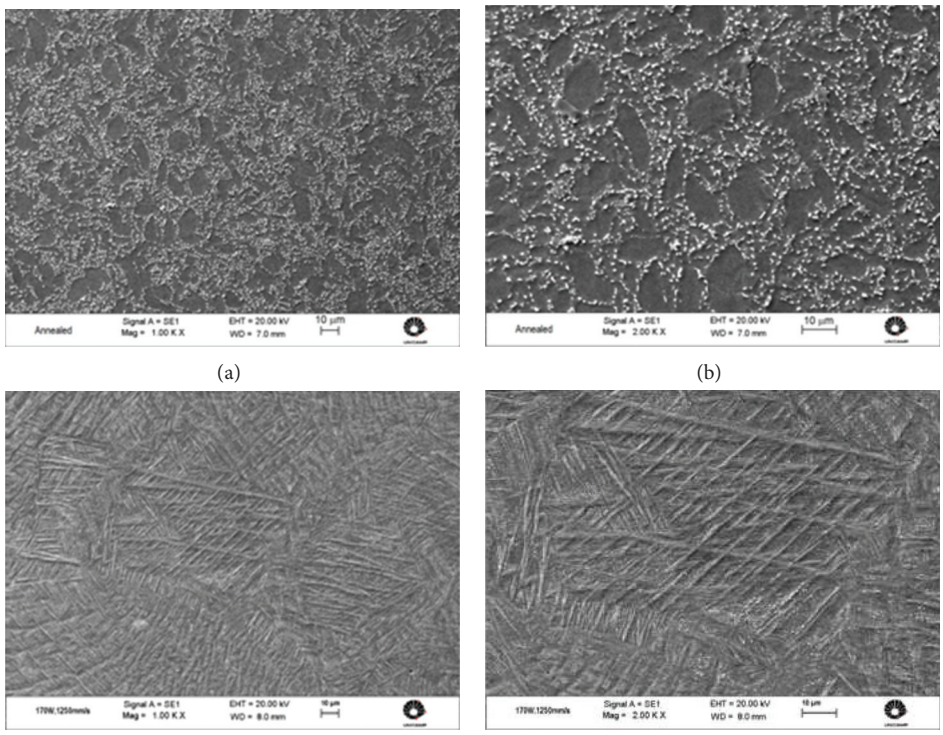

Figure 4: Microstructure of the Ti6Al4V samples in the annealed condition ((a) and (b)) and produced by DMLS ((c) and (d)).

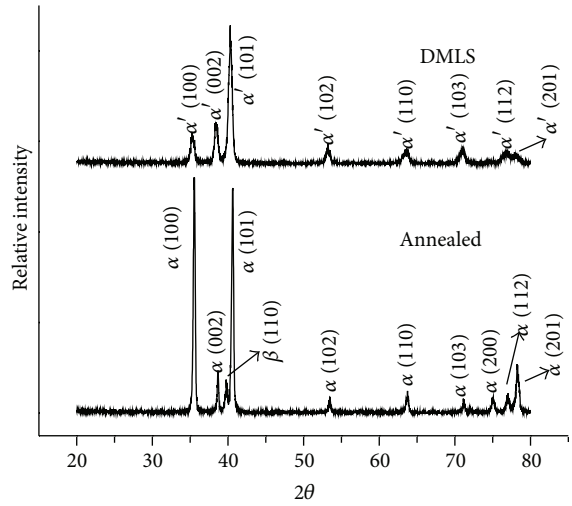

Figure 5: Diffractograms of the annealed and DMLS samples.

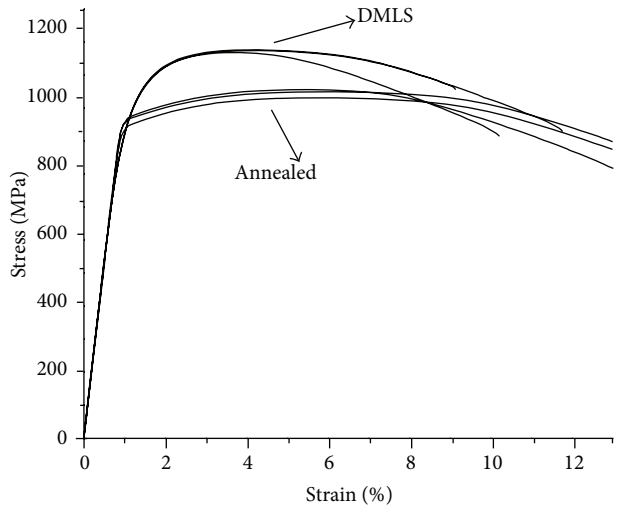

Figure 6: Stress-strain graphs of the annealed and DMLS samples.

σ_e and E; however, the samples produced by DMLS showed values of σ_u and microhardness higher than the samples in the annealed condition. On the other hand, the values of elongation at rupture show a lower ductility than the DMLS samples, which can be explained by a slight embrittlement due to the laser melting [43].

4. Conclusions

Additive manufacturing techniques have been applied in the production of custom-built implants that meet the physical characteristics of each patient. The processing parameters used in the DMLS process resulted in samples with refined microstructure, composed by hexagonal α' martensite, and acicular morphology, having a relative density of about 98%. The chemical composition of the samples is in accordance with the specification of the ASTM F136 standard. The X-ray diffraction confirmed that the only phase present in the DMLS samples is the α' phase. The ultimate tensile strength and microhardness values were superior to the ones obtained for the alloy in the annealed condition. There was a loss in ductility of the material, which can be explained by a slight embrittlement due to melting by laser.

Conflict of Interests

The authors declare that there is no conflict of interests regarding the publication of this paper.

Acknowledgments

The authors wish to acknowledge the financial support provided by the Scientific Research Foundation for the State of São Paulo (FAPESP-Process 2008/57860-3 and 2010/05321-1) and National Council for Scientific and Technological Development (CNPq-Process 573661/2008-1).

References

[1] M. M. Pereira, V. T. L. Buono, and C. A. C. Zavaglia, "Materiais metálicos—ciência e aplicação como biomateriais," in *Biomateriais: Fundamentos e Aplicações*, R. L. Oréfice and H. S. Mansur, Eds., pp. 39–58, Guanabara Koogan, Rio de Janeiro, Brazil, 2006.

[2] J. Parthasarathy, B. Starly, S. Raman, and A. Christensen, "Mechanical evaluation of porous titanium (Ti6Al4V) structures with electron beam melting (EBM)," *Journal of the Mechanical Behavior of Biomedical Materials*, vol. 3, no. 3, pp. 249–259, 2010.

[3] L. S. Bertol, W. K. Júnior, F. P. D. Silva, and C. Aumund-Kopp, "Medical design: direct metal laser sintering of Ti-6Al-4V," *Materials and Design*, vol. 31, no. 8, pp. 3982–3988, 2010.

[4] L. E. Murr, S. A. Quinones, S. M. Gaytan et al., "Microstructure and mechanical behavior of Ti-6Al-4V produced by rapid-layer manufacturing, for biomedical applications," *Journal of the Mechanical Behavior of Biomedical Materials*, vol. 2, no. 1, pp. 20–32, 2009.

[5] D. W. Petersen, J. E. Lemons, and L. C. Lucas, "Comparative evaluations of surface characteristics of cp titanium, Ti-6Al-4V and Ti-15Mo-2.8Nb-0.2Si (Timetal 21SRx)," *Journal of ASTM International*, vol. 2, pp. 151–165, 2005.

[6] E. J. Giordani, V. A. Guimarães, T. B. Pinto, and I. Ferrreira, "Propriedades de corrosão de dois aços inoxidáveis austeníticos utilizados como biomateriais," in *Proceedings of the Simpósio Matéria*, San Carlos de Bariloche, Argentina, 2003.

[7] G. Rondelli, B. Vicentini, and A. Cigada, "Localised corrosion tests on austenitic stainless steels for biomedical applications," *British Corrosion Journal*, vol. 32, no. 3, pp. 193–196, 1997.

[8] M. Terada, R. A. Antunes, A. F. Padilha, and I. Costa, "Corrosion resistance of three austenitic stainless steels for biomedical applications," *Materials and Corrosion*, vol. 58, no. 10, pp. 762–766, 2007.

[9] J. B. Park, Y. K. Kim, and J. D. Bronzino, *Biomaterials: Principles and Applications*, CRC Press, New York, NY, USA, 2003.

[10] M. Niinomi, "Recent metallic materials for biomedical applications," *Metallurgical and Materials Transactions A*, vol. 33, pp. 477–486, 2002.

[11] S. Abramson, H. Alexander, S. Best et al., "Classes of materials used in medicine," in *Biomaterials Science: An Introduction to Materials in Medicine*, B. D. Ratner, Ed., pp. 67–233, Elsevier, Academic Press, San Diego, Calif, USA, 2004.

[12] A. L. V. C. Silva and P. R. Mei, *Aços e ligas especiais*, Edgard Blücher, São Paulo, Brazil, 2006.

[13] S. A. Brown and J. E. Lemons, "Medical applications of titanium and its alloys: the material and biological issues," Special Technical Publication STP 1272, 1996.

[14] D. M. Brunette, P. Tengvall, M. Textor, and P. Thomsen, *Titanium in Medicine: Material Science, Surface Science, Engineering, Biological Responses and Medical Applications*, Springer, Berlin, Germany, 2001.

[15] American Society for Testing and Materials (ASTM) F136, Standard Specification for Wrought Titanium-6Aluminum-4Vanadium ELI (Extra Low Interstitial) Alloy for Surgical Implant Applications (UNS R56401), 2011 .

[16] J. Black, *Orthopaedic Biomaterials in Research and Practice*, Churchill Livingstone, New York, NY, USA, 1988.

[17] P. S. Walker, *Human Joints and Their Artificial Replacements*, Thomas, Springfield, Ill, USA, 1977.

[18] American Society for Testing And Materials ASTM F1798, "Standard Test Method for Evaluating the Static and Fatigue Properties of Interconnection Mechanisms and Subassemblies Used in Spinal Arthrodesis Implants".

[19] "American society for testing and materials ASTM F1800," Standard Practice for Cyclic Fatigue Testing of Metal Tibial Tray Components of Total Knee Joint Replacements.

[20] W. D. Callister, *Ciência e engenharia de materiais: uma introdução*, LTC, Rio de Janeiro, Brazil, 2002.

[21] J. Carvalho and N. Volpato, "Prototipagem rápida como processo de fabricação," in *Prototipagem Rápida: Tecnologias e Aplicações*, N. Volpato, Ed., pp. 1–15, Edgard Blücher, São Paulo, Brazil, 2007.

[22] I. Gibson, L. K. Cheung, S. P. Chow et al., "The use of rapid prototyping to assist medical applications," *Rapid Prototyping Journal*, vol. 12, no. 1, pp. 53–58, 2006.

[23] L. C. Hieu, E. Bohez, J. Vander Sloten et al., "Design for medical rapid prototyping of cranioplasty implants," *Rapid Prototyping Journal*, vol. 9, no. 3, pp. 175–186, 2003.

[24] J. A. Foggiato, "O uso da prototipagem rápida na área médico-odontológica," *Tecnologia Humanismo*, vol. 20, pp. 60–68, 2006.

[25] N. Volpato, "Os principais processos de prototipagem rápida," in *Prototipagem Rápida: Tecnologias e Aplicações*, N. Volpato, Ed., pp. 55–100, Edgard Blücher, São Paulo, Brazil, 2007.

[26] A. F. Antas, F. J. Lino, and R. Neto, "Utilização das tecnologias de prototipagem rápida na área médica," in *Proceedings of the* 5° *Congresso Luso-Moçambicano de Engenharia*, Maputo, Mozambique, 2008.

[27] M. Truscott, D. de Beer, G. Vicatos et al., "Using RP to promote collaborative design of customised medical implants," *Rapid Prototyping Journal*, vol. 13, no. 2, pp. 107–114, 2007.

[28] L. L. Hench, "Bioceramics: from concept to clinic," *Journal of the American Ceramic Society*, vol. 74, no. 7, pp. 1487–1510, 1991.

[29] S. Gopakumar, "RP in medicine: a case study in cranial reconstructive surgery," *Rapid Prototyping Journal*, vol. 10, no. 3, pp. 207–211, 2004.

[30] W. Wu, Y. Zhang, H. Li, and W. Wang, "Fabrication of repairing skull bone defects based on the rapid prototyping," *Journal of Bioactive and Compatible Polymers*, vol. 24, no. 1, pp. 125–136, 2009.

[31] R. S. de Oliveira, R. Brigato, J. F. Gurjão Madureira et al., "Reconstruction of a large complex skull defect in a child: a case report and literature review," *Child's Nervous System*, vol. 23, no. 10, pp. 1097–1102, 2007.

[32] M. Koike, P. Greer, K. Owen et al., "Evaluation of titanium alloys fabricated using rapid prototyping technologies—electrom beam melting and laser beam melting," *Materials*, vol. 4, pp. 1776–1792, 2011.

[33] C. V. Ferreira, J. R. L. Santos, and J. V. L. Silva, "Exemplos de aplicações da prototipagem rápida," in *Prototipagem Rápida: Tecnologias e Aplicações*, N. Volpato, Ed., pp. 196–224, Edgard Blücher, São Paulo, Brazil, 2007.

[34] S. Singare, Q. Lian, W. P. Wang et al., "Rapid prototyping assisted surgery planning and custom implant design," *Rapid Prototyping Journal*, vol. 15, no. 1, pp. 19–23, 2009.

[35] S. F. Khan and K. W. Dalgarno, *Design of Customized Medical Implants by Layered Manufacturing*, School of Mechanical and Systems Engineering, NC University, Tyne and Wear, UK, 2009.

[36] J. Milovanović and M. Trajanović, "Medical applications of rapid prototyping," *Mechanical Engineering*, vol. 5, pp. 79–85, 2007.

[37] "American society for testing and materials ASTM E384," Standard Test Method for Knoop and Vickers Hardness of Materials, 2010.

[38] "American Society for Testing and Materials ASTM E8/E8M," Standard Test Methods for Tension Testing of Metallic Materials, 2009.

[39] V. A. Joshi, *Titanium Alloys: An Atlas of Structures and Fracture Features*, CRC Press, New York, NY, USA, 2006.

[40] G. Lütjering and J. C. Williams, *Titanium*, Springer, Berlin, Germany, 2007.

[41] M. E. Ramosoeu, H. K. Chikwanda, A. S. Bolokang, G. Booysen, and T. N. Ngonda, "Additive manufacturing: characterization of Ti-6Al-4V alloy intended for biomedical application," in *Proceedings of the Light Metals Conference*, Johannesburg, South Africa, October 2010.

[42] L. Facchini, E. Magalini, P. Robotti, A. Molinari, S. Höges, and K. Wissenbach, "Ductility of a Ti-6Al-4V alloy produced by selective laser melting of prealloyed powders," *Rapid Prototyping Journal*, vol. 16, no. 6, pp. 450–459, 2010.

[43] B. Vandenbroucke and J. Kruth, "Selective laser melting of biocompatible metals for rapid manufacturing of medical parts," *Rapid Prototyping Journal*, vol. 13, no. 4, pp. 196–203, 2007.

Hindawi Publishing Corporation
Advances in Mechanical Engineering
Volume 2014, Article ID 640496, 7 pages
http://dx.doi.org/10.1155/2014/640496

Research Article

Manufacturing of Porous Polycaprolactone Prepared with Different Particle Sizes and Infrared Laser Sintering Conditions: Microstructure and Mechanical Properties

G. V. Salmoria,[1,2] D. Hotza,[1] P. Klauss,[1] L. A. Kanis,[3] and C. R. M. Roesler[2]

[1] *CIMJECT Laboratory, Department of Mechanical Engineering (EMC), Federal University of Santa Catarina (UFSC), 88040-900 Florianópolis, SC, Brazil*
[2] *Biomechanics Engineering Laboratory, University Hospital (HU), Federal University of Santa Catarina (UFSC), 88040-900 Florianópolis, SC, Brazil*
[3] *TECFARMA Group, University of Southern Santa Catarina (UNISUL), 88704-900 Tubarão, SC, Brazil*

Correspondence should be addressed to G. V. Salmoria; gean.salmoria@ufsc.br

Received 18 March 2014; Accepted 8 July 2014; Published 6 August 2014

Academic Editor: Cynthia Gomes

The techniques of Rapid Prototyping, also known as Additive Manufacturing, have prompted research into methods of manufacturing polymeric materials with controlled porosity. This paper presents the characterization of the structure and mechanical properties of porous polycaprolactone (PCL) fabricated by Selective Laser Sintering (SLS) using two different particle sizes and laser processing conditions. The results of this study indicated that it is possible to control the microstructure, that is, pore size and degree of porosity, of the polycaprolactone matrix using the SLS technique, by varying the particle size and laser energy density, obtaining materials suitable for different applications, scaffolds and drug delivery and fluid mechanical devices. The specimens manufactured with smaller particles and higher laser energy density showed a higher degree of sintering, flexural modulus, and fatigue resistance when compared with the other specimens.

1. Introduction

A porous material is a material containing voids, which is often considered a solid with defects and empty spaces (organized or nonorganized). The matrix is treated as the solid part of a porous material and the pores are typically filled with a fluid (liquid or gas). In the past, a material with pores was usually considered to be defective. However, nowadays, with improved knowledge, several technological applications have been identified for porous materials [1]. A porous medium is generally characterized by its morphology and porosity. Other properties, such as tensile strength and thermal/electrical conductivity, are derived from the structural characteristics and properties of the constituents [2].

The concept of porous media is used in many areas of applied science and engineering: physicochemical processes [3], filtration [4], liquid and gas absorption [5, 6], acoustics [7], geomechanics [8], hydrogeology [9], fluid thermomechanics [10], gas sensors [11], pharmaceutics [12], cosmetics [13], bioremediation [14], bone and cartilage tissue engineering [15], scaffolds [16], and other drug delivery devices [17]. Porous polymer devices are suitable for a wide range of applications but they can exhibit high variability according to the preparation technique. The main manufacturing procedures used are polymerization with an expanding agent, polymerization with cross-linking and an expanding agent, solvent-based techniques, solvent aggregation of particles, and particle sintering [18]. A typical porous polymer is prepared by particle aggregation and sintering resulting in the formation of a structure with open pores, pore size distributions from 10 to 500 μm, and porosity from 30 to 70% [19].

The techniques of Rapid Prototyping (RP), also known as Additive Manufacturing, have prompted research into methods used to manufacture polymeric materials with controlled porosity, particularly for tissue engineering applications [20]. The strategy in this area of research is to integrate Computer Aided Design (CAD) and RP techniques such as Selective

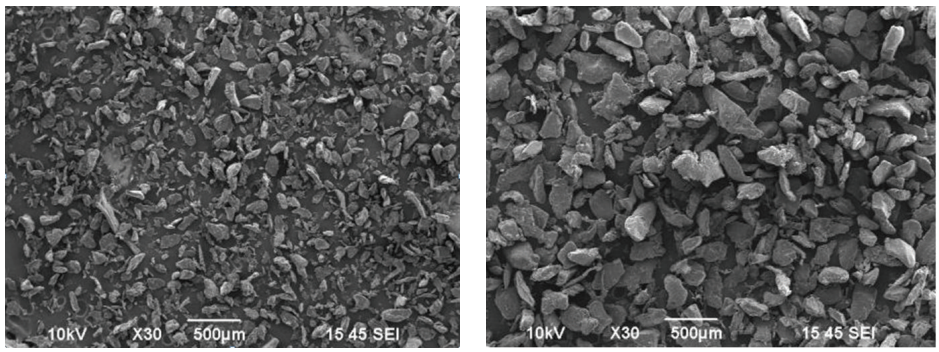

125–150 μm (a)

150–212 μm (b)

Figure 1: Micrographs of the PCL particles with size ranges of 125–150 μm and 150–212 μm.

Laser Sintering (SLS) to fabricate porous polymeric devices [21]. The control of the matrix porosity is achieved by manipulating the SLS process parameters of laser beam power and scan speed [22–25].

SLS has been successfully applied to different polymeric materials: polyamide [26], polyethylene (PE) [22], cellulose [27], PE/hydroxyapatite [24], and blends of PA/PA [28, 29] and PA/PE [30, 31]. Nevertheless, fabrication of polycaprolactone (PCL) based materials by SLS is still incipient [23]. In this context, this paper presents the characterization of the structure and mechanical properties of PCL manufactured by SLS using two different particle size ranges and laser power irradiation values.

2. Experimental

2.1. Material. The polymeric powder used in this study was commercial polycaprolactone (Sigma-Aldrich), with an average molecular weight of 70,000 to 90,000 g/mol, melt flow index of 1.0 g/10 min, and density of 1.145 g/cm^{-3} at 25°C. The PCL was ground cryogenically in a mechanical grinder and sieved. Particle size ranges of 125–150 and 150–212 μm were obtained.

2.2. Specimens Preparation by Selective Laser Sintering. The specimens (dimensions of 35 × 5.0 × 1.4 mm) were sintered in SLS equipment using a CO_2 laser (9 Watts) with a 250 μm diameter laser beam. For the manufacture of the specimens, the laser scanning speed was maintained at 50 mm/s, the hatch spacing was 100 μm, and the laser energy densities were 0.040 and 0.072 J/mm^2. The powder bed temperature was 45°C.

Table 1 shows the processing conditions (laser energy density) and particle size for the fabricated specimens.

2.3. Infrared Spectroscopy and Differential Scanning Calorimetry. The infrared spectrum of the polymer powder was obtained using a 16 PC Perkin Elmer spectrophotometer with Fourier Transform in order to evaluate the polymer absorbance at the CO_2 laser wavelength (10.6 μm). Differential Scanning Calorimetry (DSC) curves were obtained using a Shimadzu DSC50 calorimeter at temperatures ranging from −90 to 300°C, applying a heating rate of 10°C/min. The average sample weight was 6.7 mg and the nitrogen flow rate was 50 cm^3/min.

Table 1: The laser energy density and particle size range used in the fabrication of the specimens.

Specimen	Particles size (μm)	Laser energy density (J/mm^2)
A1	125–150	0.040
A2	150–212	0.040
A3	125–150	0.072
A4	150–212	0.072

2.4. Scanning Electron Microscopy. Philips XL30 and Jeol JSM-6390LV scanning electronic microscopes were used to investigate the particle characteristics, specimen microstructures, and cryogenic fracture topographies and features. The specimens were coated with gold in a Bal-Tec Sputter Coater SCD005.

2.5. Mechanical Analysis. Mechanical analysis was performed on a TA Instruments analyzer, model Q800. The samples were submitted to a flexural test (stress × strain) in the single cantilever mode using a controlled strength rate of 2 N/min at 30°C. For the determination of the storage modulus (E′) and the loss factor (tan δ), a fixed frequency of 1 Hz and temperature range of −90°C to 90°C, with a heating rate of 3°C/min and maximum strain of 0.5%, were used. Fatigue experiments were conducted at 30°C, with 5% of strain amplitude.

3. Results and Discussion

The micrographs in Figure 1 show images of the polycaprolactone (PCL) particles after grinding (125–150 and 150–212 μm).

Figure 2 shows the infrared spectrum for the PCL particles permitting the determination of the CO_2 laser beam absorption by the material at a wavelength of 10.6 μm. The PCL shows notable absorption at a wavelength of 10.6 μm, corresponding to the stretching of the –C–O– group (970 cm^{-1}).

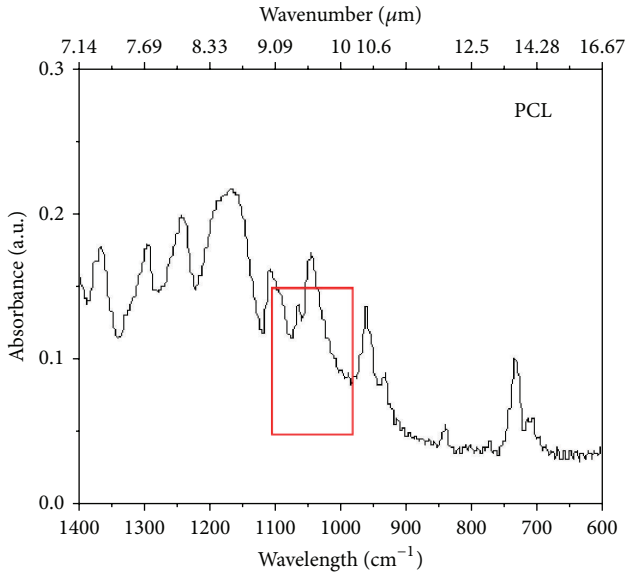

Figure 2: Infrared spectrum for the PCL powders.

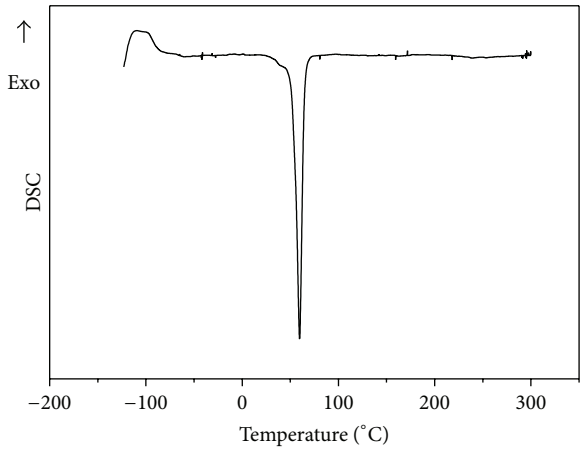

Figure 3: The DSC thermogram for the PCL powder.

Figure 3 shows the Differential Scanning Calorimetry (DSC) curves for the PCL powder, with a melting temperature of 59.60°C and 55% of crystallinity. The determination of the melting temperature (T_m) is of great importance for the polymer sintering process. The processing temperature of a semicrystalline polymer must be above its T_m, that is, in the case of PCL, above 60°C.

Figures 4 and 5 show the micrographs of the polycaprolactone specimens fabricated with different particle size ranges and laser energy densities, at magnifications of 30 and 100 times, respectively. The images show that the specimens present uniform porous morphology with coalesced particles and interconnected pores distributed in the sintered structure. The specimens fabricated with small particles (A1 and A3 specimens) presented a higher degree of sintering when compared with the specimens fabricated with larger particles at the same laser energy density (A2 and A4, resp.) (Figure 4).

Table 2: Average values for mechanical properties of the specimens obtained in stress-strain tests.

Specimens	Flexural modulus (MPa)	Strength at 10% of strain (MPa)
A1	74 ± 5.6	5.6 ± 0.3
A3	286 ± 1.1	21 ± 0.3
A2	2.8 ± 1.6	0.8 ± 0.1
A4	51 ± 7.0	4.8 ± 0.4

The specimen fabricated with smaller particles and higher laser energy density (specimen A3) presented a higher level of sintering, showing a co-continuous structure and dense morphology, which is probably due to the higher surface energy of the small particles and their tendency to coalescence at temperatures higher than the melting temperature T_m. On the other hand, the specimen fabricated with larger particles and lower laser energy density (specimen A2) presented a lower level of sintering showing the formation of small "necks" between the particles, resulting in a granular morphology (Figure 5).

Figure 6 shows the cryogenically fractured surfaces of the polycaprolactone specimens. The micrograph of specimen A3 shows that increasing the laser energy density causes greater coalescence of the particles, resulting in an increased thickness of the necks. Specimen A2 produced with larger particles and lower laser energy density showed a low level of sintering, where almost no fractures between the powder particles are observed.

Figure 7 shows the stress versus strain curves for the specimens produced under different processing conditions varying the particle size. Table 2 shows the values for the elastic modulus and strain (8.5% deformation) of the specimens.

The elastic modulus for the specimen manufactured with smaller particle size and higher energy density (A3) (286 MPa) differed considerably from that for the other specimens. This result suggests that the strength of the samples increases with a decrease in the particle size and increase in the laser energy density. Smaller particles have a larger surface area, allowing greater contact between the particles and the formation of a higher number of necks per unit area. For the A1 sample the same trend was observed (74 MPa) but the difference was less significant due to the lower value for the laser energy density. Specimen A2 presented the lowest value when compared with the other specimens, due to the low degree of sintering. As noted in the SEM images (Figure 6), the specimen fabricated with larger particles and lower laser energy density showed a low degree of sintering, with almost no fractures between the powder particles.

Figure 8 shows the behavior of the storage modulus (E′) for the polycaprolactone sintered specimens.

The specimens produced with a higher laser energy density (A3 and A4) tended to have higher E′ values. Specimen A3 showed a higher initial elastic modulus (609 MPa), then a decrease until around −60°C (544 MPa), followed by a sharp drop until 50°C. Specimen A4, manufactured with larger particles (lower degree of sintering), initially presented a lower elastic modulus (E′) than A3 (195 MPa), with a slight

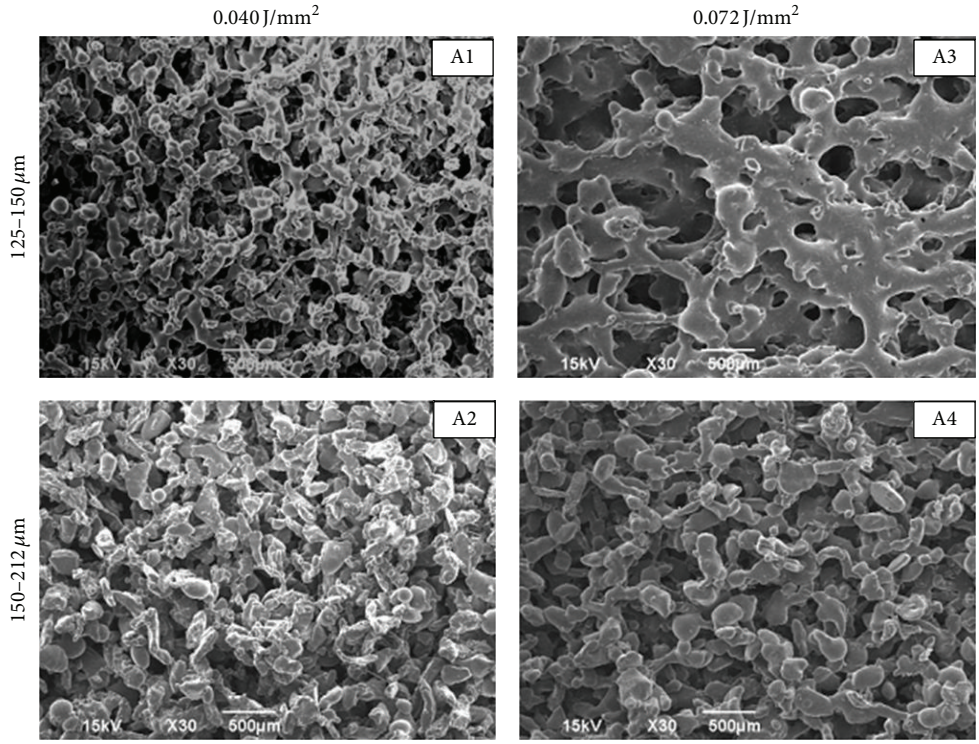

Figure 4: Micrographs of the surfaces of sintered polycaprolactone specimens (magnification 30 times).

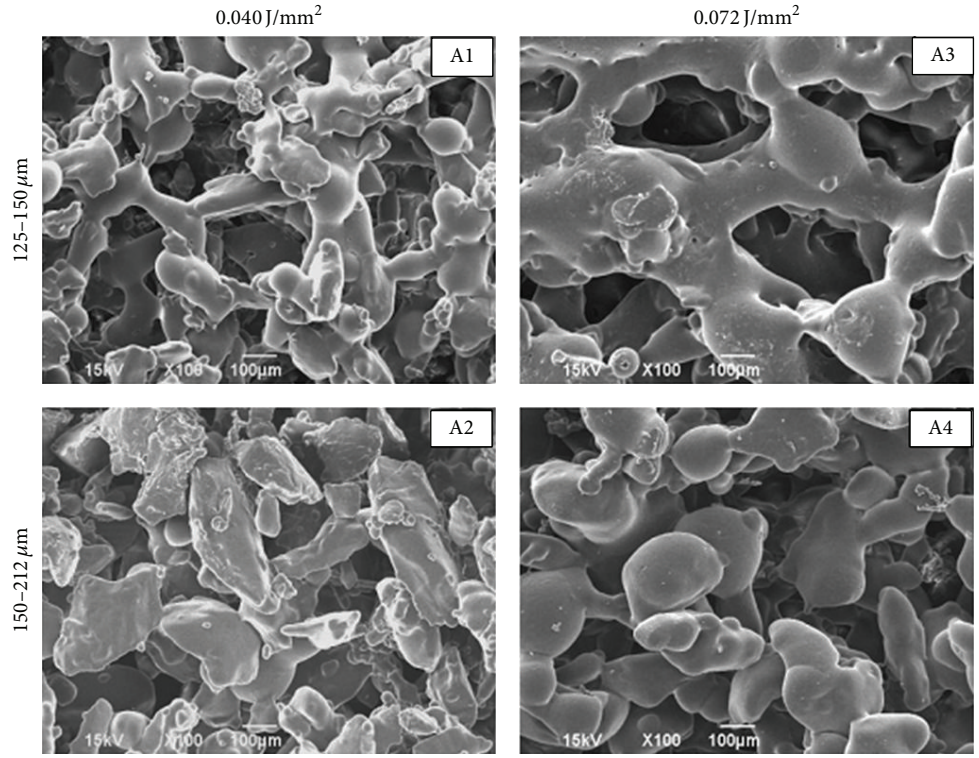

Figure 5: Micrographs of the surfaces of sintered polycaprolactone specimens (magnification 100 times).

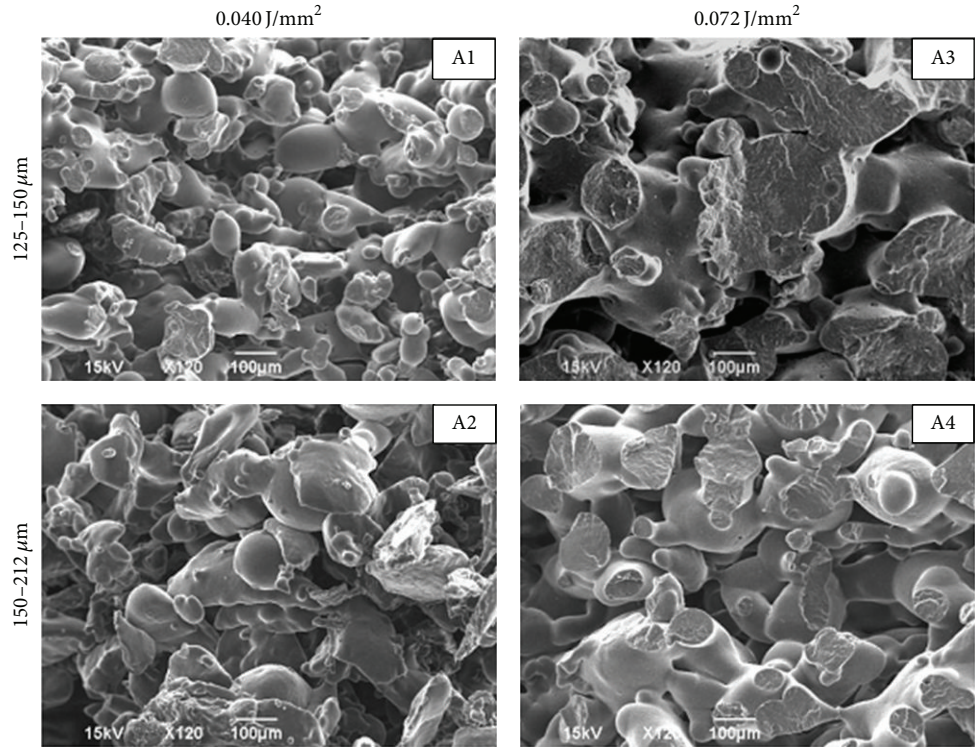

Figure 6: Micrographs of cryogenically fractured polycaprolactone specimens (magnification 120 times).

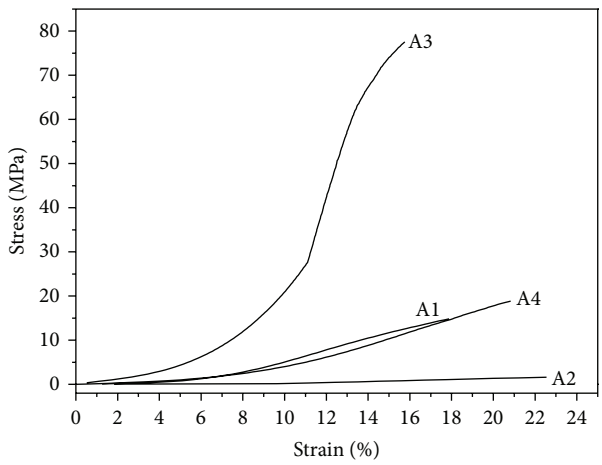

(A1) 125–150 μm/0.040 J/mm^2 (A2) 150–212 μm/0.040 J/mm^2
(A3) 125–150 μm/0.072 J/mm^2 (A4) 150–212 μm/0.072 J/mm^2

Figure 7: Stress versus strain curves for polycaprolactone specimens.

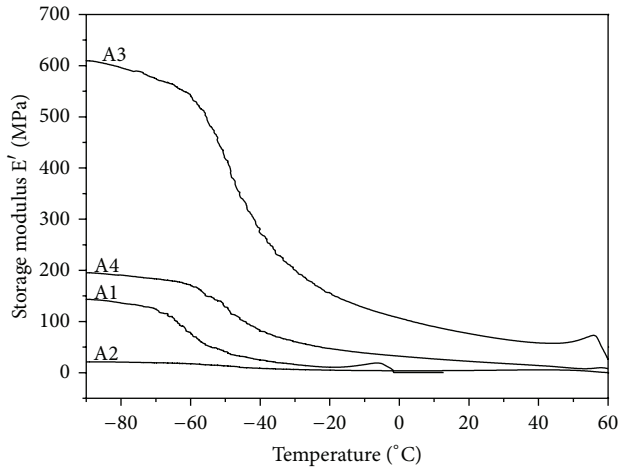

(A1) 125–150 μm/0.040 J/mm^2 (A2) 150–212 μm/0.040 J/mm^2
(A3) 125–150 μm/0.072 J/mm^2 (A4) 150–212 μm/0.072 J/mm^2

Figure 8: Storage modulus (E′) of polycaprolactone specimens.

decrease until around −60°C (168 MPa) followed by a more pronounced decrease. Specimen A1 had an initial elastic modulus of 143 MPa followed by a gentle decrease until around −70°C and then a faster decrease until 60°C. Specimen A2 had the lowest elastic modulus due to a lower degree of sintering. The initial elastic modulus value was 21.22 MPa and this remained practically constant until the melting temperature.

Analyzing the loss tangent curves (Figure 9) for the sintered parts, it was observed that the T_m values for samples A1, A3, and A4 (−4.06, −13.77, and −11.32°C, resp.) were very distant from those provided by the DSC for the powder (−59.60°C), which can be attributed to the processing conditions and cooling of the specimens.

Figure 10 shows the curves obtained in the fatigue tests (stress × cycle number) for specimens fabricated with polycaprolactone. A decrease in stress over time is a consequence

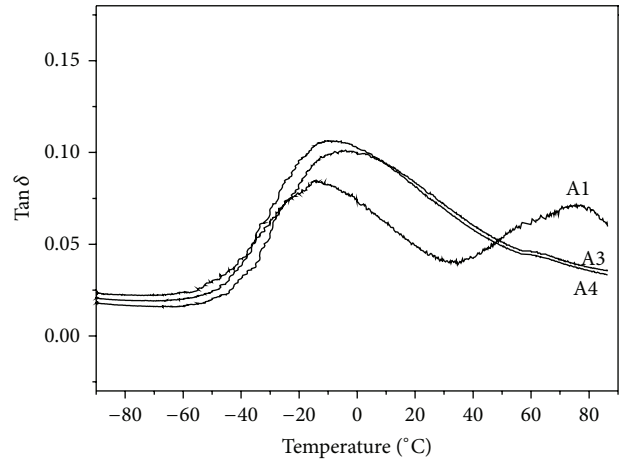

(A1) 125–150 μm/0.072 J/mm^2
(A3) 150–212 μm/0.040 J/mm^2
(A4) 150–212 μm/0.072 J/mm^2

Figure 9: Loss tangent (tan δ) for polycaprolactone specimens.

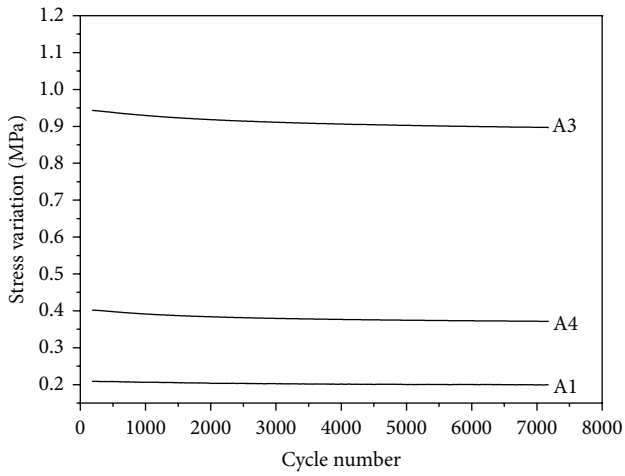

(A1) 125–150 μm/0.040 J/mm^2
(A3) 125–150 μm/0.072 J/mm^2
(A4) 150–212 μm/0.072 J/mm^2

Figure 10: Fatigue curves showing stress versus cycle number for the polycaprolactone specimens.

of molecular relaxation of the chains due to rotational movement.

In relation to the resistance of materials in service to forces and loads, the behavior under fatigue is extremely important. The specimens showed little variation in the stress applied as the cycle number increased, indicating that the fatigue resistance occurs only in the region of elastic deformation (reversible deformation). Due to the higher degree of sintering, A3 showed higher applied stress, indicating that initially the material is more rigid compared with specimen A4.

Specimen A1 had the lowest stress variation value, which was attributed to the low degree of sintering. The specimens were subjected to 7200 cycles with 20% deformation with no fractures occurring; however, for specimen A2, due to low degree of sintering and elastic modulus, the data were not recorded by the equipment.

4. Conclusions

In the manufacturing of parts, varying the particle size range and laser energy density employed, the microstructure obtained was found to be appropriate for application in biomedical fields, that is, uniform morphology, coalescence of particles and interconnected pores distributed in the sintered structure.

Specimen A3, manufactured with smaller particles and a higher laser energy density, had a larger surface area per unit volume, that is, greater contact with the laser beam, and increased packing of particles, providing a higher degree of sintering. This result was confirmed by the stress versus strain curves, storage modulus, and fatigue tests, which indicate higher values when compared with the other specimens. In the case of specimen A2, because of its low degree of sintering, as observed from the SEM images, there was practically no coalescence of the particles, the values being considerably lower when compared with other specimens, as expected.

The results of this study indicated that it is possible to control the microstructure, that is, pore size and degree of porosity, of polycaprolactone samples using the SLS technique, by varying the particle size range and laser energy density employed during processing. Samples appropriate for different purposes, such as scaffolds, drug delivery and fluid mechanical devices, can thus be produced.

Conflict of Interests

The authors declare that there is no conflict of interests regarding the publication of this paper.

Acknowledgments

The authors would like to thank the PRONEX program, FAPESC, and CNPq for the financial support.

References

[1] M. E. Davis, "Ordered porous materials for emerging applications," *Nature*, vol. 417, no. 6891, pp. 813–821, 2002.

[2] A. Thomas, "Functional materials: From hard to soft porous frameworks," *Angewandte Chemie—International Edition*, vol. 49, no. 45, pp. 8328–8344, 2010.

[3] M. Wang, Q. Kang, P. P. Mukherjee, and P. C. Lichtner, "Mesoscopic modeling of multiphysicochemical transport phenomena in porous media," *Advances in Mechanical Engineering*, vol. 2010, Article ID 142879, 11 pages, 2010.

[4] R. R. Trussell and M. Chang, "Review of flow through porous media as applied to head loss in water filters," *Journal of Environmental Engineering*, vol. 125, no. 11, pp. 998–1006, 1999.

[5] M. O. Adebajo, R. L. Frost, J. T. Kloprogge, O. Carmody, and S. Kokot, "Porous materials for oil spill cleanup: a review of synthesis and absorbing properties," *Journal of Porous Materials*, vol. 10, no. 3, pp. 159–170, 2003.

[6] R. E. Morris and P. S. Wheatley, "Gas storage in nanoporous materials," *Angewandte Chemie-International Edition*, vol. 47, no. 27, pp. 4966–4981, 2008.

[7] M. R. F. Kidner and C. H. Hansen, "A comparison and review of theories of the acoustics of porous materials," *International Journal of Acoustics and Vibrations*, vol. 13, no. 3, pp. 112–119, 2008.

[8] B. Ghanbarian, A. G. Hunt, R. P. Ewing, and M. Sahimi, "Tortuosity in porous media: a critical review," *Soil Science Society of America Journal*, vol. 77, no. 5, pp. 1461–1477, 2013.

[9] J. J. L. Higdon, "Multiphase flow in porous media," *Journal of Fluid Mechanics*, vol. 730, pp. 1–4, 2013.

[10] S. Wood and A. T. Harris, "Porous burners for lean-burn applications," *Progress in Energy and Combustion Science*, vol. 34, no. 5, pp. 667–684, 2008.

[11] M. P. Suh, Y. E. Cheon, and E. Y. Lee, "Syntheses and functions of porous metallosupramolecular networks," *Coordination Chemistry Reviews*, vol. 252, no. 8-9, pp. 1007–1026, 2008.

[12] K. Adibkia, M. Barzegar-Jalali, Y. Javadzadeh, R. Bayrami, and G. Mohammadi, "A review on the porous adsorbents in drug delivery systems," *Pharmaceutical Sciences*, vol. 18, no. 2, pp. 103–118, 2012.

[13] A. Ansaldi, "Porous entrapment spheres as delivery vehicles," in *Delivery System Handbook for Personal Care and Cosmetic Products*, pp. 323–332, William Andrew, 2005.

[14] T. K. Sen and K. C. Khilar, "Review on subsurface colloids and colloid-associated contaminant transport in saturated porous media," *Advances in Colloid and Interface Science*, vol. 119, no. 2-3, pp. 71–96, 2006.

[15] D. Hutmacher, "Scaffolds in tissue engineering bone and cartilage," *Biomaterials*, vol. 21, no. 24, pp. 2529–2543, 2000.

[16] K. Rezwan, Q. Z. Chen, J. J. Blaker, and A. R. Boccaccini, "Biodegradable and bioactive porous polymer/inorganic composite scaffolds for bone tissue engineering," *Biomaterials*, vol. 27, no. 18, pp. 3413–3431, 2006.

[17] G. Ahuja and K. Pathak, "Porous carriers for controlled/modulated drug delivery," *Indian Journal of Pharmaceutical Sciences*, vol. 71, no. 6, pp. 599–607, 2009.

[18] R. Balaji, S. Boileau, P. Guérin, and D. Grande, "Design of porous polymeric materials from miscellaneous macromolecular architectures: an overview," *Polymer News*, vol. 29, no. 7, pp. 205–212, 2004.

[19] D. Wu, F. Xu, B. Sun, R. Fu, H. He, and K. Matyjaszewski, "Design and preparation of porous polymers," *Chemical Reviews*, vol. 112, no. 7, pp. 3959–4015, 2012.

[20] S. H. Masood, J. P. Singh, and Y. Morsi, "The design and manufacturing of porous scaffolds for tissue engineering using rapid prototyping," *International Journal of Advanced Manufacturing Technology*, vol. 27, no. 3-4, pp. 415–420, 2005.

[21] K. Kincade, "Rapid prototyping evolves into custom manufacturing," *Laser Focus World*, vol. 41, no. 5, pp. 129–133, 2005.

[22] G. V. Salmoria, C. H. Ahrens, P. Klauss, R. A. Paggi, R. G. Oliveira, and A. Lago, "Rapid manufacturing of polyethylene parts with controlled pore size gradients using selective laser sintering," *Materials Research*, vol. 10, no. 2, pp. 211–214, 2007.

[23] G. V. Salmoria, P. Klauss, K. Zepon, L. A. Kanis, C. R. M. Roesler, and L. F. Vieira, "Development of functionally-graded reservoir of PCL/PG by selective laser sintering for drug delivery devices," *Virtual and Physical Prototyping*, vol. 7, no. 2, pp. 107–115, 2012.

[24] G. V. Salmoria, E. A. Fancello, C. R. M. Roesler, and F. Dabbas, "Functional graded scaffold of HDPE/HA prepared by selective laser sintering: microstructure and mechanical properties," *International Journal of Advanced Manufacturing Technology*, vol. 65, no. 9–12, pp. 1529–1534, 2013.

[25] G. V. Salmoria, P. Klauss, K. M. Zepon, and L. A. Kanis, "The effects of laser energy density and particle size in the selective laser sintering of polycaprolactone/progesterone specimens: morphology and drug release," *International Journal of Advanced Manufacturing Technology*, vol. 66, no. 5–8, pp. 1113–1118, 2013.

[26] V. E. Beal, R. A. Paggi, G. V. Salmoria, and A. Lago, "Statistical evaluation of laser energy density effect on mechanical properties of polyamide parts manufactured by selective laser sintering," *Journal of Applied Polymer Science*, vol. 113, no. 5, pp. 2910–2919, 2009.

[27] G. V. Salmoria, P. Klauss, R. A. Paggi, L. A. Kanis, and A. Lago, "Structure and mechanical properties of cellulose based scaffolds fabricated by selective laser sintering," *Polymer Testing*, vol. 28, no. 6, pp. 648–652, 2009.

[28] G. V. Salmoria, J. L. Leite, and R. A. Paggi, "The microstructural characterization of PA6/PA12 blend specimens fabricated by selective laser sintering," *Polymer Testing*, vol. 28, no. 7, pp. 746–751, 2009.

[29] G. V. Salmoria, J. L. Leite, L. F. Vieira, A. T. N. Pires, and C. R. M. Roesler, "Mechanical properties of PA6/PA12 blend specimens prepared by selective laser sintering," *Polymer Testing*, vol. 31, no. 3, pp. 411–416, 2012.

[30] G. V. Salmoria, J. L. Leite, C. H. Ahrens, A. Lago, and A. T. N. Pires, "Rapid manufacturing of PA/HDPE blend specimens by selective laser sintering: microstructural characterization," *Polymer Testing*, vol. 26, no. 3, pp. 361–368, 2007.

[31] J. Lisi Leite, G. V. Salmoria, R. A. Paggi, C. H. Ahrens, and A. S. Pouzada, "Microstructural characterization and mechanical properties of functionally graded PA12/HDPE parts by selective laser sintering," *International Journal of Advanced Manufacturing Technology*, vol. 59, no. 5–8, pp. 583–591, 2012.

Hindawi Publishing Corporation
Advances in Mechanical Engineering
Volume 2014, Article ID 185374, 10 pages
http://dx.doi.org/10.1155/2014/185374

Research Article

A Method to Characterize the Quality of a Polymer Laser Sintering Process

Stefan Rüsenberg, Stefan Josupeit, and Hans-Joachim Schmid

Direct Manufacturing Research Center (DMRC) and Particle Technology Group (PVT), University of Paderborn, Pohlweg 55, 33098 Paderborn, Germany

Correspondence should be addressed to Hans-Joachim Schmid; hans-joachim.schmid@upb.de

Received 28 February 2014; Revised 24 June 2014; Accepted 25 June 2014; Published 16 July 2014

Academic Editor: Jens Günster

The reproducibility and reliability of quality aspects are an important challenge of the polymer laser sintering process. However, existing quality concepts and standardization activities considering influencing factors along the whole process chain have not been validated experimentally yet. In this work, these factors are analyzed and kept constant to obtain a reliable material data set for different layer thicknesses and testing temperatures. In addition, material qualities regarding powder ageing effects are analyzed using different build heights and layer thicknesses: while an increase of the layer thickness reduces mechanical part strength and density, it also results in a less intense thermal ageing of unmolten powder due to shorter build times.

1. Introduction

Polymer laser sintering is a powder bed additive manufacturing technology that promises lots of advantages compared to conventional technologies like injection molding. High part complexity and individualism as well as a rapid manufacturing of parts are the main benefits. Nevertheless there are also a lot of challenges on the way from prototyping to manufacturing technology: costs, available materials, reproducibility, and standardization of quality aspects are only some of the issues to be approached. The development of a quality management for polymer laser sintering as well as the analysis of specific powder or process parameters has been in the focus of many research projects. However, a holistic view considering the whole production chain and the experimental validation of quality assurance concepts have not been performed yet.

Therefore, the main influencing parameters along the whole process chain from the CAD data to the finished product are figured out in this work. These parameters are kept constant to obtain a reliable set of different thermal, physical, and mechanical part properties, which are required for the qualification of the manufacturing technology in the industry. For all tests, the same batch of refreshed polyamide 12 material and the "EOS Part Property Profiles" for five different layer thicknesses were used. Tensile and impact properties are given as function of different testing temperatures and used layer thicknesses as well as investigations on powder ageing effects during the build jobs.

The findings are an adequate reproducibility of build jobs on the one hand and the powder and part properties on the other hand: the higher the layer thickness, the lower the mechanical part strength and density. In contrast, a higher layer thickness also results in a less intense thermal ageing of unmolten powder due to shorter build times. The testing temperature dependency of mechanical part properties is thereby comparable to traditionally manufactured specimen. The results of this work can be used to both qualify part properties and to validate a repeatable process quality of laser sintering systems in application.

At first, the chapter state of the art will give an overview about existing related works in literature. After that, the process chain is analyzed and an overview about the most important influencing factors is given. Then, the methods for the specimen fabrication and characterization are presented and discussed. First, results of the powder and part tests are shown in the results chapter.

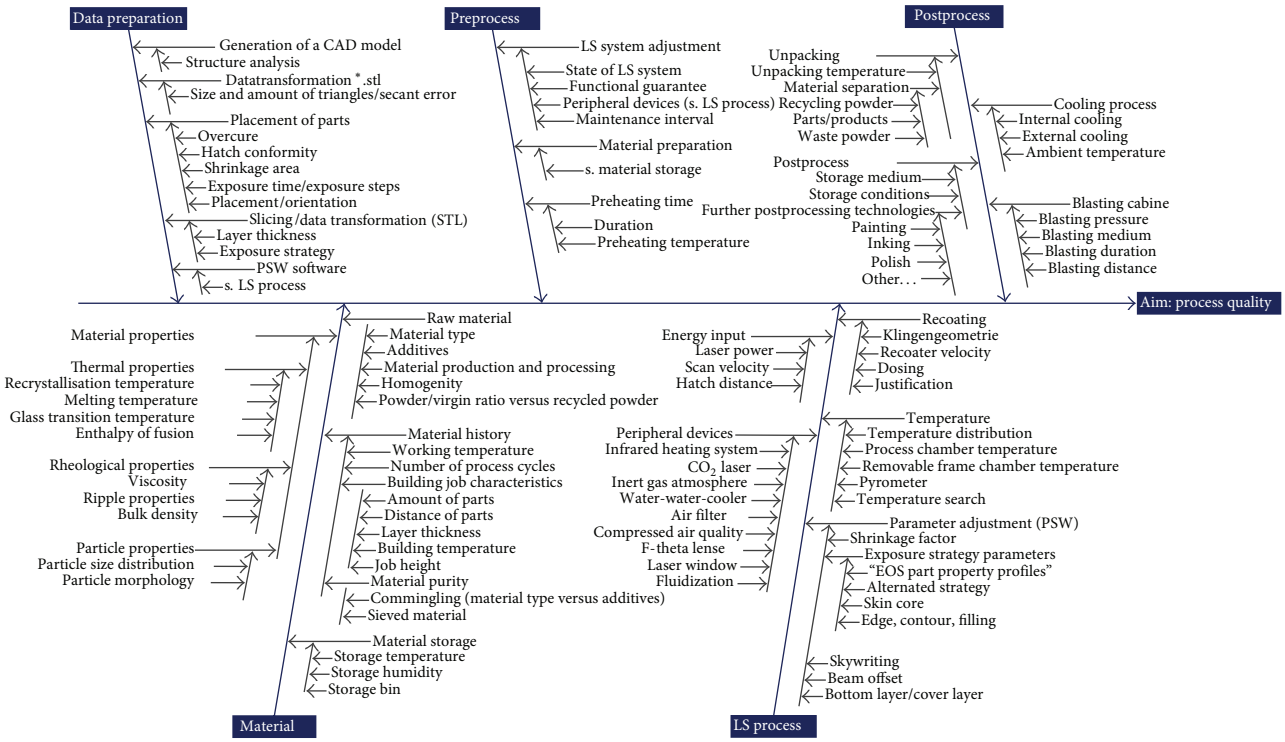

Figure 1: Influencing factors along the laser sintering process chain.

2. State of the Art

Polymer laser sintering is a very complex manufacturing process, which is influenced by many parameters along the process chain from the CAD model to the finished part. As a consequence, the quality of laser sintered parts is always a result of a multitude of parameters, which have to be kept constant for reproducible and robust part properties [1]. Depending on the individual application, "quality" criterions can be mechanical properties like tensile or impact behavior as well as good surface characteristics or the dimensional accuracy. To control all these parameters is still a challenge of additive technologies and is essential to use additive technologies for series production.

The influencing parameters can be categorized. For example, Schmid and Levy classified the influencing parameters into Equipment, Material, Production/Batch, and Part/Finish [2]. The material quality especially has been and is in the focus of many works: since mixtures of virgin and aged materials are used for part production, it is very important to investigate specific powder properties and correlate these with part and process characteristics. For example, the powder flowability investigated by Amado et al. [3] is important for a sufficient thin-layered powder application, while the characterization of thermal powder properties like the melting and recrystallization behavior investigated by Drummer et al. [4] is essential for choosing the right process temperatures. In addition, especially the measurement of the melt volume rate (MVR) and other rheological powder tests have been proven as methods to adjust the powder mixture ratio [5, 6] in order to influence the surface quality [7].

Regarding the production and the laser sintering process itself, the part orientation and placement within the building area as well as the process parameters, for example the laser energy density, building temperatures, scanning strategy, or the cooling procedure, are the most important influencing factors. While most of these parameters can be adjusted directly by the machine operator, other unwanted occurrences like an inhomogeneous temperature distribution on and within the powder bed lead to varying part qualities [8]. Therefore it is important to know and deal with the capability as well as the challenges of the available equipment.

As a result, the development of quality standards for the production of parts using the laser sintering technology became popular in the last years. For example, the VDI guideline 3405-1 [9] suggests specific powder characterization methods, an in-line process control, and testing of part properties to assure parts with constant properties. In addition, system requirements are stated to provide standardized reference values. Also the ASTM F42 committee is working on a specification for powder bed fusion of plastic materials.

3. Laser Sintering Process Chain

The laser sintering process chain illustrated in Figure 1 has been developed by Rüsenberg and Schmid at the Direct Manufacturing Research Center (DMRC) [1]. It considers five different steps from the CAD model to the finished product and shows relevant parameters influencing the process quality. A sixth step includes the specification of the process quality. The most important factors are described here.

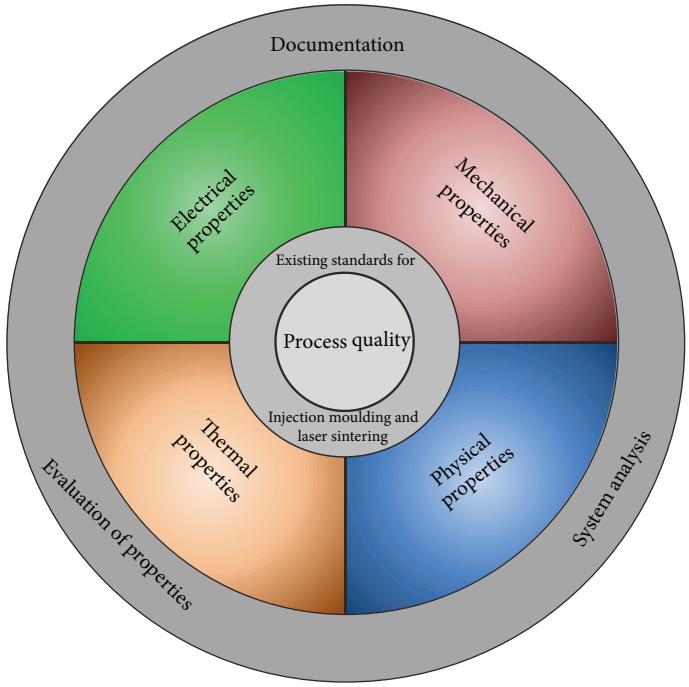

Figure 2: Key values to specify the laser sintering process quality.

3.1. Data Preparation. At first, a CAD model has to be generated and transferred into the STL format. Laser sintering specific design rules, for example, minimal clearances or wall thicknesses, have to be considered. The orientation of the parts as well as the positioning within the three-dimensional build area may also change part quality characteristics due to different temperature profiles, anisotropy effects, and number of hatch lines. In addition, a dimensional scaling has to be applied due to thermal shrinkage and overcure effects in the bottom layer(s) of a part.

3.2. Material. The material used has to fulfill a multitude of requirements for an optimal recoating and processing behavior: thermal and rheological properties have to be considered as well as particle properties like the size distribution and morphology. Another important aspect is the thermal ageing of the unmolten material during the build process: since recycled material is used, the history of the used powder has to be known. Instead of using a constant virgin/used powder ratio, the adjustment by rheological properties like the melt volume rate or the solution viscosity has been proven.

3.3. Preprocess/Machine Conditions. Several machine parameters like the laser power or the temperature distribution on the powder surface have to be controlled and adjusted regularly. Definite maintenance and cleaning intervals are essential for constant machine conditions. Before a build job starts, the machine has to be warmed up for sufficient heat homogeneity. The storage of the machine and the material in a constant standard atmosphere is also essential for reproducible results.

3.4. LS-Process. The laser sintering process itself can be divided into the following steps: recoating, preheating, and laser exposure, which are geared to each other precisely. Small changes in these parameters can have a significant influence. Here, the "EOS Part Property Profiles" are used, which are sets of defined process parameters to keep the process as constant as possible. For the different layer thicknesses, different recoater blade shapes are used. Thereby, especially the powder bed density can be influenced and again kept constant.

3.5. Postprocess. The most important step regarding the postprocess is the cooling of the part cake. For example, the cooling rates are dependent on the position within the part cake and the build height. The parts are unpacked only after the maximum core temperature is below the glass transition temperature of the material. If possible, the parts should be blasted automatically to eliminate any user dependency. In application, long-term ageing or strain effects must be considered.

3.6. Specification of the Process Quality. Figure 2 summarizes important key values to specify the laser sintering process quality. Existing standards and methods for the determination of part properties are mostly based on traditional manufacturing processes and have to be transferred to the laser sintering process characteristics, for example, the orientation dependency and layer thickness. Together with a documentation of the given parameters and an ongoing system analysis the evaluation of part and powder properties completes the laser sintering process chain.

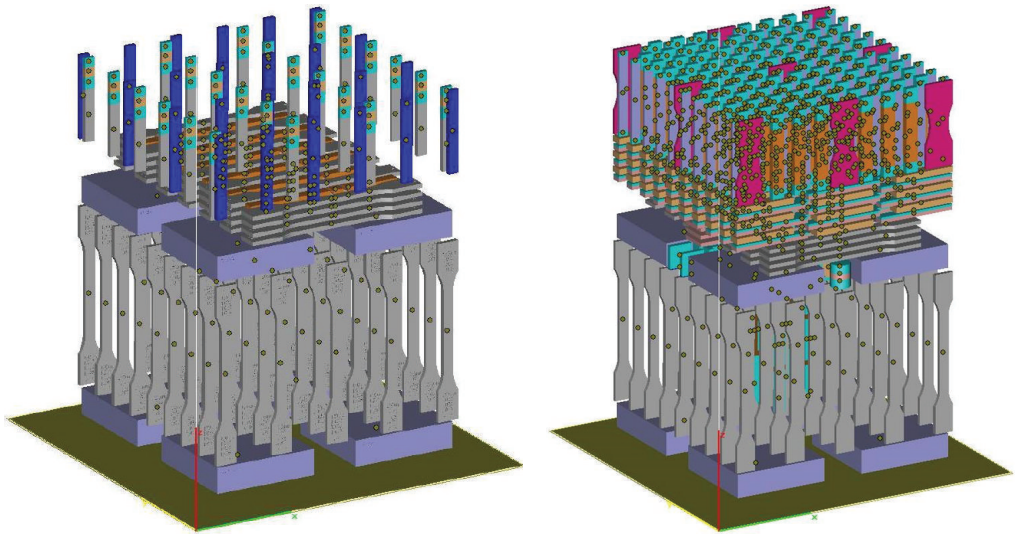

(a) (b)

Figure 3: Build job layout of the reference jobs RJ#1 (a) and RJ#2 (b).

4. Specimen Fabrication

For the determination of part properties and powder analysis, two reference jobs (RJ#1 and RJ#2; see Figure 3) are designed. The parts are arranged hatch-compliant with a minimal distance of 50 mm from the frame edges. In this build area, part properties were determined as adequate homogenous in previous experiments. To keep the laser exposure time per layer constant, "dummy" parts are included and built with the same exposure parameters as the other parts, but with zero laser power.

RJ#1 contains flat (x) and upright (z) oriented specimen for static tensile, compression, and flexural tests at different testing temperatures. Furthermore, eight hollow boxes are positioned in the bottom and center area of the build job to specify the powder bed density and position dependent powder ageing effects. The layout of RJ#2 is the same as that of RJ#1 in the lower part. The upper part contains specimens for the analysis of dynamic mechanical properties (torsion and bending), electrical conductivity, impact strength (Charpy and Izod), and the heat deflection temperature (HDT), again all in both x and z direction.

An EOSINT P395 laser sintering system from *EOS Electrical Optical Systems GmbH* is used to build the reference jobs. As exposure parameters, the "EOS Part Property Profiles" are used, which means that the exposure parameters like laser powder, scan velocity, and hatch distance are constant for the chosen layer thickness. The build chamber temperature is determined according to EOS instructions (build of crosses; non-curl-temperature +5 K) and given in Table 1. The removal chamber temperature is set at 130°C and the preheating time is 4 hours for each job. In total, RJ#1 is built twice and RJ#2 is built once for each layer thickness. All jobs were unpacked after a minimal cooling time of 10 hours within the machine in nitrogen atmosphere plus 24 hours in standard atmosphere until a maximal core temperature of 40°C. All specimens are blasted in an automatic blasting cabin with a rotating cage and defined blasting pressure of 3 bars and time of 10 minutes from a distance of approximately 25 cm. Due to water absorption, the specimens are conditioned in standard atmosphere (~21°C ± 1,5°C, relative humidity 50% ± 10%) for at least 4 weeks before testing.

Table 1: Different recoater blade shapes and build chamber temperatures according to the "EOS Part Property Profiles."

Layer thickness/(μm)	Build chamber temperature/(°C)	Recoater blade shape
60	177	flat
100	178	round
120	179	round
150	180	triangular
180	181	triangular

The material used for all jobs is one batch of refreshed polyamide 12 (PA 2200) powder delivered by EOS. The average melt volume rate of this powder is 31 cm^3/10 min ± 1 cm^3/10 min, which equates a powder ratio of ~46% virgin (~68 cm^3/10 min ± 1 cm^3/10 min) and ~54% used powder (~16 cm^3/10 min ± 1 cm^3/10 min). The used powder was cycled and refreshed 4 times before, which is close to a "circulatory" state and representative for a real application.

5. Part and Powder Characterization Methods

5.1. Powder Bed Density (PBD). The powder bed density is determined using the hollow boxes with the contained bulk powder, with outer dimensions of 100 × 100 × 25 mm^3 and a wall thickness of ~0.7 mm. At first, the absolute dimensions (X_{PB}, Y_{PB}, and Z_{PB}) are measured. Then, the mass of the whole box (m_1) is detected in an unopened condition as well

as in an opened condition with removed powder (m_L) using a *Mettler & Toledo XS4002S* balance. The wall thicknesses (d_x, d_y, and d_z) are the last values to measure. The powder box density is calculated with this formula:

$$\mathrm{PBD} = \left(X_{\mathrm{PB}} - 2 \cdot d_x\right) \cdot \left(Y_{\mathrm{PB}} - 2 \cdot d_y\right) \cdot \left(Z_{\mathrm{PB}} - d_{z,\mathrm{bottom}} - d_{z,\mathrm{top}}\right) \left(m_1 - m_L\right)^{-1}. \quad (1)$$

5.2. Melt Volume Rate. The determination method of the melt volume rate is described by Rüsenberg and Schmid at the PPS 2013 in Nuremberg [6] and at the European Forum on Rapid Prototyping 2012 in Paris [1]. The method is based on the test standard DIN EN ISO 1133 and EOS working instructions. A *Zwick Mflow* measurement device is used with a testing temperature of 235°C and a piston load of 5 kg. The material is predried in a furnace for 10 min at 105°C, 5 min at 105 → 140°C (ramp), and 2 min at 140°C. Each given value is the average of a minimum of three single measurements.

5.3. Part Density. For the part density determination, cubic test samples with an edge length of 21 mm are used. The density ρ_S is detected using the Archimedes principle described in standard DIN EN ISO 1183 and is calculated by the following formula [10]:

$$\rho_S = \frac{m_{S,A} \cdot \rho_{IL}}{m_{S,A} - m_{S,IL}}, \quad (2)$$

with $m_{S,A}$ being the sample mass in air, $m_{S,IL}$ being the sample mass within the sample fluid, and ρ_{IL} being the density of the sample fluid [11].

5.4. Tensile Properties. The tensile properties are detected according to DIN EN ISO 527 with an *INSTRON 5569* universal testing system with an *Advanced Video Extensometer* to detect the elongation. A truss speed of 1 mm/min to detect the Young's modulus and 50 mm/min for the strength and elongation at break is selected [12]. For the temperature dependent tensile tests, a heating/cooling chamber is attached to the testing system. All specimens are stored for a minimum of 20 hours within a climate chamber at testing temperature before the test starts.

Each RJ#1 contains 45 tensile specimens in z direction and 28 specimens in x direction. 9 specimens in z direction are tested dry (unconditioned) directly after unpacking to examine the reproducibility and comparability of build jobs. The rest of the specimen is divided into groups for the different testing temperatures: 4 × 9 specimen in z direction and 4 × 7 specimen in x direction. With two RJ#1 jobs, it is thereby possible to test eight different temperatures: −60, −30, 0, 22, 30, 40, 60, and 90°C.

5.5. Impact Properties. The impact properties are detected using the given standard DIN EN ISO 179 (Charpy) at an impact testing machine *Zwick/Roell, Model HIT5.5P*. For reliable results 10 test specimens in each direction are tested for one temperature. All test specimens are tested flatwise, without notch and with a pendulum of 5J.

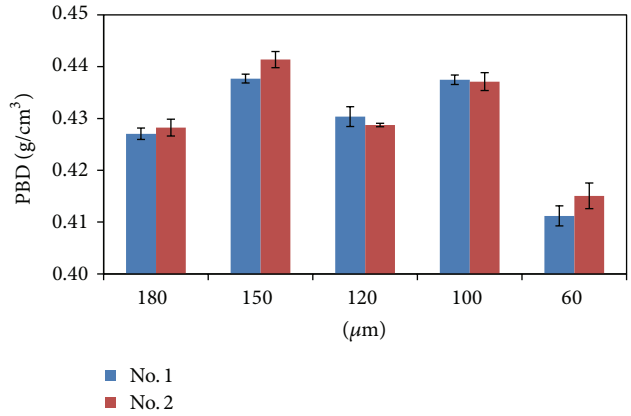

Figure 4: Powder bed density as function of layer thickness for RJ#1 and RJ#2.

6. Results and Discussion

6.1. Reproducibility of Build Jobs. A number of 9 upright built tensile test specimens (z direction), removed from each job at the same location, give information about the reproducibility from job to job. These specimens are tested at dry conditions. The results, for example, for a layer thickness of 100 μm, are nearly constant: the tensile strength is 47,63 MPa for the first and 46,62 MPa for the second reference job. The elongation at break and the Young's modulus also show no significant deviation (17,31% and 16,83%, resp.; 1650 MPa and 1674 MPa). These investigations are equivalent for each layer thickness; the reference jobs are reproducible and therefore a comparison is possible.

6.2. Powder Bed Density. The PBD shows different results for each layer thickness. There are no significant deviations between RJ#1 and RJ#2. The values shown in Figure 4 are the average of all 16 (RJ#1) or 8 (RJ#2) powder boxes per layer thickness. Jobs built with 60 μm thick layers have the smallest PBD (0.411 g/cm^3 ± 0.002 [RJ#1] and 0.415 g/cm^3 ± 0.002 [RJ#2]). The PBD for 180 μm as well as 120 μm is equivalent between 0.427 g/cm^3 ± 0.001 [RJ#1_180 μm] and 0.430 g/cm^3 ± 0.002 [RJ#1_120 μm]. There are no significant deviations being detected. The highest PBD are detected for a layer thickness of 100 μm and 150 μm: the values are between 0.437 g/cm^3 ± 0.0009 [RJ#2_100 μm] and 0.441 g/cm^3 ± 0.002 [RJ#2_150 μm]. The reason for the different powder bed densities is the different recoater blade shapes used for different layer thicknesses. For a layer thickness of 60 μm, a flat recoater geometry is used, while, for layer thicknesses of 100 μm and 120 μm, a round shape blade is used. The third geometry (triangular shape) is used for the layer thicknesses of 150 μm and 180 μm. Because of an equivalent particle size distribution (30 μm, ..., 100 μm) for all layer thicknesses, the particles have to be packed using different recoater geometries for a steadier PBD. It is noticeable that the smaller layer thickness, for example 100 μm in contrast to 120 μm, has higher powder bed density. For a small layer thickness like 60 μm, the particle recoating is difficult, because the layer

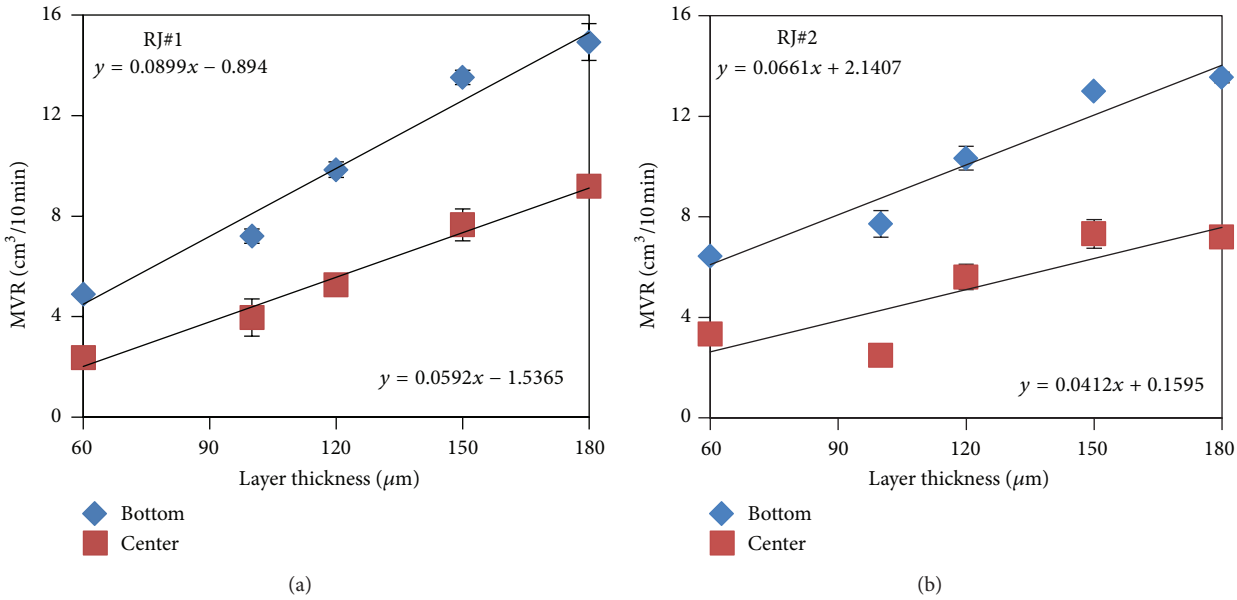

Figure 5: Melt volume rate (MVR) of the used powder from the bottom and center boxes.

thickness is smaller than the biggest particle size. Therefore it is necessary to use a flat blade to prevent a compaction of the powder bed. Consequentially, the PBD for 60 μm is much smaller than for the other layer thicknesses.

6.3. Melt Volume Rate (MVR). The powder ageing during the build jobs is shown for RJ#1 and RJ#2 (Figure 5) and is detected using the melt volume rate (MVR). A comparison of powder ageing effects for different layer thicknesses and at different positions within the part cake is possible due to equivalent build job layouts. It is obvious that the layer thickness directly influences the material ageing. For small layer thicknesses, the ageing is much higher than for high layer thicknesses. This effect can directly be related to the number of layers and thereby the build time. A longer dwell time of the powder at high temperatures results in a lower MVR due to a higher viscosity of the molten material.

Another finding is the position dependency of the powder ageing: for each layer thickness, the material ageing of the central placed powder boxes is much higher than of the bottom placed powder boxes. This effect can be traced back to the temperature history and distribution within the part cake: due to faster cooling rates at outer areas, the thermal ageing of the powder is less intensive and the dwell time at high temperatures is significantly shorter.

The differences between the first and the second reference jobs can also be traced back to the temperature-time profile. Although the absolute position of the powder boxes within the part cake is the same, the relative position is another because RJ#2 is 60 mm higher than RJ#1. The lower slope of the trend line considering the higher build job RJ#2 indicates that the layer thickness dependency is less intense. The absolute values between RJ#1 and RJ#2 vary only at very low and high layer thicknesses.

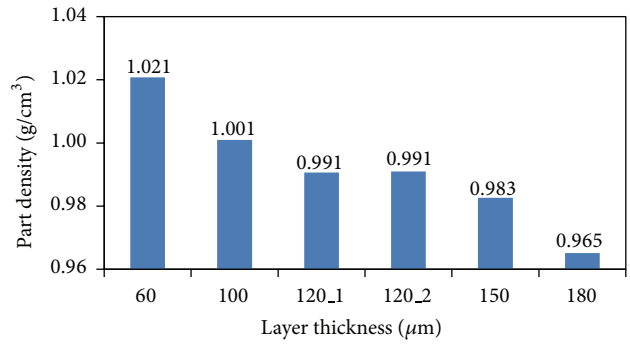

Figure 6: Part density as function of the used layer thickness.

6.4. Part Density. The part density shown in Figure 6 depends on the layer thickness. The part density decreases using higher layer thicknesses. It is noticeable that parts built with a layer thickness of 60 μm have the highest part density ($\rho_{60\,\mu m} = 1,0208\,g/cm^3$), although the powder bed density using this layer thickness is the smallest. The part density points to the different energy densities regarding different layer thicknesses. A layer thickness of 60 μm seems to have a higher energy density than other thicknesses. For a layer thickness of 120 μm also the reproducibility is shown: the part density for the first job ($\rho_{120\,\mu m\_1} = 0{,}9907\,g/cm^3$) does not deviate significantly from the second one ($\rho_{120\,\mu m\_1} = 0,9910\,g/cm^3$).

6.5. Tensile Properties. The tension tests are performed for all layer thicknesses as well as chosen temperatures (−60°C, . . ., 90°C) using specimens from the first reference job RJ#1. The left graph shows the Young's modulus as a function of

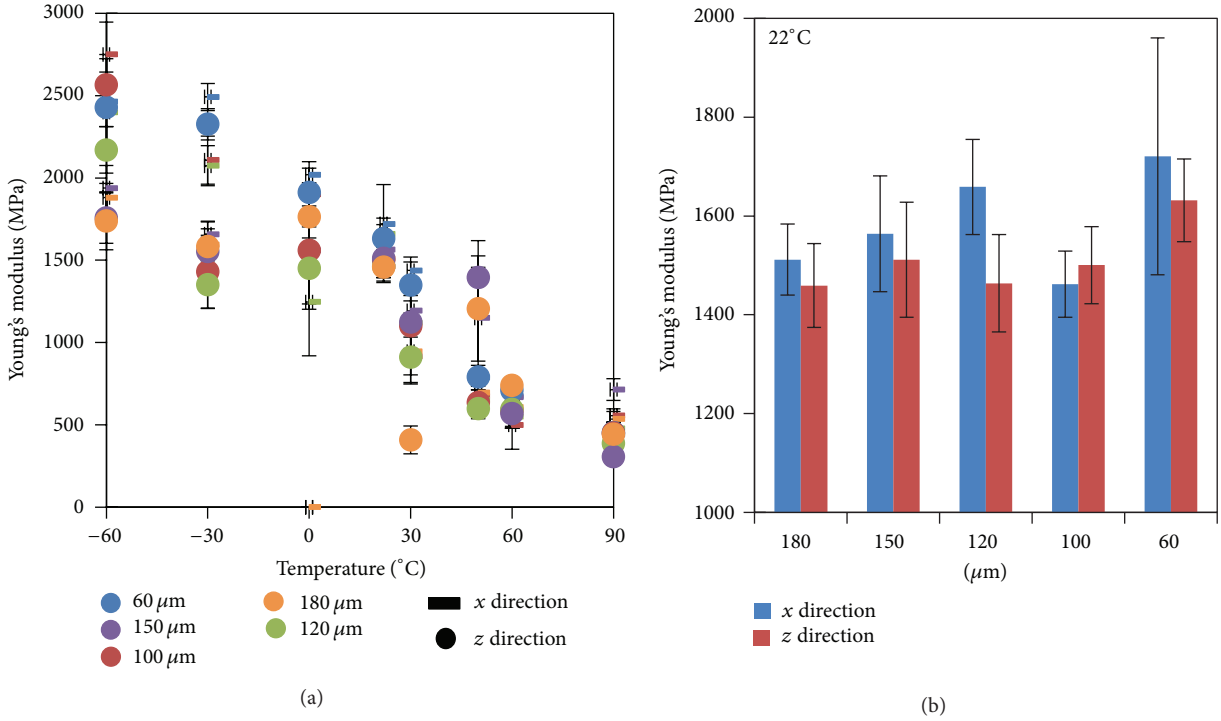

FIGURE 7: Young's modulus as function of the layer thickness and testing temperature for x and z direction.

different layer thicknesses as well as different build orientations. It is noticeable that the Young's modulus (Figure 7) in x direction is higher than in z direction. For the Young's modulus detection it is difficult to get a sensible statement about significant deviations. For lower temperatures the smaller layer thicknesses show higher Young's moduli than the higher layer thicknesses. For 60 μm and 100 μm the curve is sloping down until room temperature. The other curves are sloping down in a smoother way and seem to be constant between −60°C and 0°C. It is conspicuous that the moduli within the glass transition temperature area, which is between 30°C and 50°C, fall down below 500 MPa at 90°C. As can be seen in the right graph, a significant deviation of the Young's modulus for different layer thicknesses cannot be detected due to large error bars. The trend for x direction only shows small deviations: the values are increasing for smaller layer thicknesses.

The tensile strength (Figure 8) shows a behavior similar to the Young's modulus: it decreases with rising testing temperatures. For low temperatures it is visible that the strength of the test specimens placed in x direction is much higher than in z direction. These deviations become smaller for higher temperatures. A closer view is given by a look at the results for room temperature. The tensile strength shows increasing values with decreasing layer thicknesses as well as a higher tensile strength in x direction than in z direction. For a layer thickness of 180 μm the tensile strength in x direction is about 44.10 MPa ± 0.35 and therefore ~15% smaller than for 60 μm (51.94 MPa ± 1.11). The deviation for z direction (50.05 MPa ± 1.57 compared to 40.3 MPa ± 2.79) is about 20%. It is conspicuous that the first standard deviation for all layer thicknesses is higher in z direction than in x direction. Due to similar curve trends, the part density seems to have a direct influence on the tensile strength.

The elongation at break shown in Figure 9 indicates significant deviations between test specimens placed in x and z directions for all tested temperatures. The gradients show an opposing trend compared to the Young's modulus and the tensile strength with a higher elongation at break at high temperatures. Thereby, the variations between the different layer thicknesses are negligible for temperatures below 0°C. For higher temperatures, smaller layer thicknesses result in higher elongations at break. The graph on the right shows the elongation at break as function of the layer thickness in detail. The tensile bars in x direction show a much higher elongation at break than the samples in z direction. In z direction, the absolute values decrease for higher layer thicknesses. For specimens built in x direction, no significant layer thickness dependency can be observed due to an indistinct trend and high standard deviations.

6.6. Impact Strength. The curves given in Figure 10 show the impact strength as function of different testing temperatures and layer thicknesses. In general, the impact strength in x direction is higher than in z direction, especially at high temperatures. It is conspicuous that the test specimens have a nearly constant impact strength at temperatures below room temperature. The values increase by passing the glass transition area. A significant deviation between the different layer thicknesses is not shown with the exception of the values at a layer thickness of 60 μm, which is invalid because most

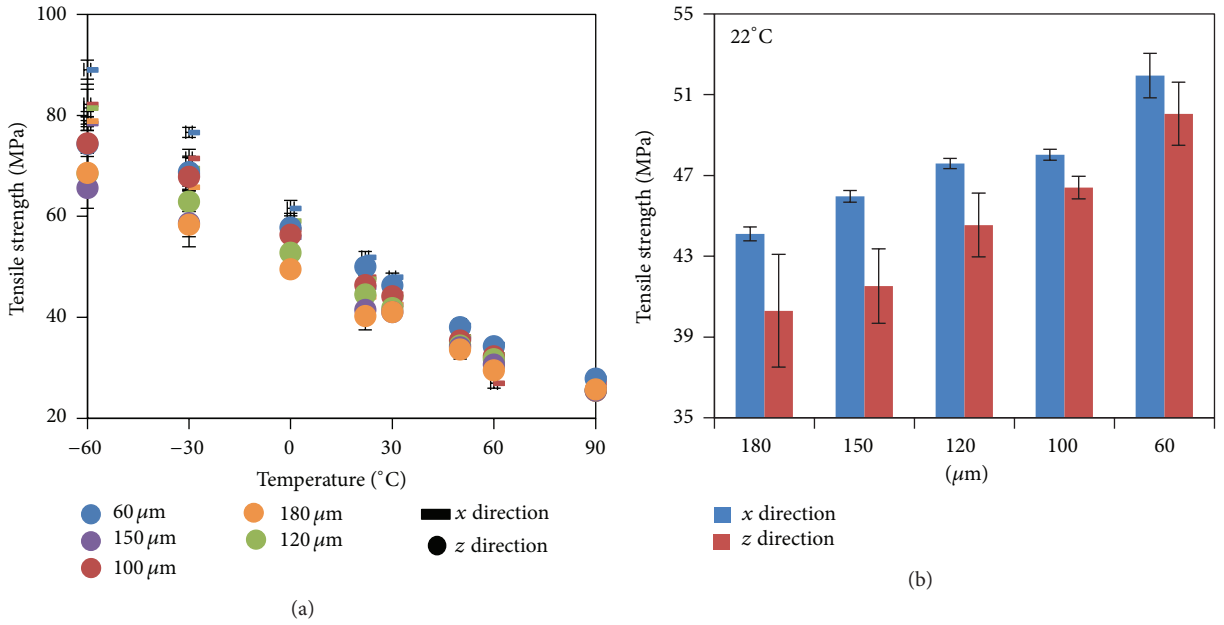

FIGURE 8: Tensile strength as function of the layer thickness and testing temperature for x and z direction.

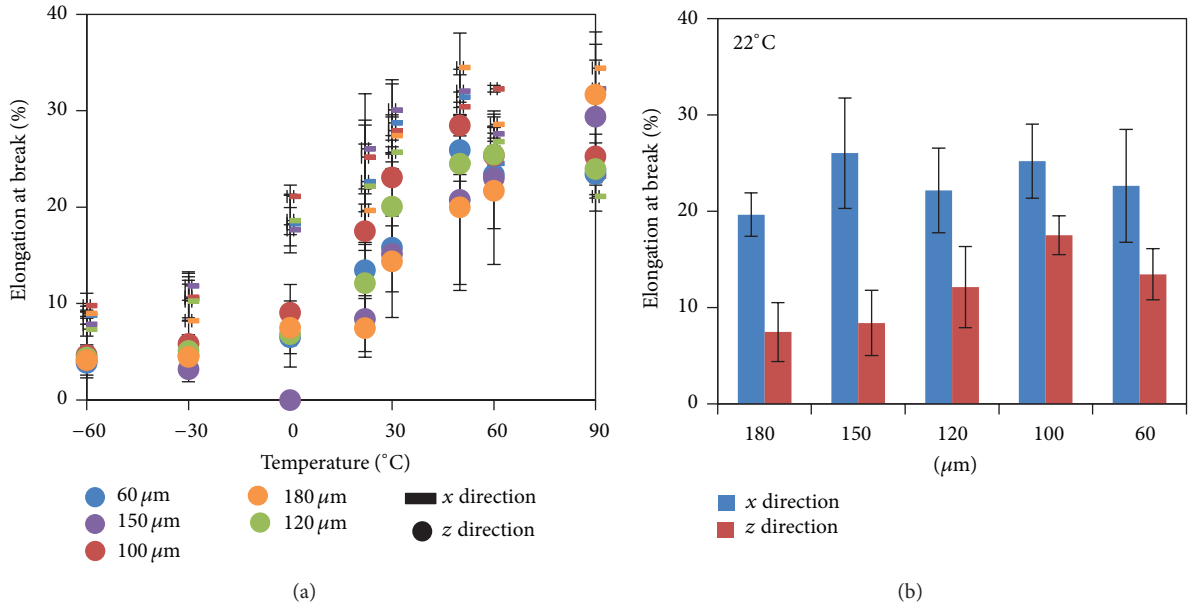

FIGURE 9: Elongation at break as function of the layer thickness and testing temperature for x and z direction.

of the values are outside of the detection parameters given in the test standard. The impact strength of 60 μm specimens in z direction has not been detected yet. The results for 50°C and 60°C for a layer thickness of 100 μm in x direction are also invalid. However, the impact strength for 60 μm specimen in x direction is significantly higher than for the other layer thicknesses and directions.

7. Conclusions

In this work the most important influencing factors along the process chain of the polymer laser sintering process have been identified and verified within a series of experiments keeping these parameters constant. Thereby, the field of parameters, where an acceptable product quality is secured, was determined. Also, the reproducibility and applicability of a quality concept in this holistic way have been shown and proven for the first time. The developed method can be used to get information about a complete data set as function of the main process parameters, for example, the layer thickness and the build orientation and placement. These data sets are essential to qualify the manufacturing process for specific applications. In total, two reference jobs were needed to detect the most important material properties. This work has been

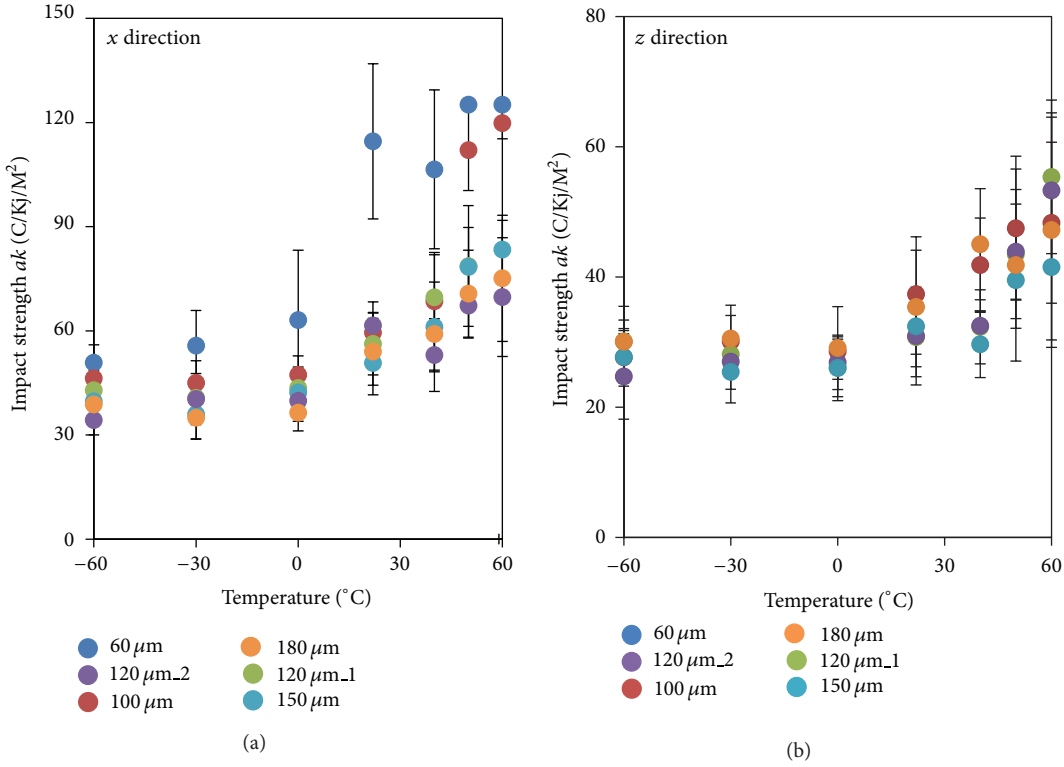

Figure 10: Impact strength as function of the testing temperature for x and z direction.

performed using a polyamide 12 standard material (PA 2200), but other materials like PA 2241 FR (flame retardant) or PA 2221 (refresh optimized) can be investigated with the same method.

Several mechanical and physical part properties have been investigated using the "EOS Part Property Profiles" standard parameters. While the smallest tested layer thickness results in the lowest powder bed density, the actual part density shows an opposing trend: the higher the layer thickness, the lower the part density. Similar results can be observed regarding the mechanical tensile properties: the tensile strength, Young's modulus, elongation at break, and the impact strength are higher using smaller layer thicknesses. Further on, the testing temperature dependency was analyzed from −60°C to +90°C. Here, laser sintered parts show a behavior comparable to traditional manufactured specimen with increasing tensile strength values and decreasing impact strength and elongation at break at low temperatures. However, the effect of build orientation has to be considered.

The material ageing depends on the layer thickness, the job height, and the position within the part cake. The temperature distribution and history during the build and cooling process are an important influencing parameter and have to be investigated in greater depth to find a solution for "more homogenous" part properties. The material ageing at the center of the part cake is higher than at the bottom. Also, the intensity of material ageing increases with smaller layer thicknesses. This effect can also be traced back to longer build times and thereby a "stronger" temperature-time-profile. In further experiments, it might be possible to get information about the temperature distribution and history investigating material samples from different positions.

Conflict of Interests

The authors declare that there is no conflict of interests regarding the publication of this article.

Acknowledgments

The authors want to thank the industry partners of the DMRC as well as the federal state of North Rhine-Westphalia and the University of Paderborn, Germany, for the financial and operational support. Many thanks are due to the assistance of EOS GmbH, Evonik Industries, and The Boeing Company for performing this project and working close together with industry staff to solve user questions.

References

[1] S. Rüsenberg and H.-J. Schmid, "Mechanical properties as a result of multitude of parameters," AEPR 12, 17th European Forum on Rapid Prototyping and Manufacturing, Paris, France, 2012.

[2] M. Schmid and G. Levy, "Quality management and estimation of quality costs for additive manufacturing with SLS," in *Proceedings of the Direct Digital Manufacturing Conference*, Berlin, Germany, 2012.

[3] A. Amado, M. Schmid, G. Levy, and K. Wegener, "Advances in SLS powder characterization," in *Proceedings of the 22nd Annual International Solid Freeform Fabrication Symposium (SFF '11)*, Austin, Tex, USA, 2011.

[4] D. Drummer, D. Rietzel, and F. Kühnlein, "Development of a characterization approach for the sintering behavior of new thermoplastics for selective laser sintering," *Physics Procedia*, vol. 2, part B, pp. 533–542, 2010.

[5] S. Rüsenberg, R. Weiffen, F. Knoop, and H.-J. Schmid, "Controlling the quality of laser sintered parts along the process chain," in *23rd Annual International Solid Freeform Fabrication Symposium (SFF '12)*, Austin, Tex, USA, 2012.

[6] S. Rüsenberg and H.-J. Schmid, "Advanced characterization method of nylon 12 materials for application in laser sinter processing," in *Proceedings of the 29th International Conference of the Polymer Processing Society*, Nuremberg, Germany, 2013.

[7] S. Josupeit, S. Rüsenberg, N. Rupp, and H.-J. Schmid, "Thermal ageing of polyamide 12 used for polymer laser sintering—influence on part quality characteristics," in *Proceedings of the ANTEC 2014*, Las Vegas, Nev, USA, April 2014.

[8] A. Wegner and G. Witt, "Ursachen für eine mangelnde Reproduzierbarkeit beim Laser-Sintern von Kunststoffbauteilen," in *RapidTech 2013*, Erfurt, Germany, 2013.

[9] *VDI Guideline: Additive Manufacturing Processes, Rapid Manufacturing—Laser Sintering of Polymer Parts—Quality Control*, VDI-Handbuch Produktionstechnik und Fertigungsverfahren, Band 2: Fertigungsverfahren, 2013.

[10] DIN EN ISO 1183, "Plastics—Methods for determining the density of non-cellular plastics—Part 1: immersion method, liquid pyknometer method and titration method," Germany, 2013.

[11] W. Hellerich, G. Harsch, and E. Baur, *Werkstoff-Führer Kunststoffe: Eigenschaften—Prüfungen—Kennwerte*, Carl Hanser, München, Germany, 2010.

[12] DIN EN ISO 527, Plastics—Determination of tensile properties, Germany, 2012.

Hindawi Publishing Corporation
Advances in Mechanical Engineering
Volume 2014, Article ID 217584, 7 pages
http://dx.doi.org/10.1155/2014/217584

Research Article

Investigations on Temperature Fields during Laser Beam Melting by Means of Process Monitoring and Multiscale Process Modelling

J. Schilp, C. Seidel, H. Krauss, and J. Weirather

Institute for Machine Tools and Industrial Management (iwb), Technical University of Munich, 85748 Garching, Germany

Correspondence should be addressed to C. Seidel; christian.seidel@iwb.tum.de

Received 28 February 2014; Accepted 12 May 2014; Published 9 July 2014

Academic Editor: Cynthia Gomes

Process monitoring and modelling can contribute to fostering the industrial relevance of additive manufacturing. Process related temperature gradients and thermal inhomogeneities cause residual stresses, and distortions and influence the microstructure. Variations in wall thickness can cause heat accumulations. These occur predominantly in filigree part areas and can be detected by utilizing off-axis thermographic monitoring during the manufacturing process. In addition, numerical simulation models on the scale of whole parts can enable an analysis of temperature fields upstream to the build process. In a microscale domain, modelling of several exposed single hatches allows temperature investigations at a high spatial and temporal resolution. Within this paper, FEM-based micro- and macroscale modelling approaches as well as an experimental setup for thermographic monitoring are introduced. By discussing and comparing experimental data with simulation results in terms of temperature distributions both the potential of numerical approaches and the complexity of determining suitable computation time efficient process models are demonstrated. This paper contributes to the vision of adjusting the transient temperature field during manufacturing in order to improve the resulting part's quality by simulation based process design upstream to the build process and the inline process monitoring.

1. Introduction

The laser beam melting (LBM) process is an additive manufacturing technology to produce almost fully dense metal parts from a powdery feedstock by utilizing a laser beam for the powder solidification. Today, a shift in the predominant application area of additive manufacturing processes from research laboratories to shop floors is evident [1]. Therefore, it is crucial to ensure a first-time-right process design and subsequently guarantee a reproducible and reliable quality standard. Process monitoring and modelling can foster this development by providing the possibility to deepen the process understanding and to improve the process design. This paper focuses on the simulation and experimental analysis of temperature fields, which are a key factor for process stability and part quality [2]. Therefore, temperature monitoring enables the detection of unpredicted process imperfections and proves the quality of each produced part. Microscale modelling provides insights on very short time scales and allows investigating corresponding process phenomena [3].

This paper wants to add scientific value by a combined view on the possibilities and limitations on both process monitoring and multiscale simulation. This can be useful to support process design for new materials or to calibrate thermal imaging data. Macroscale process models can support the process design by offering the possibility to analyze a part's temperature field upstream to the build job. Based on these temperature fields a thermomechanical analysis can be performed to forecast part deformations. These are mainly caused by residual stress release via the temperature gradient mechanism and are of major interest to technology users [4].

2. Materials and Methods

The solidification mechanisms in LBM are mainly influenced by the melt flow behavior and wettability and can be varied

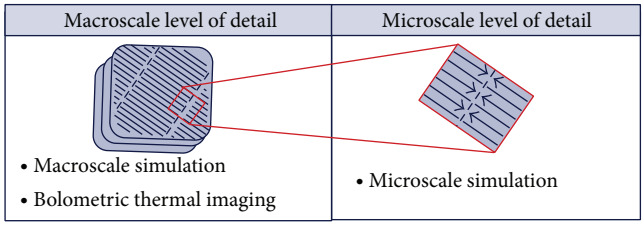

Figure 1: Investigated levels of detail.

through the applied scanning strategy. Depending on the latter, the material is reheated in several temperature cycles resulting in residual stress and deformation. Firstly, adjacent scan tracks cause a certain volume to reheat at hatch frequency (approximately 250 Hz). Secondly, the division of the total cross section into multiple scan areas (island-shaped, stripe-wise, etc.) results in additional thermal cycles for volume regions that are located close to the scan area boundaries; compare zoomed view in Figure 1.

Last, the weld penetration depth is considerably larger than the nominal layer thickness which causes a remelting and reheating of already solidified part regions. Within this paper, a comparison of simulation results with data gathered through process monitoring is performed on the macro- as well as the microscale level.

Thereby, the performance in terms of time and spatial resolution is discussed. For this purpose microscale modelling allows investigating the process with the highest possible temporal and spatial resolution. Due to the required calculation time, this simulation approach is limited to a few melt tracks only. This is caused by the fact that a large amount of solution steps is necessary to realize the intended micrometer and microsecond resolution. By utilizing abstraction methods, for example, the heat input, macroscale modelling allows investigating the whole part's thermal and subsequently structural behavior resulting from the build-up process. This leads to a decreasing number of solution steps compared to microscale modelling. The achievable resolution is in the order of magnitude of millimeters and milliseconds. Process monitoring is performed inline to the process using thermal imaging and can provide a complete part inspection at a timescale of milliseconds. The investigated material within this paper is the nickel-base alloy Inconel 718, which is commonly used in turbo machinery production. The experimental and numerical methods are introduced below.

2.1. Macroscale Simulation. The macroscale approach is used for the simulation of the additive manufacturing process of complete parts. For an acceptable computation time, several simplifications are necessary [4–8]. For a part-based simulation of the LBM process four fields of modelling can be identified [9, 10]: geometry, material, heat input, and ambient influences. Figure 2 illustrates how the geometry (first row) and the heat input modelling (second row) are carried out within this paper.

As data base, a sliced representation of the part's geometry (CLI-file) is used which comprises information (point

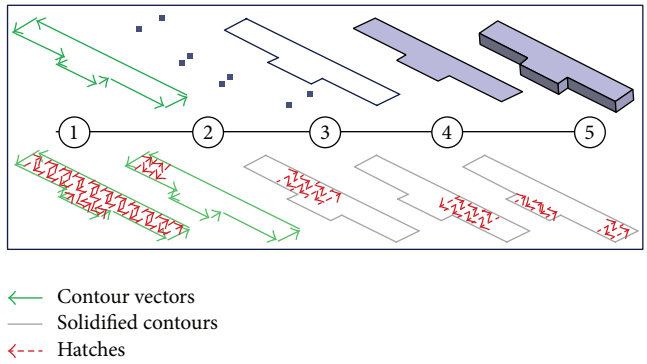

Figure 2: Multistep procedure of geometry and heat input modeling.

clouds) about laser scan vectors (both polylines for creating the part's contours and hatches to fill them) as well as all corresponding laser power values and scan velocities.

For the geometry modelling, the point cloud is imported to a FEA tool (ANSYS) as key points (2) after extracting the part contour (polylines) (1). Subsequently, lines are generated (3) to connect the key points. Closed vector contours are then converted to areas (4). Afterwards, the 2D-part description is extruded (5) according to the height of the present layer or layer compound (multiple layers grouped as one layer). By repeating the described procedure layer by layer or layer compound-wise the part's geometry is fully imported and a mesh which exhibits nodes on specific height levels is generated.

The heat input is modelled by prescribing a material specific temperature load to scan areas. Figure 2 (second row) illustrates the general principle of deriving scan areas from machine data. In Step 1, the whole scan vector information, hatches, and contour vectors (polylines), as transferred to the additive manufacturing machine, are shown. Steps 2 to 5 illustrate an abstraction of all scan vectors resulting in 4 load steps with a constant accumulated length of scan vectors proportional to the total length [10]. In the sense of this method, the most abstract option is to utilize only one single heat impulse to the total part cross section (solidus temperature constraint on the topmost layer). This was found to be a calculation time efficient modelling technique for the beam material interaction in order to analyze the resulting temperature field of a part to be built, but it is limited to properly model the different thermal cycles within one layer perpendicular to the build direction [8, 11].

The materials strength behavior is modelled by a multipoint linear kinematic hardening model [10].

2.2. Microscale Simulation. Several simulation approaches for laser material processing consider fluid-dynamic effects occurring in the heat affected zone [12–14]. In this sense, electron beam melting and laser beam melting are specifically investigated in [15–17]. Concerning this work, only conduction is considered as heat transportation mechanism within the microscale simulation model. Hence, transportation of heat energy caused by mass flow (e.g., fluid dynamics in

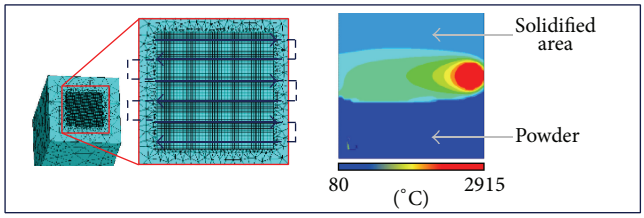

Figure 3: Approach for the microscale model.

the melt pool) is not taken into account in order to reduce calculation time.

The thermophysical properties of Inconel 718 are given in [18]. Temperature-dependent values for the absorptivity of Inconel 718 at the wavelength of Nd:YAG-laser (1.06 μm) can be found in [19]. For simplification and improvement of the convergence behavior a constant absorptivity value of 0.35 is assumed. In order to take the heat removal caused by evaporation into account, the temperature in the simulation approach is limited by the evaporation temperature of nickel (about 2915°C). The powder is modelled by a continuum approximation which means that there are no single powder particles but a solid with adapted properties [4]. Melting and solidification mechanisms of the powder bed elements are taken into account depending on their temperatures. When the temperature level reaches the solidus temperature the properties of these elements are changed to those of solid material.

For microscale modelling a heat source with a normally distributed intensity is applied. The beam properties for the investigated additive manufacturing system EOS M 270 can be found in [20]. The interaction between laser radiation and solid material is modelled by an area-related heat flux density obtained through multiplying the absorptivity by the intensity distribution [21]. Compared to solid material, the effective absorptivity of the powder domain is increased due to multiple reflections of the laser beam at the surface of the powder particles [22]. For considering the increased effective optical penetration depth a volume-related heat source is applied to the powder continuum. Here, the heat source is modelled in terms of heat flux density q_p (W/m^3), which exponentially decays with powder depth z:

$$q_p(r,z) = \frac{a_p}{d} \exp\left[-\frac{z}{d}\right] \frac{2P}{\pi w^2} \exp\left[-2\frac{r^2}{w^2}\right]. \quad (1)$$

The optical penetration depth d of the powder material is 20 μm according to [22]; the powder absorptivity a_p is assumed to be 0.6. Furthermore, P is the laser power and w denotes the 86% beam radius. The investigated process zone (500 μm × 500 μm × 60 μm) is meshed with uniform cubic elements with an edge length of 8 μm. The thickness of the powder layer is 40 μm. For modelling the underlying and already solidified regions a large block meshed with coarse tetrahedral elements is used; compare Figure 3.

2.3. Monitoring and Quality Methods. Approaches for measuring of quality-related variables (e.g., temperature, melt pool size, etc.) can be divided into coaxial setups, which are sensing the process emissions directly at the current beam position [23, 24], and off-axis setups, which usually monitor the complete build substrate at a time. In [25] the feasibility of layer-wise off-axis process monitoring based on a microbolometer IR-camera is shown and the setup used is presented. Deviations in the laser melting process, occurring at a timescale of several tens of milliseconds, can be detected by evaluating properties of the heat affected zone under idealized conditions. The typical response time for microbolometer cameras in the order of 8 ms limits the maximum frame rate to approximately 50 Hz. Furthermore, the pixel resolution of 250 μm causes spatial averaging over multiple single scan tracks (width: approximately 100 μm). Therefore, the peak temperatures cannot be determined reliably. This monitoring approach focuses on the spatially resolved analysis of the cool down behavior of a complete part section. An IR-detector (spectral range of 8 μm to 14 μm) is used to measure the associated temperature interval (melt temperature to room temperature). To derive the absolute temperature from IR measurements an effective emissivity of 0.2 is assumed, which is based on experiments that account for LBM-characteristic surface structure and the considered temperature range.

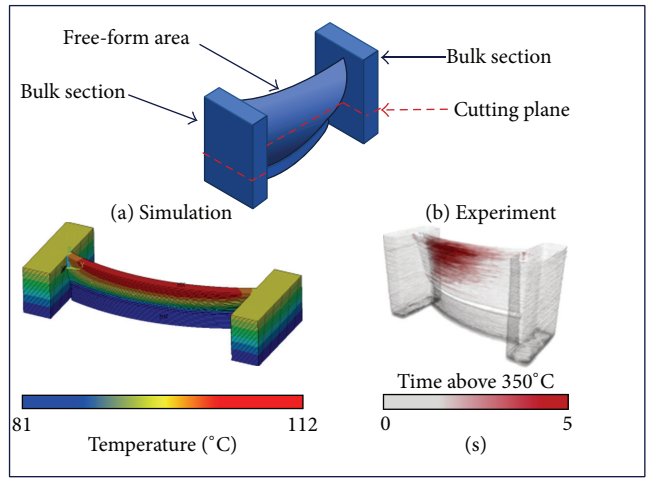

Figure 4: Turbine blade for macroscale investigations: simulation (a) and experimental (b) results for a cutting plane located at one-third of the part's height.

3. Results and Discussion

3.1. Macroscale Level. Based on the experimental and numerical setups described above, the temperature distributions are investigated for a blade geometry in aero engine applications. Furthermore, the thermal measurements are used to evaluate the accuracy of modelling approaches for the exposure strategy. Figure 4 shows the test specimen utilized for the macroscale investigations.

In the bottom right part of Figure 4 an experimental result illustrating the time over a specified temperature limit (350°C) is shown. On the left, the simulation result of

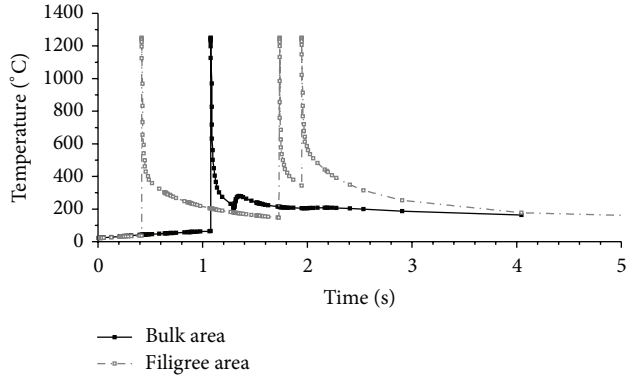

Figure 5: Simulated temperature curves for monitoring points within the bulk and free-formed section of layer compound 20 (numerical result).

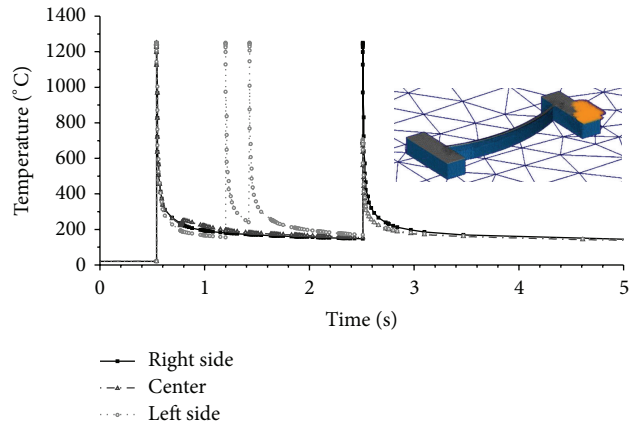

Figure 6: Temperature curve layer compound 20 (time scale adjusted) for 3 monitoring points within a load area in the top right corner (numerical result).

a modelled cool down step is illustrated (based on one single heat impulse to the complete part layer for modelling the heat input to the layer compound,cf Figure 2). It can be derived that both the experimental (b) and numerical results (a) exhibit significant differences in temperature distribution perpendicular to the build direction. The difference in cooling behavior as shown in Figure 4 is due to the overhanging structure on the left side of the free-form area which features an inferior heat removal. This result is analysed in terms of element temperatures of monitoring points within the bulk and filigree free-form area of the turbine blade; compare Figure 5.

The plotted element temperatures are averaged over four nodes on the top surface of the 20th layer compound (build height: 5 mm) for both a monitoring point in the center of the bulk section and one in the free-formed area. In compliance with Figure 4(b), it can be seen that the time over 350 degrees of Celsius is higher within the filigree free-formed area compared to the massive bulk area. The reason for the temperature differences illustrated in Figures 4 and 5 is the heat transportation in reverse build direction. It is increased within the massive part regions (bulk section) compared to the free-formed section. In addition, the cool down rate for the bulk area is larger than for the filigree free-formed section. In laser beam melting, different cool down rates can influence the microstructure of parts [26]. Hence, by homogenization of the cool down behavior, the resulting microstructure could become more predictable. In addition residual stresses and deformations caused by the temperature gradient mechanism perpendicular to the build direction could be reduced.

Recapitulating, by utilizing a macroscale model to support process design, heat accumulations in, for example, free-formed part areas can be detected and could subsequently be avoided by adjusting laser power or scan velocity. For an economically efficient process design, the described simulation of the build-up process should be completed within a short period of time compared to the actual build time. To compensate for inaccuracies and to ensure part quality, process monitoring is performed to back up simulation results and to identify necessary refinements of modelling approaches.

In contrast to the numerical solution in Figure 4, a more detailed macroscale simulation approach was utilized to gather the results shown in Figure 5. Here, the heat input was modelled by accumulating the scan vectors (cf. Figure 2) to 10 scan areas which were applied with a temperature load of 1250°C for a load time corresponding to the scanning velocity (following [11]). On the one hand, the result accuracy should be increased through this measure because the thermal cycling of the elements due to the hatching of the laser (cf. Section 2) can be modelled more accurately. On the other hand, the calculation time for the thermal solution of 20 layers increased from 16 minutes to 215 minutes. The effect of this modelling approach on the result accuracy can be investigated in Figure 6 which shows the temperature curve of three elements within the first scan area (top right corner) of layer compound 20.

Thereby, elements on the left end of the scan area, in the center, and on the right end were chosen. Due to the fact that the spatial resolution is limited by the element size, the elements on the left end of the scan area were also within the selection of the second scan area which explains the peaks at about 1.4 s. Hence, this approach enables the modelling of additional temperature cycles for neighboring scan areas as discussed in Section 2. Furthermore, the approach is capable of modelling the contour exposure that completes the solidification of the current part cross section (peak at 2.5 s in Figure 6). Through heat conduction an increase in temperature can also be detected for the elements in the center and on the left at 2.5 s. It can also be seen that the general temperature level in Figure 6 is above approximately 190°C once the solidification of layer compound 20 is started (0.55 s), although the chosen preheat temperature is 80°C. This effect is caused by heat accumulation due to a restricted influence of the base plate on the heat conduction rate between part and base plate. Figure 7(b) shows a measured temperature evolution at different points of interest for

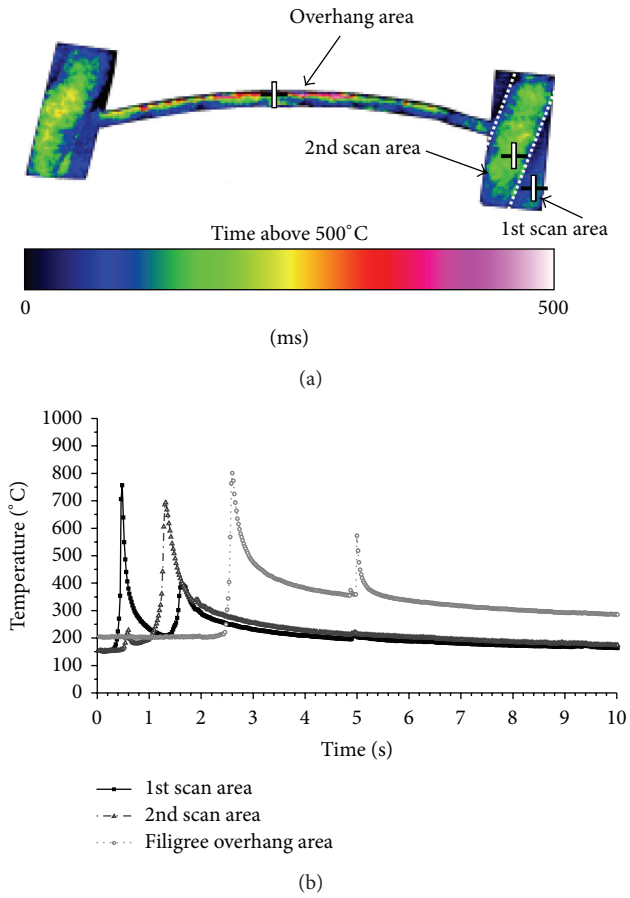

Figure 7: Experimental results obtained by thermography. Layer-integrated image showing time above 500°C level (a). Temperature evolution for different subareas at measurement points (b).

a corresponding part section during the process. The measured temperature level can be compared to the model (cf. Figure 6).

To enable a straightforward identification of hot spots, Figure 7(a) displays the geometrically mapped data for a characteristic layer-wise cool down time (derived from the total time above a certain temperature). Both the figure and the chart in Figure 7 describe the same physical background of delayed heat dissipation and can be used as a quality indicator. Furthermore, it can be concluded that the temperature evolution varies significantly between the first and second scan areas. After exposing the first scan area, the overall temperature in its vicinity increases and causes a slower cool down of the second scan area. In accordance with the numerically investigated temperature curves shown in Figure 5 the time above a fixed temperature (e.g., 350°C) is increased for the monitoring point within the free-formed area.

3.2. Microscale Level. The microscale model is intended to simulate the subsequent exposure of single tracks only. Compared to the macroscopic, part-based level, the temperature distribution and its temporal evolution can be investigated with an increased temporal and spatial resolution (micrometers and microseconds). A comparison of measurement data is only reasonable at the level of multiple scan tracks, taking into account the spatial and temporal averaging caused by the inertia of the measurement setup. To compare the numerical results of the microscale simulation with experimental data from thermography a modelled volume region of 250 μm × 250 μm × 40 μm is investigated by averaging corresponding nodal temperatures (cf. Section 2). This equals the pixel size of the measurement setup: compare Figure 8.

As introduced in Section 2 of this paper, hatching takes place on microscale level (10 μm, 10 μs) and states the main influence on temperature evolution through reheating (cf. Figure 8). Because of spatial (250 μm) and temporal (20 ms) resolution limits in the bolometric measurement setup, the layer-wise monitoring approach is mainly suitable for investigating the cooling behavior and long term temperature field evolution; compare Section 3.1. Due to spatial averaging the cooling behavior for single tracks is superimposed by the current temperature of its vicinity, resulting in a low frequency temperature rise as the heat source passes by.

To compare the simulation results—from both the micro- and the macroscale models—with the experimental results the width of the temperature curves and the cooling rates are investigated. Hereby, the width of a temperature curve is defined by the time; the temperature of an observed area region is above a fixed value of 500°C and cooling rate means the change with time of the temperature curve. The microscale model exhibits the fastest cooling rates compared to both the macroscale simulation and the experiments. Concerning the microscale model, the maximum cooling rate is −378.49°C/ms and the temperature peak width is 1.98 ms (Figure 8(a), first peak). As stated before, the thermography camera is not able to resolve the repeated heating cycles caused by neighbored hatches due to the inertia of the experimental setup. The maximum cooling rate measured with the bolometer is −1.74°C/ms and the width of the temperature curve is in this case 60.80 ms. These values broadly correspond with the results obtained from the macroscale simulation where a maximum cooling rate of −4.83°C/ms and a width of the temperature peak of 20.02 ms are observed.

4. Conclusions

Macroscale process modelling can be utilized to investigate the temperature field during the build process. Therefore, necessary adjustments to achieve a homogeneous temperature field perpendicular to the build direction can be identified upstream to the build process. As a result, the process design could be improved. In contrast to the state of the art, this would lead to an adjustment of process parameters within a part (e.g., increased scan velocity in the free-formed (cf. Figure 4) part area) in dependence on the wall thickness. To ensure the part quality and document the homogenized temperature field, the build-up process should be monitored, for example, by thermography.

On the macroscale level, abstract modelling approaches need to be applied for the virtual process design in order

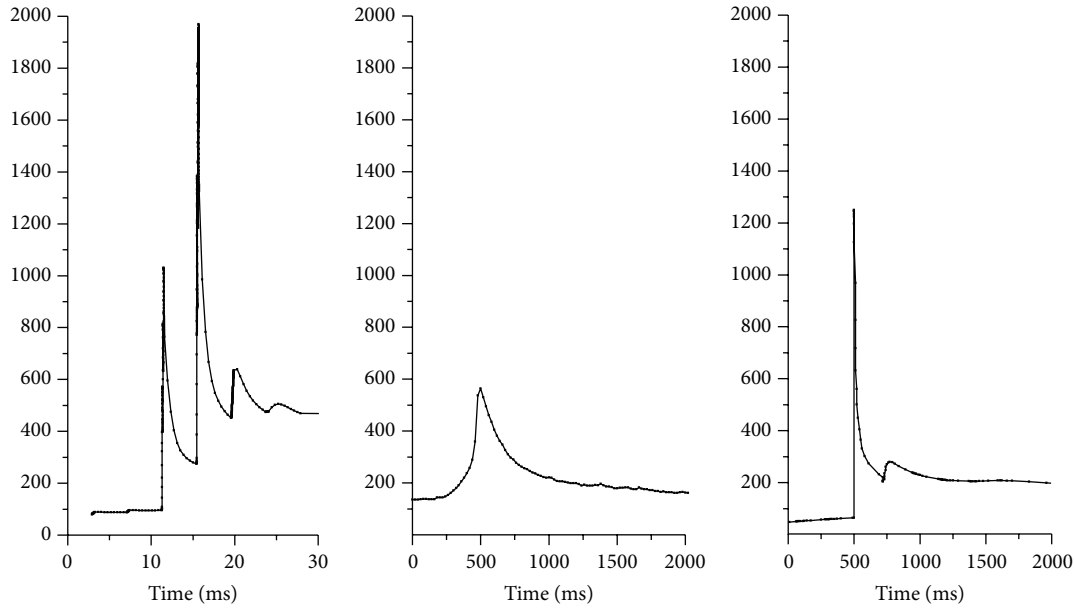

(a) Microscale hatch simulation [°C] (b) Bolometer measurement [°C] (c) Macroscale hatch simulation [°C]

Figure 8: Bolometer measurement of >40 hatches for fixed region of interest (b) compared with macroscale simulation results ((c), cf. Figure 5) and microscale simulation of several single hatches (a).

to gather numerical results within a computing time which is less than the build time of the part. To evaluate the accuracy of element temperatures (cf. Figures 5 and 8) process monitoring results should be considered. Thereby, the limitations of abstractions can be derived and users can decide whether they want to apply maximal calculation time efficient approaches or rather need increased result accuracy.

Process monitoring at the level of microseconds states an interconnection between microscale and macroscale modelling in the following way. Macroscale simulation cannot investigate random process irregularities on the part-based level but allows the prediction of possible systematic errors and deterioration of part quality and part deformations. Microscale modelling cannot handle full featured part geometries but allows a detailed understanding of realistic temperature cycles during hatching. Compared to macroscale modelling, the layer-wise process monitoring approach is capable of detecting geometry-dependent systematic and especially random irregularities during the manufacturing process by investigating the cool down behavior as the heat source passes by.

Future work comprises an integration of process monitoring and modelling. On a macroscale level, results from thermal imaging can be imported to the simulation system in order to perform a simulation of the resulting part's structural behavior, in particular, the resulting residual stress state which is cost intensive to measure. Furthermore, temperature profiles gathered through thermal imaging can contribute to the improvement of suitable abstraction methods for heat input modelling. On a microscale level, simulation results are of use for the calibration of measurement equipment and also for validating abstraction methods for macroscale modelling in terms of, for example, the energy intensity.

In addition, future work should focus on an improvement of both the simulation models and the experimental setup for thermal imaging. For an improved comparison of the microscale simulation model and the thermography results, an increase of temporal and spatial resolution compared to the setup used within this work is necessary.

Conflict of Interests

The authors declare that there is no conflict of interests regarding the publication of this paper.

Acknowledgment

The research leading to these results has received funding from the European Union's Seventh Framework Programme (FP7/2007–2013) for the Clean Sky Joint Technology Initiative under Grant agreement no. 287087.

References

[1] T. Wohlers, *Wohlers Report 2012: Additive Manufacturing and 3D Printing State of the Industry—Annual Worldwide Progress Report*, 2012.

[2] M. F. Zaeh and M. Ott, "Investigations on heat regulation of additive manufacturing processes for metal structures," *Annals of the CIRP*, vol. 60, no. 1, pp. 259–262, 2011.

[3] I. A. Roberts, C. J. Wang, R. Esterlein, M. Stanford, and D. J. Mynors, "A three-dimensional finite element analysis of

the temperature field during laser melting of metal powders in additive layer manufacturing," *International Journal of Machine Tools and Manufacture*, vol. 49, no. 12-13, pp. 916–923, 2009.

[4] M. F. Zaeh and G. Branner, "Investigations on residual stresses and deformations in selective laser melting," *Production Engineering*, vol. 4, no. 1, pp. 35–45, 2010.

[5] C. Seidel, M. F. Zaeh, J. Weirather et al., "Simulation of the laser beam melting process—an approach for an efficient geometry modelling of complex lightweight parts," in *Proceedings of the DGM LightMAT*, Deutsche Gesellschaft für Materialkunde e.V., 2013.

[6] T. A. Krol, S. Westhaeuser, M. F. Zaeh, J. Schilp, and C. Groth, "Development of a simulation-based process chain—strategy for different levels of detail for the preprocessing definitions," in *ASIM 2011-21. Symposium Simulationstechnik*, R. Boedi and W. Maurer, Eds., Winterthur, Del, USA, September 2011.

[7] N. Keller, F. Neugebauer, H. Xu, and V. Ploshikhin, "Thermomechanical simulation of ALM of titanium aerospace structures," in *Proceedings DGM LightMAT 2013*, e. V. Deutsche Gesellschaft für Materialkunde, Ed., 2013.

[8] T. A. Krol, C. Seidel, and M. F. Zaeh, "Prioritization of process parameters for an efficient optimisation of additive manufacturing by means of a finite element method," in *Proceedings of the 8th CIRP Conference on Intelligent Computation in Manufacturing Engineering*, vol. 12, pp. 169–174, 2013.

[9] C. Seidel, T. A. Krol, J. Schilp, M. F. Zaeh, and C. Groth, "Ansätze zur rechenzeiteffizienten Struktursimulation additiv gefertigter, filigraner Bauteile," in *Proceedings of the ANSYS Conference & 30th CADFEM Users' Meeting*, CADFEM GmbH, Ed., Kassel, Germany, 2012.

[10] C. Seidel, M. F. Zaeh, J. Weirather, T. A. Krol, J. Schilp, and D. Schmid, "Prozessnahe Modellierung des Materialverhaltens beim Laserstrahlschmelzen als Grundlage für die Ergebnisgenauigkeit hinsichtlich der Bauteilmaßhaltigkeit und des Eigenspannungszustandes," in *Proceedings of the ANSYS Conference & 31th CADFEM Users'Meeting*, CADFEM GmbH, Mannheim, Germany, 2013.

[11] C. Seidel, M. F. Zaeh, M. Wunderer, J. Weirather, T. A. Krol, and M. Ott, "Simulation of the laser beam melting process approaches for an efficient modelling of the beam-material interaction," in *Proceedings of the 8th International Conference on Digital Enterprise Technology*, Fraunhofer Institute for Industrial Engineering (IAO), Stuttgart, Germany, 2014.

[12] A. Otto and M. Schmidt, "Towards a universal numerical simulation model for laser material processing," *Physics Procedia*, vol. 5, pp. 35–46, 2010.

[13] A. Otto, H. Koch, K.-H. Leitz, and M. Schmidt, "Numerical simulations—a versatile approach for better understanding dynamics in laser material processing," *Physics Procedia*, vol. 12, pp. 11–20, 2011.

[14] A. Otto, H. Koch, and R. G. Vazquez, "Multiphysical simulation of laser material processing," *Physics Procedia*, vol. 39, pp. 843–852, 2012.

[15] C. Körner, E. Attar, and P. Heinl, "Mesoscopic simulation of selective beam melting processes," *Journal of Materials Processing Technology*, vol. 211, no. 6, pp. 978–987, 2011.

[16] E. Attar and C. Körner, "Lattice Boltzmann model for thermal free surface flows with liquid-solid phase transition," *International Journal of Heat and Fluid Flow*, vol. 32, no. 1, pp. 156–163, 2011.

[17] F.-J. Guertler, M. Karg, K.-H. Leitz, and M. Schmidt, "Simulation of laser beam melting of steel powders using the three-dimensional volume of fluid method," *Physics Procedia*, vol. 41, pp. 874–879, 2013.

[18] G. Pottlacher, H. Hosaeus, B. Wilthan, E. Kaschnitz, and A. Seifter, "Thermophysikalische Eigenschaften von festem und flüssigem Inconel 718," *Thermochimica Acta*, vol. 382, pp. 255–267, 2002.

[19] C. Sainte-Catherine, M. Jeandin, D. Kechmair, J.-P. Ricaud, and L. Sabatier, "Study of dynamic absorptivity at 10.6 μm (CO_2) and 1.06 μm (Nd-YAG) wavelengths as a function of temperature," *Journal de Physique*, vol. 1, pp. C7-151–C7-157, 1991.

[20] H. Krauss and M. F. Zaeh, "Investigations on manufacturability and process reliability of selective laser melting," *Physics Procedia*, vol. 41, pp. 815–822, 2013.

[21] A. Hussein, L. Hao, C. Yan, and R. Everson, "Finite element simulation of the temperature and stress fields in single layers built without-support in selective laser melting," *Materials and Design*, vol. 52, pp. 638–647, 2013.

[22] P. Fischer, V. Romano, H. P. Weber, N. P. Karapatis, E. Boillat, and R. Glardon, "Sintering of commercially pure titanium powder with a Nd:YAG laser source," *Acta Materialia*, vol. 51, no. 6, pp. 1651–1662, 2003.

[23] T. Craeghs, S. Clijsters, E. Yasa, and J.-P. Kruth, "Online quality control of selective laser melting," in *Proceedings of the Solid Freeform Fabrication*, University of Texas at Austin, 2011.

[24] T. Craeghs, F. Bechmann, S. Berumen, and J.-P. Kruth, "Feedback control of Layerwise Laser Melting using optical sensors," *Physics Procedia*, vol. 5, pp. 505–514, 2010.

[25] H. Krauss, C. Eschey, and M. F. Zaeh, "Thermography for monitoring the selective laser melting process," in *Proceedings of Solid Freeform Fabrication*, University of Texas, Austin, Tex, USA, 2012.

[26] L. Thijs, F. Verhaeghe, T. Craeghs, J. V. Humbeeck, and J. Kruth, "A study of the microstructural evolution during selective laser melting of Ti-6Al-4V," *Acta Materialia*, vol. 58, no. 9, pp. 3303–3312, 2010.

Hindawi Publishing Corporation
Advances in Mechanical Engineering
Volume 2014, Article ID 741083, 10 pages
http://dx.doi.org/10.1155/2014/741083

Research Article

Advanced Material Studies for Additive Manufacturing in terms of Future Gear Application

Jan Bräunig,[1] Thomas Töppel,[1] Bernhard Müller,[1] Martin Burkhardt,[1] Thomas Hipke,[2] and Welf-Guntram Drossel[2]

[1] *Fraunhofer Institute for Machine Tools and Forming Technology (IWU), 01187 Dresden, Germany*
[2] *Fraunhofer Institute for Machine Tools and Forming Technology (IWU), 09126 Chemnitz, Germany*

Correspondence should be addressed to Jan Bräunig; jan.braeunig@iwu.fraunhofer.de

Received 24 January 2014; Revised 1 April 2014; Accepted 6 May 2014; Published 26 June 2014

Academic Editor: Jens Günster

Additive manufacturing by laser beam melting is predestined for complex component geometry like integrated cooling channels without enormous posttreatment processing. To investigate the influence of build-up direction in terms of later tooth excitation of gear-wheels, first fundamental material analyses were accomplished in this publication. Therefore, additively produced specimens were used to determine the build-up direction dependent elastic properties of the material in all three spatial directions based on tensile and torsion tests. The anisotropies of elastic limits and breaking points of previous studies were confirmed in this paper. Furthermore, torsion values were also determined depending on build-up direction. Laser beam melted X3NiCoMoTi18-9-5 (hot-work tool steel) was shown to exhibit extremely high performance under shear loading in comparison to conventionally processed steel. The influence of build-up direction on torsional strength was also shown.

1. Introduction

In recent years, additive manufacturing has become a reliable tool for custom small-batch production or for prototyping and has accelerated the conversion of CAD designs into reality. The process is dependable, reduces design lead times, and offers new geometric possibilities, which is why, in addition to its use in prototyping applications, it could also be considered for use in traditional mechanical engineering if the respective boundary conditions are favourable. With additive manufacturing, limits of producibility of conventional manufacturing are no longer valid, especially for the generation of geometries with undercuts and internal free-form cavities, opening up new possibilities for the production of gears. Researchers are currently working on increasing the efficiency of tooth contact, which they hope to achieve by integrating coolant channels into tooth flanks [1], see Figure 1.

Another possible application is the production of acoustically optimised wheel bodies, which require complex geometric shapes according to [2].

However, the material properties of additively manufactured components are not directly comparable to those of conventionally produced parts. In detail, this paper describes the mechanical analysis of the properties of additively processed, laser beam melted hot-work tool steel X3NiCoMoTi18-9-5 (material number 1.2709) which is not suitable for an application in gears but shows equal effects between different build-up directions. Qualification of the gear material 16MnCr5 for the laser beam melting process is current state of research and will be ready for industrial use in the medium term.

2. State of Research into the Material Properties of Laser-Fused Components

The additive manufacturing process of laser beam melting in use at the Fraunhofer Institute for Machine Tools and Forming Technology (IWU) applies a thin layer of powder and then melts it selectively with a laser. The microstructure of this fused material has a substantial influence on the material's mechanical properties. According to [3], rapid cooling of the fused material produces a very fine-grained microstructure, which in turn leads to high hardness values

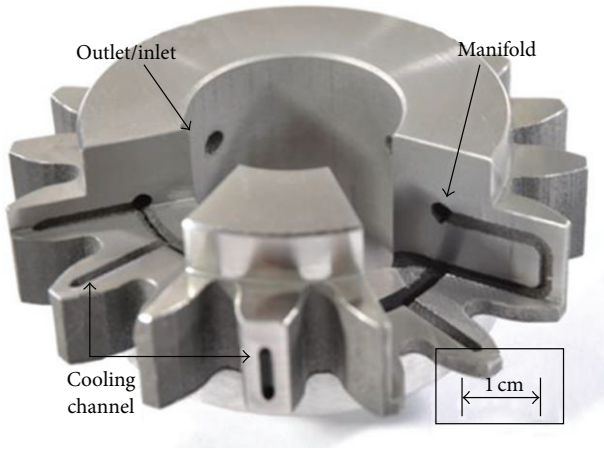

Figure 1: Additive manufactured gear with integrated coolant channels [1].

and brittle material behaviour. Slow cooling, in contrast, favours the formation of large grains, which reduces hardness values and has a negative impact on ductility. Elastic properties, however, are not determined by grain size but rather by interactions between lattice atoms. Thus, according to [3], the characteristic values for elasticity are not influenced by the parameters of the manufacturing process. Contrast this with [4], where it was published that the modulus of elasticity is dependent on the laser energy used. It was demonstrated concretely that the use of a 1,000 Watt laser system led to the formation of a strong alignment parallel to the build-up direction.

As a result, an increase in the modulus of elasticity was detectable. This leads to the conjecture that the high energy input from the laser causes a directional solidification of the crystallites and thus a kind of growth structure. However, no further description is given of the process parameters, and so only a limited assessment of the conclusions is possible. Reference [5] offers another possible explanation for the general dependence of the modulus of elasticity on the laser energy. The density and modulus of elasticity of test specimens are shown to be related to the laser scanning speed. Since all other process parameters were held constant for the tests, the input energy can be extrapolated directly from the scanning speed. As the scanning speed increases and thus the energy input drops, the density clearly decreases and the modulus of elasticity falls. This is consistent with the reasoning of [3], which states that the modulus of elasticity is dependent on the interatomic distance and not on the microstructure. Therefore, the elastic properties can be influenced by the selection of parameters for the manufacturing process.

Aside from the influence of process parameters on material properties, a relationship between build-up direction, stress direction, and respective strength values was demonstrated in several papers (e.g., [3, 4, 6–8]). From this it can be assumed that the bonds between two successive layers differ from those within one layer, thus resulting in different properties.

Furthermore, [8] determined that powder from different manufacturers can lead to different moduli of elasticity and strength values in manufactured specimen. The dependences cited has been demonstrated several times, but the influencing variables are so numerous and varied that only a few characteristic values of additively manufactured steels are currently included, for example, in technical guideline VDI 3405 (part 2).

Moreover, the process parameters are adapted individually to each application and therefore hardly comparable. The load capacities of components cannot be calculated reliably without knowing the exact material characteristics, meaning that these values must be determined individually for the respective process parameters. Based on the assumption that the microstructure within one layer forms homogeneously, it can be assumed that the characteristic values of the material within that layer are directionally independent. This tendency has already been demonstrated in [7] for hardness values. If this can also be confirmed for the elastic properties, it will be possible to fully describe the elastic behaviour of additively manufactured components using a transversely isotropic material model. This will require determination of five independent material parameters, consisting of the modulus of elasticity, the shear modulus, and Poisson's ratio (E_1, E_3, G_{13}, ν_{12}, and ν_{13} if the additive layer corresponds to layer 12; see Figure 8), for the respective additive manufacturing process.

In this paper, tensile and torsion tests are used to demonstrate the validity of the material model and to reveal the necessary characteristic values of the tested hot-work tool steel X3NiCoMoTi18-9-5. The measured material properties are also related to each other in accordance with the assumptions of a transversely isotropic material model. The following gives an explanation of the tests as well as a presentation of the results obtained. The current state of laser beam melting technology does not yet offer a quenched and tempered steel for gear tooth applications, such as 16MnCr5 which would be processable with laser beam melting on commercially available laser beam melting machines. Therefore, these tests will first be applied to material X3NiCoMoTi18-9-5, even though it is known that this material is not suitable for gear teeth. Nevertheless, the results that are obtained will be

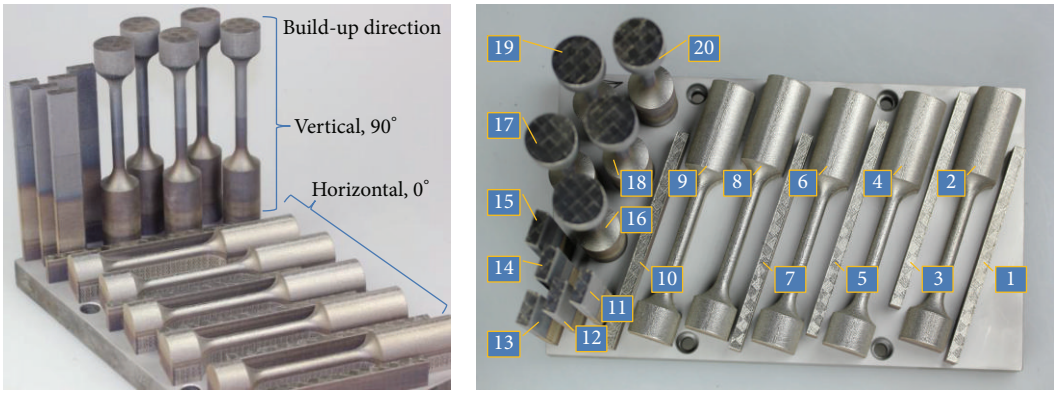

(a) (b)

FIGURE 2: Additive manufacturing process samples with different build-up directions (a) and numbering of specimens (b).

translatable to future additive processing of a material like 16MnCr5.

3. Experimental Tests

Tensile and torsion tests were performed to determine the five independent material parameters. The test specimens that were required for this were all produced with an angle of 0° or 90° between the build-up direction and the longitudinal axis of the specimen. As such, they are also referred to as having a vertical or horizontal build orientation. Five specimens were produced for each test and each build orientation. The time needed to fuse one material layer during the laser beam melting process depends in large part on the size of the regions to be fused. The smaller the area to be fused in one layer, the faster the next powder layer can be applied and fused. This shortens the intervals between laser energy inputs into the component, thus increasing the base temperature in the built-up (fused and solidified) regions of the specimen. This is believed to be the reason for the differently coloured material regions (annealing colour) of the vertical blanks in Figure 2(a). The individual specimen locations were measured and documented for later comparison with actual location of fracture in order to determine what level of influence these areas have on location of fracture. The manufacturing of the specimens was performed on a "Concept Laser M2 cusing" laser beam melting machine with a random chessboard scanning strategy ($5 \times 5\,\text{mm}^2$ chessboard subfield size), an diode-pumped fibre laser with 400 W nominal power, continuous wave, and the following build-up parameters:

(i) laser power: 187 W

(ii) scan speed: 600 mm s^{-1}

(iii) hatching: 0.105 mm

(iv) layer thickness: 0.03 mm.

3.1. Tensile Tests. Uniaxial tensile tests were used to determine the moduli of elasticity and Poisson's ratios for the different spatial orientations of the additive manufacturing process. The geometry of the test specimens was based on DIN 50125 for these tests. Additional conventional machining steps such as turning and grinding were necessary based on the tolerances and surface roughness required for tensile specimens. Tensile specimen strain was measured via the optical method of grey value correlation using an ARAMIS-12 M measuring system of Gesellschaft für Optische Messsysteme (GOM mbH, Braunschweig/Germany). This reduced the impact of the rigidity of the tensile testing machine on the measurements and made it possible for the longitudinal and transverse strain to be determined at each point in time during testing. In order to minimise the measurement uncertainty resulting from this method, it was necessary to select a large enough stochastic sample or number of measurement facets on the specimen surface (according to photooptical aspects). Thus, an appropriate specimen cross section was required. In the end, preference was given to a square specimen cross section with a side length of 5 mm and a parallel initial length of 25 mm. This cross section was confirmed with the measuring system in pretests (Figure 3).

The tensile tests were carried out on an Inspekt universal testing machine made by Hegewald & Peschke MPT GmbH, Nossen/Germany (Figure 3(a)). The longitudinal and transverse strains of two mutually perpendicular specimen sides had to be analysed, and so both sides had to be recorded by the optical measuring system during the entire test. The test setup was thus arranged to allow each camera of the ARAMIS system to record both sides of the specimens. A sample camera image is shown in Figure 4(b). This made it possible to record the deformation of both sides of the specimens and to determine elastic material characteristics for the entire test duration. The force signal of the tensile testing machine was fed to the ARAMIS system to allow strain values to be linked to the associated specimen stress. As recommended in DIN EN ISO 6892-1, the crosshead speed was set to 0.8 mm/min for the elastic region and 5.0 mm/min for the plastic region.

The stress-strain curves for all tensile test specimens are shown in Figure 5. Specimen number assignments can be found in Figure 2(b). There is a noticeable difference between the curves of vertically oriented (specimens 11 to 15) and

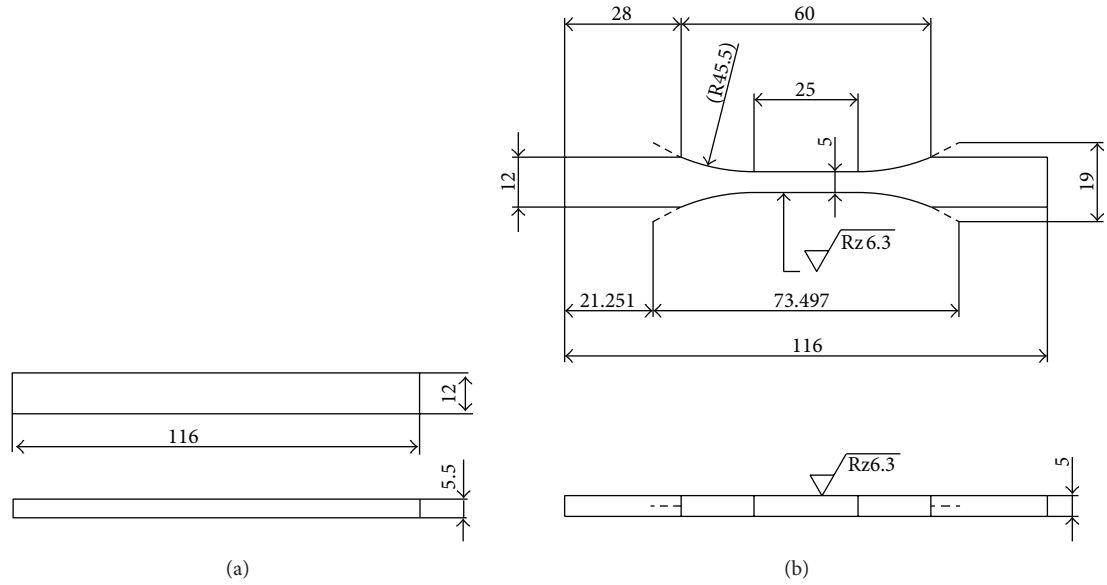

Figure 3: Laser beam melted workpiece (a) and machined specimen (b) geometry for tensile test.

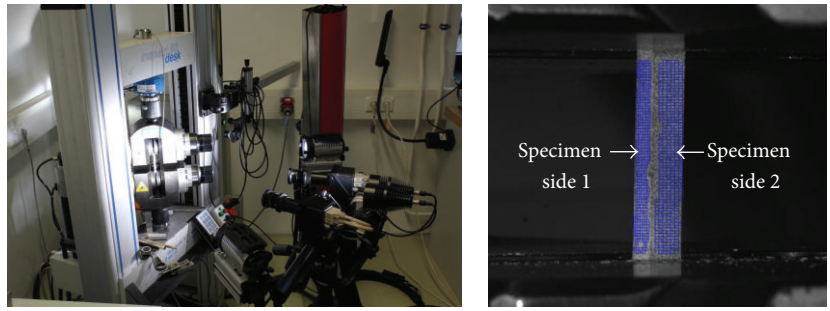

Figure 4: Test setup (a) and ARAMIS system camera image of the clamped specimen (b).

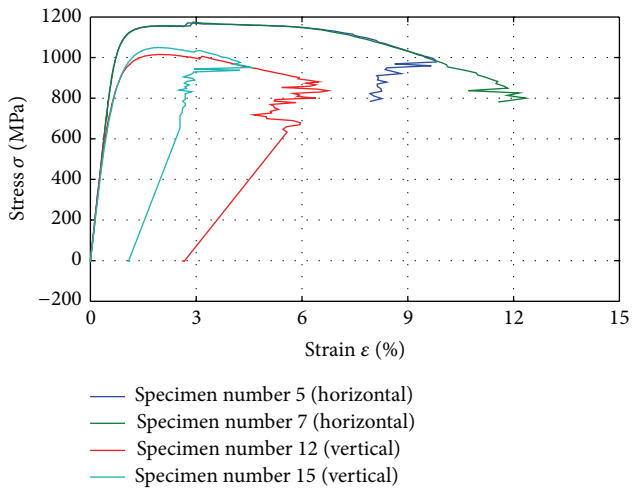

Figure 5: Stress-strain curves for specimens 5, 7 (horizontal build-up direction) and 12, 15 (vertical build-up direction) subjected to tensile testing.

horizontally oriented (specimens 1 to 10) tensile specimens. Once the ultimate tensile strength is exceeded, any further increase in stress results in a proportionately larger drop in strain followed quickly by material failure.

Different material behaviour depending on specimen orientation in manufacturing cannot be explained solely by the grain size of the material's microstructure. It is conjectured that grain size is different for the two build-up directions, since, as previously explained, the processing time per layer of the vertically oriented specimens is shorter and the energy input occurs in shorter intervals. This results in a slower cooling of the material, which thus tends to have a larger grain size.

The horizontally oriented specimens exhibit high tensile strength and ductility, whereas the vertically oriented specimens tend to exhibit lower strength and rather brittle behaviour. The sharply divergent ductility can be regarded as an indicator for small grains in the horizontally oriented specimens and large grains in the vertically oriented specimens. The high strength and ductility exhibited by the

Table 1: Results of tensile tests.

Specimen	Build-up direction	Young's modulus in GPa			0.2% yield strength in MPa			Tensile strength in MPa
		Side 1	Side 2	Average	Side 1	Side 2	Average	
1	Horizontal	156.0	157.9	157.0	1101.4	1093.9	1097.6	1160.9
5	Horizontal	155.1	156.6	155.9	1076.4	1073.3	1074.8	1170.4
7	Horizontal	154.7	158.9	156.8	1079.7	1083.7	1081.7	1174.6
10	Horizontal	152.2	154.3	153.2	1086.4	1089.5	1087.0	1174.1
11	Vertical	154.9	148.2	151.5	862.7	839.8	851.3	1004.4
12	Vertical	148.7	148.9	148.8	868.6	852.6	860.6	1015.7
13	Vertical	152.0	161.6	156.8	883.3	878.7	881.0	1069.5
14	Vertical	148.9	155.2	152.0	880.2	876.4	878.3	1025.9
15	Vertical	142.0	147.6	144.3	892.1	905.6	898.8	1049.5

horizontally oriented specimens and the lower strength and rather brittle behaviour of the vertically oriented specimens lead to the conjecture that the formation of a fine-grained or coarse-grained microstructure depends on the specimens' orientation in the build job. This means that the higher base temperature of the vertically oriented specimens, in addition to causing the differently coloured regions, also influences microstructure formation.

In order to minimise the impact of different grain sizes and to enable a targeted investigation of any further effects, the process parameters should be selected so that the energy input is independent of the specimens' orientation in the build job and the component geometry. This will ensure comparable heat influence and microstructure formation in all cases. Otherwise, the material relationships will be very complex, making it difficult to assess the load capacity of additively manufactured components. It must also be noted that the stress-strain curves of all horizontally oriented specimens exhibit a small spread. The specimen position on the build platform during the manufacturing process was not observed to have an influence on strength values. However, the ultimate tensile strengths that were determined for the vertically oriented specimens exhibit relatively large differences. It seems that individual local failure sites within a layer have a much larger effect in the case of small cross-sectional areas built up per layer.

The ultimate tensile strength of a specimen corresponds to the maximum stress occurring during the test. The largest stress value was determined for each specimen, and a mean value was calculated for all the specimens with a given orientation in the build job. The resulting value corresponds to the ultimate tensile strength of the respective angular orientation. Furthermore, the modulus of elasticity and the 0.2% yield strength can be determined directly from the stress-strain diagram.

The modulus of elasticity corresponds to the slope of the linear elastic region. Thus, a regression line was determined for each specimen at a sufficient distance from the beginning and end of the elastic region. The slope of this regression line corresponds to the modulus of elasticity. The mean value for each angular orientation in the build job was in turn derived from these determined values.

It can be seen in the stress-strain curve that the tested material has no pronounced yield strength, and so the transition from the elastic region to the plastic region is defined with a constant strain of 0.2% [9]. In order to determine the associated yield stress $R_{p0.2}$, a line was plotted through $\varepsilon = 0.2\%$ parallel to the linear elastic region, and its point of intersection with the stress-strain curve was determined. The stress value obtained by this method corresponds to the yield strength of the specimen. A detailed list of the test results can be found in Table 1. An ultimate tensile strength of 1100 MPa is indicated for conventionally produced, untreated X3NiCoMoTi18-9-5. Additively manufactured steel parts thus exhibit the same performance as with conventional manufacturing.

As in previous studies, these tests demonstrated the dependence of strength values on the specimens' angular orientation in manufacturing. Vertically oriented components have an approximately 20% lower yield strength and an approximately 12% lower ultimate tensile strength under application of the selected production parameters. The expected anisotropy of the moduli of elasticity could not be precisely demonstrated, however. Nevertheless, the directional dependence must be acknowledged based on the measurements of all specimens and cannot be attributed to measurement uncertainty. However, the relationship between the anisotropic material parameters was shown and can be trusted. Solely, the exact values are uncertain. The extent to which this small difference has an impact on the design of components and whether it needs to be taken into consideration at all will have to be decided on a case-by-case basis.

In addition to Table 1 the following Table 2 presents the relevant statistic values of all specimen. Because of the small quantity of tested specimens, there is no usual statistical coverage. Otherwise, the available space was fully exploited as shown in Figure 2.

Poisson's ratio ν corresponds to the negative ratio of transverse strain to longitudinal strain. The Poisson's ratio for each specimen and specimen side was determined by creating a diagram with transverse strain over longitudinal strain and then plotting the regression line in the elastic region. The slope of these lines thus corresponds to the negative of

Table 2: Statistic values of tensile tests.

Build-up direction	Statistic value	Young's modulus in GPa	0.2% yield strength in MPa	Tensile strength in MPa	Poisson's ratio	
					Side 1	Side 2
Horizontal	Arithmetic average	155.71	1085.54	1170	0.3154	0.41715
	Standard degression	1.9858	8.7228	5.4986	0.0282	0.0205
Vertical	Arithmetic average	150.80	874.00	1033.00	0.3528	0.3353
	Standard degression	5.1021	18.0649	23.5464	0.0465	0.0198

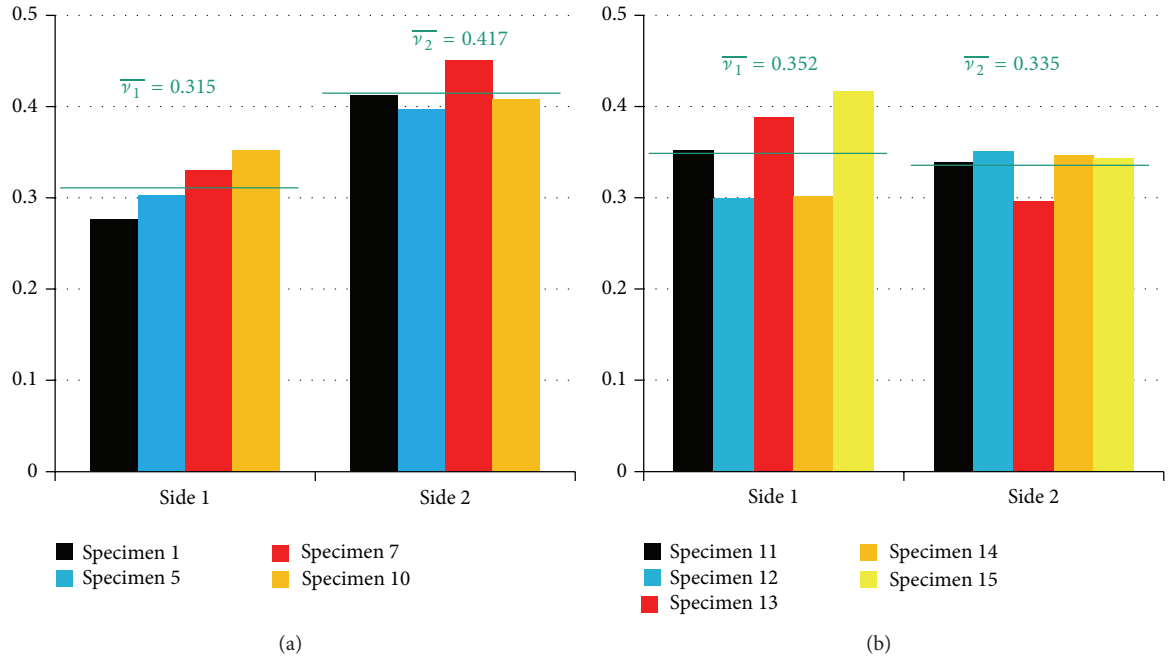

Figure 6: Poisson's ratios ν determined for two adjacent perpendicular specimen sides of each specimen and the resultant mean values, horizontal build-up direction (a) and vertical build-up direction (b).

Poisson's ratio. The mean values were then determined for each build-up direction and specimen side, and all the values were summarised in Figure 6.

Clearly, the Poisson's ratios of the two sides differ in the case of the horizontally oriented specimens. The values from specimen side 1 represent the transverse contraction within an additive layer when the load is acting on that layer. Based on the results, it can be seen that this contraction is smaller than the contraction of layers lying on top of one another at the same point in time. The directional dependence of the Poisson's ratio for horizontally oriented specimens was thus demonstrated. The results are less clear for the vertically oriented specimens. The transverse contractions of side 1 and side 2 both indicate the deformations within the levels when the load is acting perpendicular to them. Therefore, identical results were expected for both sides. Based on the measured values, however, this conformity could not be precisely demonstrated. Even so, the deviations are considered to be relatively small, such that the transverse contraction within an additive layer is characterised as virtually direction independent.

3.2. Torsion Tests. Torsion tests were used to determine the torsion-specific elastic properties and strength values and to check the assumption of the following equation:

$$G_{12} = \frac{E_1}{2\left(1 + \nu_{21}\right)}. \quad (1)$$

A precise determination of the shear modulus requires that only shear stresses occur during the test and that no axial stress components be superimposed on them. A circular cross section is used for the specimens to avoid the occurrence of bulging and the accompanying axial stresses (St. Venant torsion) in the specimen cross section. The torsion tests were carried out in accordance with DIN EN ISO 6892-1 and the tensile test with DIN 50125. The means of clamping the specimen to the test machine was adapted to the features of the machine being used, and so a square cross section was implemented on the ends of the specimens. The largest possible transition radius was chosen in order to avoid notch effects and the accompanying impact on the stress state in the transition from the round cross section to the square cross

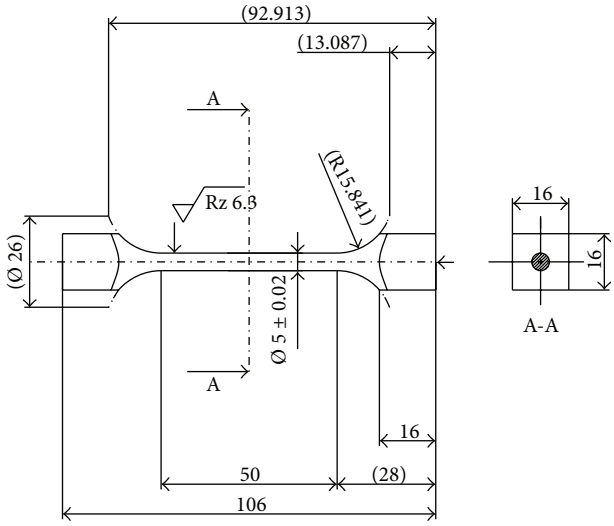

Figure 7: Specimen geometry for torsion tests.

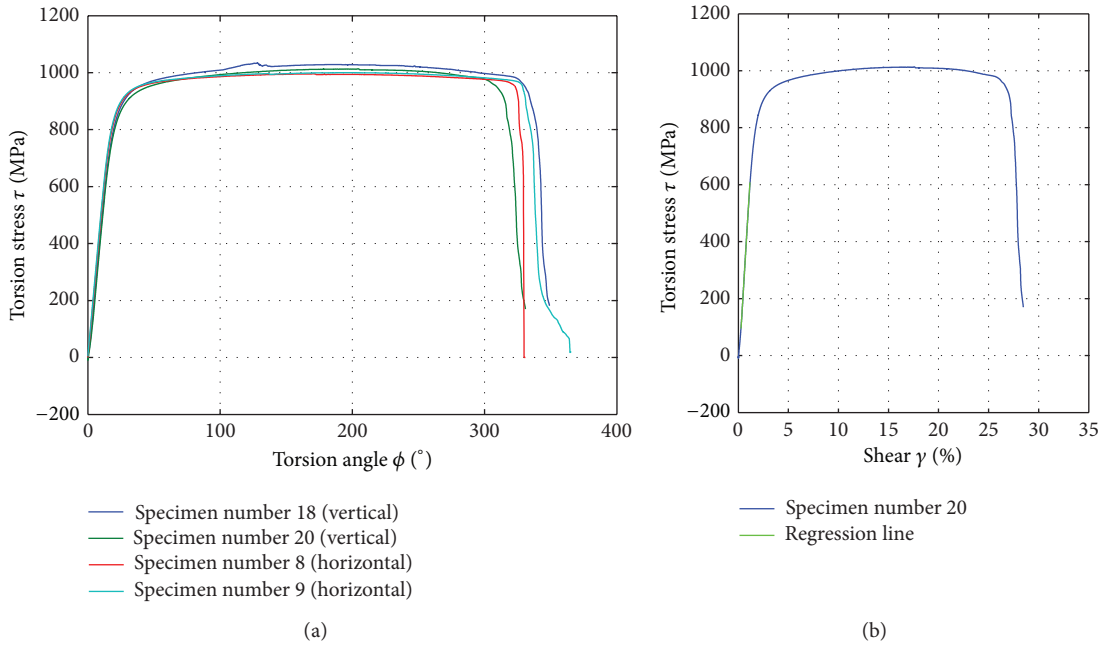

Figure 8: Curve of torsional stress over angle of rotation for all specimens ((a) specimens 8, 9: horizontal build-up direction and specimens 18, 20: vertical build-up direction) and curve of torsional stress over shear ((b) specimen 20).

section. According to [10], relationship between the diameter d of the circular cross section and the parallel specimen length L should be expressed by $L = 10d$. The selected specimen geometry fulfills this requirement and is shown in Figure 7.

The stress rates recommended in DIN EN ISO 6892-1 for tensile testing were converted for torsion stresses in order to define the test speeds. This DIN standard gives different stress rates in the elastic region based on the magnitude of the modulus of elasticity and makes recommendations for the stress rate in each case. However, the physical variable that can impact material behaviour is not the rate of stress increase but rather the rate of strain increase. The classification according to moduli of elasticity takes this fact into account and specifies mostly constant strain rates. This was likewise taken into account when making the conversions for the torsion test, by equating the strain and shear rates. When the stress rate, modulus of elasticity, and shear modulus are inserted, the result is

$$\frac{\dot{\sigma}}{E} = \frac{\dot{\tau}}{G}. \tag{2}$$

If $\dot{\sigma} = 15\,\text{MPa/s}$, $E = 210\,\text{GPa}$, and $G = 81\,\text{GPa}$, the result is a stress rate for the torsion test of $\dot{\tau} = 5.78\,\text{MPa/s}$. This is

Table 3: Characteristic values derived from the stress-shear diagram (mean values, in MPa).

Build-up direction	Statistic value	Modulus of shear	0.4% yield strength	Torsional strength
Horizontal	Arithmetic average	57487	868	989
	Standard degression	1.28	26.80	12.32
Vertical	Arithmetic average	57110	845	1022
	Standard degression	0.90	9.66	7.13

converted to torsional rate via the specimen geometry. As a result, a control rate of $\dot{M} = 0.1429\,\text{Nm/s}$ was used in the elastic region. For the plastic region, the strain rate is raised to 26 times that of the tensile test. However, with no further increase in the stress, the torque can no longer be used as a control. Therefore, a constant angular rate of $\dot{\phi} = 4.45^\circ/\text{s}$ was specified.

The tests were carried out on a *Zwick Roell* Z050 material-testing machine with torsion module. Figure 8(a) shows the resulting curve of torsional stress over angle of rotation for all specimens. Unlike in the tensile test, there are no significant differences to be seen here between the individual curves or, consequently, between the build-up directions of the specimens. Moreover, the very large maximum twist angle at break of 260° to 360° is notable. Accordingly, components produced additively via laser beam melting exhibit an extremely high torsional ductility regardless of build-up direction. The characteristic values in the stress-shear diagram were determined as in the tensile test. The following equation can be used to convert the measured torsion angle ϕ to the shear γ on the specimen surface, where r represents the specimen radius and L the parallel initial length:

$$\gamma = \frac{\phi}{L} \cdot r. \tag{3}$$

This results in the stress-shear curve, as shown in Figure 8(b) for specimen 20. As with the modulus of elasticity, the shear modulus corresponds to the slope of the regression lines in the elastic region. However, the transition to plastic behaviour is defined as a constant shear of 0.4% [11]. The mean values of the characteristics for both build-up directions were likewise determined and are summarised in Table 3.

The torsional values are also seen to exhibit a dependence on the specimen orientation. However, this dependence is smaller than that seen in the tensile test. The yield strength of the vertical orientation is 3% lower than that of the horizontally orientated, whereas their torsional strength is 3% higher. No clear anisotropy is detectable for the shear modulus.

4. Results and Discussion

The following equations, according to [12], can be used for converting elastic limit and yield strength to torsion or shear values for conventionally produced steel under normal stress:

$$\tau_m = f_\tau \cdot R_m, \tag{4}$$

$$\tau_{p0.4} = f_\tau \cdot R_{p0.2}. \tag{5}$$

For (5), the shear strength factor $f_\tau = 0.577$ appears in the literature for case-hardened steel, stainless steel, forged steel, and other steels. Thus, the bearable stresses under shear loading are 42.3% lower than under tensile loading. This comparison can also be made for the laser beam melted material based on the characteristic values determined in the tests. This results in

$$\begin{aligned} 0.8 &< f_{\tau\_\text{horizontal}} < 0.85, \\ 0.97 &< f_{\tau\_\text{vertical}} < 0.99. \end{aligned} \tag{6}$$

The torsional and shear capacities of additively processed steel are thus considerably higher than those of conventional steel. The strength values that were determined for the vertically orientated specimens were virtually the same whether under tensile or shear loading.

To determine how closely the behaviour of laser beam melted components corresponds to the transversely isotropic material model, the measurements are inserted into the required relationships between material constants. The label of the elastic material properties for the different spatial directions is based on the definition of Figure 8. The shear modulus G_{12}, with a value of $G_{12} = 57.11\,\text{GPa}$ corresponds to the value determined in the test for vertically structured specimens. The calculated shear modulus value based on the required relationship and the measured Poisson's ratio of side 1 of the specimen with horizontal build-up direction (see Figure 6(a)) comes to

$$G_{12} = \frac{E_1}{2\left(1 + \nu_{21}\right)} = \frac{156\,\text{GPa}}{2\,(1 + 0.3154)} = 59.54\,\text{GPa}. \tag{7}$$

Furthermore, from the measured transverse contractions of the vertically orientated specimens' results (Figure 6(b)),

$$\nu_{31} = \nu_{32} = \frac{0.352 + 0.335}{2} = 0.3435. \tag{8}$$

This follows in

$$\begin{aligned} \frac{\nu_{13}}{E_3} &= \frac{0.4175}{151\,\text{GPa}} = 0.0028\,\text{GPa}^{-1}, \\ \frac{\nu_{31}}{E_1} &= \frac{0.3435}{156\,\text{GPa}} = 0.00202\,\text{GPa}^{-1}. \end{aligned} \tag{9}$$

The result of (7) is not the same as the measured value ($G_{12} = 57.11\,\text{GPa}$). Furthermore, (9) do not meet the requirements of the transversely isotropic material model $\nu_{13}/E_3 = \nu_{31}/E_1$. Therefore, the expected material behaviour with respect to the assumed model could not be precisely

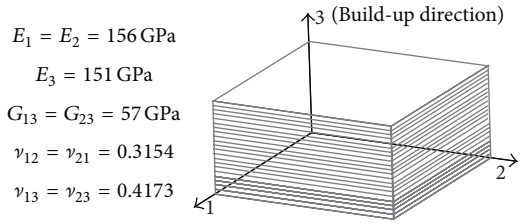

Figure 9: Elastic values for laser beam melted X3NiCoMoTi18-9-5 and definition of the spatial directions.

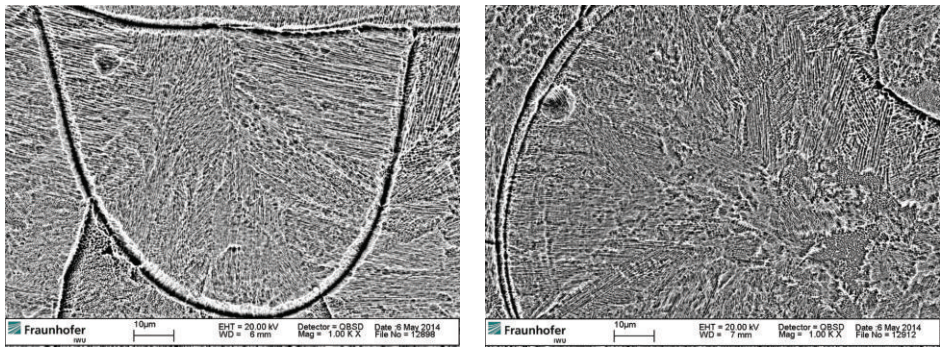

(a) (b)

Figure 10: Micrograph horizontal viewing ((a) vertical axis corresponding to build-up direction) and downwards viewing ((b) horizontal layer).

confirmed on the basis of the measured values. Values for G_{12} and ν_{31} are also necessary for a complete description of the elastic behaviour. Nevertheless, the differences between the actual properties in the tests and the transversely isotropic model are marginal that transversal isotropy can be assumed for approximate calculations. The resulting errors are comparatively small.

Additional detailed materials testing is required to confirm the demonstrated relationships. Apart from the current literature's confirmation of strength value dependences, this paper was also able to demonstrate the extremely high torsion strength of laser beam melted components with vertical as well as horizontal build-up direction. As previously justified, additional calculations are carried out using the transversely isotropic material model. The elastic constants of this model are summarised and illustrated in what follows for the case where direction 3 corresponds to the build-up direction (Figure 9).

The differently coloured regions (annealing colour, shown in Figure 2) resulting from the production process were not shown to have any influence on the sites of fracture in the tensile or torsional specimens. Despite colour variations in the vertically orientated specimens, the fractures occurred, as expected, in the parallel part of the specimen, right in the middle.

5. Summary and Future Prospects

Specimens that were produced additively via laser beam melting were used to determine the build-up direction dependent elastic properties of the material in all three spatial directions based on tensile and torsion tests, and the transversely isotropic material model was validated for initial approximate calculations. Furthermore, the anisotropies of elastic limits and breaking points as demonstrated in previous studies were confirmed. Torsion values were also determined depending on build-up direction. Laser beam melted X3NiCoMoTi18-9-5 (hot-work tool steel) was shown to exhibit extremely high performance under shear loading in comparison to conventionally processed steel. The influence of build-up direction on torsional strength was also shown to be negligible. A first view with a scanning electron microscope shows no significant difference between vertical and horizontal build-up direction of dendritic solidified structures (Figure 10). In addition, detailed investigations in microstructure and grain size are planned to prove the theory depending on the orientations under these build-up boundary conditions.

Following these tests, FE (finite-element) mesh models of spur and helical gear teeth will be generated. The background is to send on the stiffness data for these numeric mesh models and consider variable transmission errors dependent on the angle of rotation, respectively, on the build-up orientations. Furthermore, tests using a gear test rig are scheduled. Reconciling the test results with reality will also require a study of whether the material-removal processes used to increase gear tooth quality, for example, profile grinding, reveal directionally dependent properties as part of the material-removal behaviour. At the same time, attempts will be made to qualify typical gear-tooth materials for laser beam melting.

Conflict of Interests

The authors declare that there is no conflict of interests regarding the publishing of this paper.

References

[1] T. Kamps and G. Reinhart, "Increasing transmission efficiency by implementation of a conformal cooling system using additive manufacturing," in *Proceedings of the Fraunhofer Direct Digital Manufacturing Conference (DDMC '14)*, A. Demmer (Hrsg.), Ed., Fraunhofer, Stuttgart, Germany, 2014.

[2] K. Engel, *Analyse der Körperschalleitung mit sensorischen, optischen und numerischen Verfahren am Beispiel von Zahnradkörpern [Ph.D. thesis]*, Technische Universität Clausthal, 1996.

[3] O. Rehme and C. Emmelmann, *Generative Fertigung von Ti-Legierungen: Laserstrahl versus Elektronenstrahl*, Werkstoffe in der Fertigung, 2007.

[4] T. Niendorf, S. Leuders, A. Riemer, H. A. Richard, T. Tröster, and D. Schwarze, "Highly anisotropic steel processed by selective laser melting," *Metallurgical and Materials Transactions B*, vol. 44, no. 4, pp. 794–796, 2013.

[5] A. P. Roberts, G. Grayson, V. J. Challis et al., "Elastic moduli of sintered powders with application to components fabricated using selective laser melting," *Acta Materialia*, vol. 59, no. 13, pp. 5257–5265, 2011.

[6] O. Rehme and C. Emmelmann, "Rapid manufacturing of lattice structures with selective laser melting," in *Laser-based Micropackaging*, vol. 6107 of *Proceedings of SPIE*, January 2006.

[7] J. Sehrt and G. Witt, "Auswirkung des anisotropen Gefüges strahlgeschmolzener Bauteile auf mechanische Eigenschaftswerte," *RTejournal*, vol. 6, no. 1, 2009.

[8] G. Reinhart, S. Teufelhart, and F. K. E. Riss, "Examination of the geometry-dependent anisotropic material behavior in additive layer manufacturing for the calculation of mesoscopic lightweight structures," in *Proceedings of the Fraunhofer Direct Digital Manufacturing Conference*, Berlin, Germany, March 2012.

[9] J. Rösler, M. Bäker, and H. Harders, *Mechanisches Verhalten der Werkstoffe*, Vieweg Studium, Vieweg+Teubner/GWV Fachverlage, Wiesbaden, Germany, 3 edition, 2008.

[10] H. Blumenauer, *Werkstoffprüfung*, Deutscher Verlag für Grundstoffindustrie, Leipzig and Stuttgart, Germany, 6 edition, 1994.

[11] D. Muhs, D. Jannasch, and J. Voßiek, *Roloff/Matek Maschinenelemente: Normung, Berechnung, Gestaltung*, Viewegs Fachbücher der Technik, Friedr. Vieweg & Sohn, Wiesbaden, Germany, 18 edition, 2007.

[12] B. Hänel, *Rechnerischer Festigkeitsnachweis für Maschinenbauteile aus Stahl, Eisenguss- und Aluminiumwerkstoffen*, VDMA-Verl, FKM-Richtlinie, Frankfurt am Main, Germany, 5 edition, 2003.

Hindawi Publishing Corporation
Advances in Mechanical Engineering
Volume 2014, Article ID 491581, 6 pages
http://dx.doi.org/10.1155/2014/491581

Research Article

Powder-Bed Stabilization for Powder-Based Additive Manufacturing

Andrea Zocca,[1] Cynthia M. Gomes,[1] Thomas Mühler,[2] and Jens Günster[1,2]

[1] *Division of Ceramic Processing and Biomaterials, BAM Federal Institute for Materials Research and Testing, Unter den Eichen 44-46, 12203 Berlin, Germany*
[2] *Department for Engineering Ceramics, Clausthal University of Technology, Zehntnerstraße 2a, 38678 Clausthal-Zellerfeld, Germany*

Correspondence should be addressed to Jens Günster; jens.guenster@bam.de

Received 27 February 2014; Accepted 28 April 2014; Published 16 June 2014

Academic Editor: Dachamir Hotza

The most successful additive manufacturing (AM) technologies are based on the layer-by-layer deposition of a flowable powder. Although considered as the third industrial revolution, one factor still limiting these processes to become completely autonomous is the often necessary build-up of support structures. Besides the prevention of lateral shifts of the part during the deposition of layers, the support assures quality and stability to the built process. The loose powder itself surrounding the built object, or so-called powder-bed, does not provide this sustenance in most existent technology available. Here we present a simple but effective and economical method for stabilizing the powder-bed, preventing distortions in the geometry with no need for support structures. This effect, achieved by applying an air flow through the powder-bed, is enabling an entirely autonomous generation of parts and is a major contribution to all powder-based additive manufacturing technologies. Moreover, it makes powder-based AM independent of gravitational forces, which will facilitate crafting items in space from a variety of powdery materials.

1. Introduction

Additive manufacturing (AM) describes a class of technologies in which a 3D object is directly generated from a virtual model by adding material in a layer-by-layer approach defined by ASTM F2792-12a (Standard Terminology for Additive Manufacturing Technologies) as the "process of joining materials to make objects from 3D model data, usually layer upon layer, opposed to subtractive manufacturing methodologies, such as traditional machining" [1]. Well-known in the 80th and 90th as Rapid Prototyping, these technologies have been developed to reduce the time to market for new products by shortening the period between design and fabrication [2, 3]. While the need for flexibility in design had first priority at that time, nowadays the physical and functional properties of the generated parts are a major concern, for example, in emerging fields as tissue engineering [4], complex functional, and lightweight structures [5]. In this context even applications in space are currently being tested, where the diversity of tools and spare parts directly relates to the mass to be carried into space [6]. Accordingly, the terminology for this class of technologies shifts gradually from Rapid Prototyping to Additive Manufacturing [7]. The philosophy behind AM is simple: a virtual data set and the choice of material are sufficient to build a part within a ubiquitous manufacturing process. In other words, the requirement of dedicated tooling and the need of adapting the manufacturing process to a certain geometry of the part to be built is obsolete. In the meanwhile, AM offers a broad repertoire of technologies for the manufacture of individual products and even the generation of structures unique to AM is possible. Moreover, additive manufacturing is a step further in the direction towards an autonomous manufacture, as the geometry of a part to be built does not imply a certain machine setup.

The material is typically fed into the process as a powder, paste, or liquid; that is, the material is in a state optimized for the layer deposition process, but not useful for defining a finite geometry. In the manufacturing process itself, the material is used to build up the desired object and it is simultaneously transferred into a state showing its final

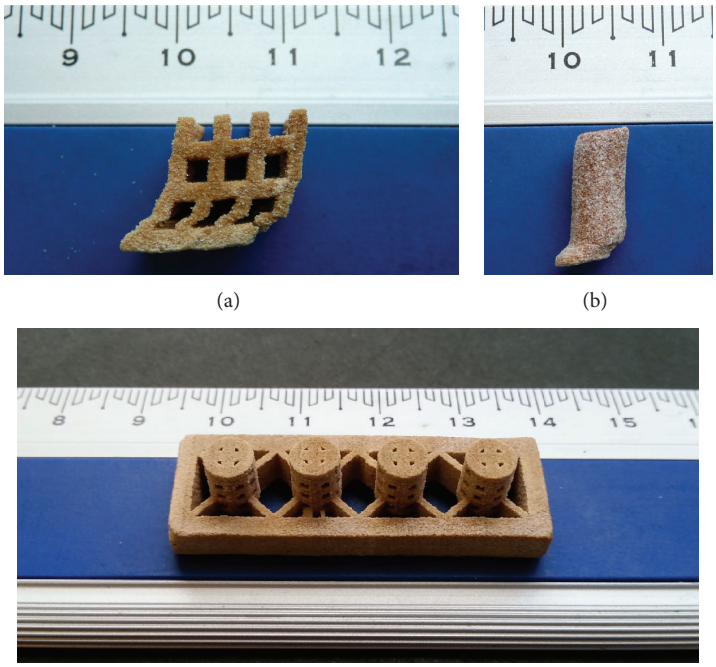

(a) (b)

(c)

Figure 1: ((a), (b)) Ill-defined ceramic parts built without support structure distorted in the 3D printing process. (c) Parts designed with support structure.

physical properties or at least a mechanical strength sufficient to transfer the object built to further processing steps.

In powder-based AM technologies a solid structure is realized by the successive deposition of layers of a flowable powder. Briefly, a layer of powdered material is first spread and subsequently the corresponding layer information is selectively inscribed by, for example, local compaction or gluing; these steps are iteratively replicated until the object is completed. The layer information is defined by the corresponding cross section of a sliced virtual 3D model of the object to be built. At the end, the part is completely embedded in a powder-bed, from which it can be easily extracted and cleaned.

The technology used to inscribe the layer information depends on the specific process considered: two of the most well-known and world-spread processes are the "three-dimensional printing (3DP)" and the "selective laser sintering (SLS)" [8].

The milestone patent "three-dimensional printing techniques" [9] by Sachs et al. was filed in 1989, while Deckard's patent "method and apparatus for producing parts by selective sintering" [10] dates back three years earlier. The former method uses a printing head to selectively spread out droplets of a liquid binder, while the latter employs the energy of a focused laser beam to selectively sinter/melt a powder.

Since the first pioneering applications, many developments have been introduced, greatly extending the use of different materials [11–13], improving the physical properties of the components built, and enhancing the accuracy of the process [14], thus allowing novel applications [15]. Still very important issues remain nowadays, hampering a completely autonomous production of parts and even restricting the freedom of design by means of these technologies. One of the major issues is the stability of the parts during the building process, which implies the need of support structures in most of the AM technologies. Support structures are structures which are built up mainly for the fixation of the desired geometry within the powder-bed. Actually, one of the intrinsic features of the powder-based technologies is the ability of the powder-bed to support the generated parts against gravitation. Despite of this, it is not stable enough to act against forces originating from powder deposition, resulting in a lateral displacement of the object upon subsequent deposition of layers; see Figures 1(a) and 1(b). These forces, which according to most setups are perpendicular to the gravitational force and tangential to the powder-bed's surface, cause the part to shift along the direction of the movement of the deposition unit, which is normally a blade or a roller unit. Therefore, to prevent this effect, support structures are commonly built along with the part, Figure 1(c).

Building up support structures consumes processing time and wastes material. Their removal requires an additional postprocessing, which is again time consuming and involves a dedicated treatment of each individual component. In the case of "selective laser sintering/melting (SLS/SLM)" the tight fixation by such structures causes also internal stresses that can potentially deform the component after its release. Very recently some work has approached this problem from a designer's perspective suggesting an optimization of the parts geometry [16] or of the materials used [17], with the aim of avoiding the use of support structures; other works focused instead on the optimization of the support structures itself

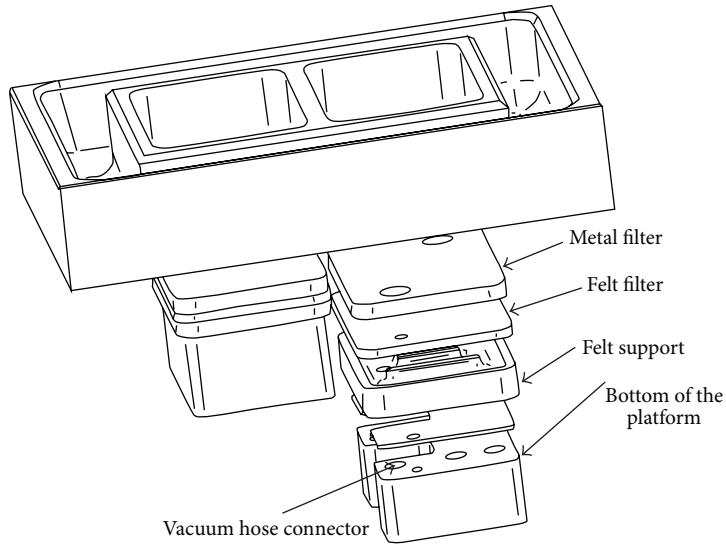

Figure 2: Exploded assembly drawing of the vacuum 3D print setup.

[18, 19]. Both approaches impose restrictions to the freedom in design and clearly have their limitations, as they do not tackle the root cause of the problem.

Obviously there exists a clear need for process improvements that are able to overcome the instability of the powder-bed and, thus, enable an entirely autonomous fabrication process. The application of a gas flow through the powdery material can indeed stabilize the powder-bed to an extent making support structures dispensable. Moreover, it makes the process independent of gravitational forces, facilitating the advantageous application of powder-based AM in space. This work introduces this innovative approach as well as the first results related to the production of parts without need of support structures.

2. Materials and Methods

A commercial 3D printer (RX-1, ExOne, USA) has been modified in order to implement a vacuum setup. This setup is described in detail in the Results and Discussion section (see also Figure 2).

The vacuum pump used is a rotary two-stage pump (PZ, Welch-Ilmvac GmbH, Ilmenau, Germany) with a pumping capacity of 10 m^3/h, while the metal filter was machined from a sheet 5 mm in thickness, purchased from GKN Sinter Metals Filters GmbH, 42477 Radevormwald, Germany. All the other components were designed and CNC machined in house.

Two ceramic powders have been compared in a set of experiments, in order to study the effect of the vacuum setup on the layer-by-layer deposition of the powder-bed in the 3D printer.

A lithium alumino-silicate (LAS) glass frit was provided by Colorobbia S.p.a (Sovigliana Vinci, Firenze, Italy) [20]. More information about the 3D printing of this material can be found in the references [21]. The frit was attrition milled and sieved between 63 μm and 125 μm.

An Al_2O_3 powder (Gilox 63, Almatis GmbH, Ludwigshafen, Germany) presents, according to the producer's specifications, a d_{10} = 2,5 μm; d_{50} = 17 μm; d_{90} = 45 μm.

The density of the powder-bed was determined by weighing the powder after a deposition of 50 layers (each 100 μm thick) in the printer's building platform and dividing the mass by the geometrical volume obtained.

The density measurements were run on triplicates and the values compared by one-tailed Student's t-test. A value of $P < 0.01$ was considered significant, but the exact P values are also reported. All results are reported as mean ± standard deviation.

A proprietary bioceramic was also used to demonstrate the three-dimensional printing of complex-shaped parts using this setup, without the use of support structures. This composition is a fast resorbable calcium alkali orthophosphate ceramic; detailed information about this material can be found elsewhere [22, 23]. The powder used in the experiments was granulated starting from particles (d_{50} = 7 μm) and 5 wt% PVA as binder in a fluidized bed granulator. The granules were sieved between 45 and 90 μm before printing.

3. Results and Discussion

In order to apply an air flow through the powder-bed in a 3D printing process, a commercial 3D printer has been modified according to the proprietary setup in Figure 2: the bottom side of the building platform is connected to a vacuum pump applying vacuum to one side of the powder-bed, resulting in a pressure gradient which creates then an air flow through the powder. A filter made of porous sinter-steel (average pore diameter = 10 μm) acts as building base and prevents the powder from being sucked into the pumping unit. The effect of the applied vacuum can be appreciated in the video provided with the Supplementary Material available online at http://dx.doi.org/10.1155/2014/491581.

Table 1: Bulk density and powder-bed density of powders A and B, with and without the application of the vacuum setup. Comparison of powders A and B freely settled bulk densities according to Hausner method and densities of powder beds composed out of 50 layers, each 100 μm in thickness.

	Powder A: density (g/cm^3) (relative density, %)	Powder B: density (g/cm^3) (relative density, %)
Bulk density		
Free settled	1,02 ± 0,01 (43,4 %)	1,23 ± 0,02 (31,1 %)
Tapped	1,23 ± 0,01 (52,3 %)	1,73 ± 0,01 (43,8 %)
Hausner ratio	1,20 ± 0,02	1,41 ± 0,03
Powder-bed density (50 layers deposited by roller)		
With vacuum	1,16 ± 0,01 (49,4 %)	1,70 ± 0,07 (43,0 %)
Without vacuum	1,09 ± 0,02 (46,4 %)	1,15 ± 0,02 (29,1 %)

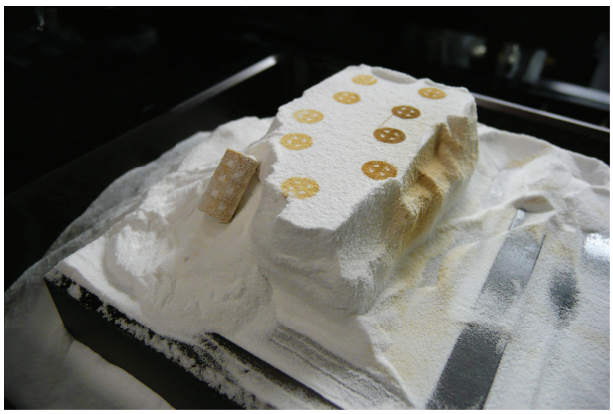

Figure 3: Set of cylinders, revealing a designed ordered porosity, printed applying the described setup, without the use of support structures. Powder used: granulated powder sieved between 45 and 90 μm of a proprietary bioceramic.

The air flow through the powder provides an additional force in direction to the porous building base and first experiments have proven that it is sufficient to stabilize the powder-bed, making support structures dispensable; see also Figure 3.

Figure 3 shows a set of cylinders (diameter = 5 mm, height = 12 mm) revealing a designed ordered porosity that were printed applying the described setup and without the use of support structures. The cylinders show no deformation or distortion. The material used was a granulated powder (sieved between 45 and 90 μm) of a proprietary bioceramic system.

Besides the powder-bed stabilization, the modified setup improves also the powder flow and its compaction during the layer formation process.

From a fundamental physics point of view, the flowing behavior of a powder depends on the interplay between the attractive interparticle force, F_a, and the gravitational force acting on each individual particle, which is directly related to the particle weight, m_g. The ratio between these two forces defines the cohesive granular Bond number, BN = F_a/m_g [24].

Flowability greatly depends on the bond number BN, because if particulates receive a gravitational force much larger than the attractive interparticle force (small BN), they follow gravitation irrespective of an existing interparticle attraction. As a consequence flowable powders pack well [25].

In order to quantify the effect of an air stream through the powder-bed, the layer-by-layer deposition of two different powders was studied: a glass powder (type A), with a rather coarse particle size distribution (63–125 μm) and good flowability and a fine α-Al_2O_3 powder (type B), with an average size of 17 μm and typically poor flowability.

The flowability of the two powders was quantified according to the Hausner Ratio [26]:

$$\mathrm{HR} = \frac{\rho_{\mathrm{Tap}}}{\rho_{\mathrm{Bulk}}} \tag{1}$$

with ρ_{Bulk} being the freely settled bulk density of the powder and ρ_{Tap} being the plateau tap density reached after a certain number of tapping cycles, in g/cm^3. This method was chosen, besides its simplicity, as it directly relates the powder packing density to its flowability. In fact, well flowable powders already reach a high bulk density when they are freely settled, and the increase of density after tapping is lower than for nonflowable powders. Hence, well flowable powders have a lower Hausner ratio than nonflowable powders.

The measured bulk densities and Hausner ratios for powders of type A and type B, reported in Table 1, clearly reveal that the type A powder flows and packs significantly better than type B (higher HR). The determined HR is in accordance with the previous values associated with good and poor flowabilities [26].

In order to evaluate the processability of the two powders, the density of a powder-bed composed of 50 layers each 100 μm thick was measured. For buildup of the layered structure, a commercial 3D printer was employed. The printer uses a counter rotating roller for depositing the individual layers. The obtained densities with and without the application of vacuum are presented in Table 1.

It is noteworthy that, according to Table 1, even without the application of vacuum the rolling deposition has a subtle but significant effect on the powder compaction. The powder-bed for powder A has a higher density compared to the free

settled powder (+6 ± 2%), while the powder-bed for powder B has a lower density than the free settled powder (−6 ± 2%).

This trend is related to the different flowing behavior of the powders, where the flowable powder A can be effectively deposited and compacted by means of the roller, whilst the deposition of the poorly flowable powder B results in a poorly packed powder-bed.

The effect of the application of vacuum on the density of the powder-bed was also evaluated for the two powders. In both cases, there was a significant increase in density when applying vacuum, that is, +48 ± 2% for powder B and +6 ± 2% for powder A. The hypothesis that the density of the powder-bed with the application of vacuum is higher than the density of the powder-bed without the application of vacuum was supported statistically by a one-tailed Student's t-test, yielding a significance level of P value = 1.9×10^{-3} for powder A and P value = 8.5×10^{-5} for powder B.

The increase in density, when vacuum was applied, was much higher for powder B than for powder A. This observation highlights the positive effect of the applied vacuum on the powder compaction especially on fine powders, which typically show a poor flowability.

It is noticeable that the density of the powder-bed for powder B, when vacuum was applied, reaches a value of 1,70 g/cm^3 that corresponds to about 43% of the theoretical density of alpha-Al_2O_3. Such value is particularly remarkable since it is similar to the tapped density of this same powder, which was 1,73 g/cm^3. Furthermore, when vacuum was applied, the relative densities of the powder-beds for powders A (49,4%) and B (43,0%) are comparable. Instead, when vacuum was not applied, the relative densities are considerably different (29,1% and 46,4% theoretical density for powders B and A, resp.).

The effective packing under the influence of a gas flow through the powder-bed can be understood within the framework of a model taking into account the forces active on each individual particle during the layer deposition process. As the vacuum is applied from the bottom side of the powder-bed, see also Figure 2, the sum of all forces averaged over the particles yields a total average force in direction to the building platform and, thus, parallel to gravitation. This observation is intuitively consistent with a macroscopic picture, with the powder simply sucked towards the porous building platform. Within this picture, however, one cannot expect a significant compaction of the powder, as the acting forces are small compared to forces applied in established technologies for compaction of powders. On the other hand, local forces induced by applying an air flow through the powder-bed guide the particles to effectively fill the interstices, as they are acting on the particles already when they are not yet in direct contact with the neighboring particles, that is, in the flowing state during the layer deposition. This effect is existing irrespective of the action of gravitational forces, which, in turn, facilitates powder-based AM under zero gravity.

The effect of external forces on the packing behavior of calcined alumina with different particle size distributions is already known in the literature. Mechanically dried filter-cake of deflocculated fine-grained alumina presents higher packing fractions if the powder has larger geometric standard deviation. The packing density depends significantly on the form of the size distribution and also on the range of the particle size [27]. Different models (e.g., [28] or [29]) can be used to predict these effects on the degree of densification of a powder compact without and with application of external forces, for example, tapping cycles. Ideally, if the particle size decreases, the proportion of fines must increase in order to fill the interstices between coarser particles, increasing though the packing fraction [27]. This effect is accentuated during the stabilization with vacuum, since it helps the finer particles to migrate between the interstices of the coarser ones. It has been observed that powders with a wide size distribution in the range of 20–50 μm, and large amounts of fines, have limited the effect of the air flow to only few millimeters height, because the powder-bed becomes quickly clogged by the finer particles filling the voids between the coarser.

However, it should be noted that the stabilization effect of vacuum is active for powder-beds up to 100 mm, in the case of powders with a coarse grain size (>50 μm, such as powder type A) and small amounts of fines. Powders with smaller grain sizes should present low proportion of fines or a tighter particle size distribution.

Further studies and simulations will be devoted to the understanding of the interplay between air flow and the formation of the powder-bed, such as the formation of preferential paths within the powder.

4. Conclusions

The application of an air flow through the powder has been demonstrated as an effective method for stabilizing the powder-bed during the layer-by-layer deposition. A proprietary setup has been applied to a commercial 3D printer, allowing the manufacturing of three-dimensional ceramic parts without the use of support structures. Moreover, it was found that the application of this setup can increase the density of the powder-bed, especially in the case of the deposition of nonflowable powders.

This setup could be easily adapted to other additive manufacturing technologies (e.g., SLS) and to other materials (e.g., metals), allowing an improved control over the geometry of the parts without the need of support structures, thus enabling a completely autonomous powder-based additive manufacturing process.

Conflict of Interests

The authors declare that there is no conflict of interests regarding the publication of this paper.

References

[1] ASTM Standard F2792, *Standard Terminology for Additive Manufacturing Technologies*, ASTM International, West Conshohocken, Pa, USA, 2012.

[2] E. Sachs, M. Cima, P. Williams, D. Brancazio, and J. Cornie, "Three dimensional printing. Rapid Tooling and prototypes directly from a CAD model," *Journal of Engineering for Industry*, vol. 114, no. 4, pp. 481–488, 1992.

[3] D. T. Pham and R. S. Gault, "A comparison of rapid prototyping technologies," *International Journal of Machine Tools and Manufacture*, vol. 38, no. 10-11, pp. 1257–1287, 1998.

[4] S. J. Hollister, "Porous scaffold design for tissue engineering," *Nature Materials*, vol. 4, no. 7, pp. 518–524, 2005.

[5] D. W. Rosen, "Computer-aided design for additive manufacturing of cellular structures," *Computer-Aided Design & Applications*, vol. 4, no. 1–6, pp. 585–594, 2007.

[6] M. Snyder, J. Dunn, and E. Gonzalez, "The effects of microgravity on extrusion based additive manufacturing," in *Proceedings of the AIAA SPACE Conference and Exposition*, September 2013.

[7] D. Bak, "Rapid prototyping or rapid production? 3D printing processes move industry towards the latter," *Assembly Automation*, vol. 23, no. 4, pp. 340–345, 2003.

[8] D. L. Bourell, H. L. Marcus, J. W. Barlow, and J. J. Beaman, "Selective laser sintering of metals and ceramics," *International Journal of Powder Metallurgy*, vol. 28, no. 4, pp. 369–381, 1992.

[9] E. M. Sachs, J. S. Haggerty, M. J. Cima, and P. A. Williams, "Inventors, Massaschussets Institute of Technology, Assignee. Three-dimensional printing techniques," US Patent no. 5,204,055, April 1993.

[10] C. R. Deckard, "Inventor, Board of Regents, The University of Texas System, Assignee. Method and apparatus for producing parts by selective sintering," US Patent no. 4,863,538, September 1989.

[11] S. Kumar and J.-P. Kruth, "Composites by rapid prototyping technology," *Materials and Design*, vol. 31, no. 2, pp. 850–856, 2010.

[12] P. Calvert, "Materials science: printing cells," *Science*, vol. 318, no. 5848, pp. 208–209, 2007.

[13] T. F. Wegrzyn, M. Golding, and R. H. Archer, "Food Layered Manufacture: a new process for constructing solid foods," *Trends in Food Science & Technology*, vol. 27, no. 2, pp. 66–72, 2012.

[14] I. Yadroitsev, I. Shishkovsky, P. Bertrand, and I. Smurov, "Manufacturing of fine-structured 3D porous filter elements by selective laser melting," *Applied Surface Science*, vol. 255, no. 10, pp. 5523–5527, 2009.

[15] N. Jones, "Science in three dimensions: the print revolution," *Nature*, vol. 486, no. 7405, pp. 22–23, 2012.

[16] C. Yan, L. Hao, A. Hussein, and D. Raymont, "Evaluations of cellular lattice structures manufactured using selective laser melting," *International Journal of Machine Tools and Manufacture*, vol. 62, pp. 32–38, 2012.

[17] K. Mumtaz, P. Vora, and N. Hopkinson, "A method to eliminate anchors/supports from directly laser melted metal powder bed processes," in *Proceedings of the 22nd International Solid Freeform Fabrication Symposium*, Austin, Tex, USA, 2011.

[18] A. Hussein, L. Hao, C. Yan, R. Everson, and P. Young, "Advanced lattice support structures for metal additive manufacturing," *Journal of Materials Processing Technology*, vol. 213, no. 7, pp. 1019–1026, 2013.

[19] J. Jhabvala, E. Boillat, C. André, and R. Glardon, "An innovative method to build support structures with a pulsed laser in the selective laser melting process," *International Journal of Advanced Manufacturing Technology*, vol. 59, no. 1–4, pp. 137–142, 2012.

[20] G. Baldi, G. Borelli, A. Antonini, and M. Bitossi, "Inventors, Colorobbia Italia S.P.a., Assignee. Process for the preparation of ceramic glass material in the form of sheets, sheets thus obtained and use thereof," Patent application US, 2010/0069218 A1, March 2010.

[21] A. Zocca, C. M. Gomes, E. Bernardo, R. Müller, J. Günster, and P. Colombo, "LAS glass-ceramic scaffolds by three-dimensional printing," *Journal of the European Ceramic Society*, vol. 33, no. 9, pp. 1525–1533, 2013.

[22] G. Berger, R. Gildenhaar, and U. Ploska, "Rapid resorbable, glassy crystalline materials on the basis of calcium alkali orthophosphates," *Biomaterials*, vol. 16, no. 16, pp. 1241–1248, 1995.

[23] R. Gildenhaar, C. Knabe, C. Gomes, U. Linow, A. Houshmand, and G. Berger, "Calcium alkaline phosphate scaffolds for bone regeneration 3Dfabricated by additive manufacturing," *Key Engineering Materials*, vol. 493-494, pp. 849–854, 2012.

[24] S. T. Nase, W. L. Vargas, A. A. Abatan, and J. J. McCarthy, "Discrete characterization tools for cohesive granular material," *Powder Technology*, vol. 116, no. 2-3, pp. 214–223, 2001.

[25] A. Castellanos, "The relationship between attractive interparticle forces and bulk behaviour in dry and uncharged fine powders," *Advances in Physics*, vol. 54, no. 4, pp. 263–276, 2005.

[26] H. H. Hausner, "Powder characteristics and their effect on powder processing," *Powder Technology*, vol. 30, no. 1, pp. 3–8, 1981.

[27] J. S. Reed, *Principles of Ceramics Processing*, Wiley, New York, NY, USA, 1995.

[28] A. H. M. Andreasen, "Ueber die Beziehung zwischen Kornabstufung und Zwischenraum in Produkten aus losen Körnern (mit einigen Experimenten)," *Kolloid-Zeitschrift*, vol. 50, no. 3, pp. 217–228, 1930.

[29] J. E. Funk and D. R. Dinger, *Predictive Process Control of Crowded Particulate Suspensions Applied to Ceramic Manufacturing*, Kluwer Academic Publishers, Norwell, Mass, USA, 1994.

Hindawi Publishing Corporation
Advances in Mechanical Engineering
Volume 2014, Article ID 141346, 12 pages
http://dx.doi.org/10.1155/2014/141346

Research Article

Novel Prospects and Possibilities in Additive Manufacturing of Ceramics by means of Direct Inkjet Printing

Anja Mareike Wätjen, Philipp Gingter, Michael Kramer, and Rainer Telle

Department of Ceramics and Refractory Materials, Institute of Mineral Engineering, RWTH Aachen University, Mauerstraße 5, 52064 Aachen, Germany

Correspondence should be addressed to Anja Mareike Wätjen; waetjen@ghi.rwth-aachen.de

Received 3 March 2014; Accepted 22 April 2014; Published 13 May 2014

Academic Editor: Jens Günster

Direct inkjet printing is a versatile additive manufacturing technology to produce complex three-dimensional components from ceramic suspensions. By successive printing of cross-sections, the sample is built up layer by layer. The aim of this paper is to show the different possibilities of direct inkjet printing of ceramic suspensions, like printing of oxide (3Y-TZP, Al_2O_3, and ZTA) or nonoxide (Si_3N_4, $MoSi_2$) ceramics, featuring microstructures, laminates, three-dimensional specimens, and dispersion ceramics. A modified thermal inkjet printer was used and the ink replaced by aqueous ceramic suspensions of high solids content. The suspensions were processed in an attrition mill or agitator bead mill to reduce the grain size <1 μm to avoid clogging of printhead nozzles. Further significant parameters are rheological properties (viscosity and surface tension) and solids content which were adjusted to the requirements of the printheads. The printed and sintered samples were analysed by SEM. Mechanical properties of 3Y-TZP samples were examined as well by use of the ball-on-three-balls test. The biaxial flexural strength of 3Y-TZP specimens was up to 1393 MPa with a Weibull modulus of 10.4 for small specimens ($3 \times 4 \times 0.3\ mm^3$).

1. Introduction

Additive manufacturing (also known as freeform fabrication or generative manufacturing) comprises a group of technologies that feature construction of objects from 3D model data by assembly of materials, typically layer by layer [1]. By these means complex three-dimensional ceramic components can be produced directly without the need for moulds or part-specific tools. Depending on the technology the shape of the sample is realized by consolidating a powder bed either by addition of a binder (three-dimensional printing [2–4]), or by selective heat treatment (e.g., selective laser sintering or selective laser melting [5–8]), or by selective curing of a photosensitive resin containing ceramic particles (stereolithography [9–12]), or by direct deposition of material (e.g., fused deposition modelling [13, 14], 3D printing in filamentary form [15, 16], aerosol jet printing [17], or direct inkjet printing [15]).

Following ASTM F2792-12a, direct inkjet printing (DIP) is considered a form of 3D printing as the construction of a specimen is realized by material deposition through a nozzle of a printhead [1]. In contrast to classical 3D printing where a bonding agent is deposited in a powder bed (binder jetting), the emitted droplets in DIP contain the building material which is selectively deposited on a substrate (material jetting) [1]. The latter enables additive manufacturing of layers and (micro) structures as well as complex three-dimensional geometries from ceramic suspensions with high solids content. The selective deposition of single particle-loaded droplets permits high precision whose level of detail even allows accurate placement of different materials next to each other. Furthermore, the resulting structures printed by DIP feature high density and mechanical properties similar to conventionally fabricated ceramic components. Due to direct deposition of materials from suspensions, it is possible to produce multimaterial parts or even cavities which are not

feasible in such form through other fabrication technologies. Additionally, the drop-wise use of varying materials makes it possible to specifically introduce internal stresses even in complex geometries.

In drop-on-demand inkjet printing a distinction is made between piezoelectric and thermal printheads. While both employ a pressure pulse to form drops, the method varies: the former ensures displacement of ink within the printhead chamber and drop ejection through deformation of a piezoelectric crystal thus mechanically creating a pressure pulse, while thermal printheads (also called bubble-jet) force ink through the nozzle by generating a bubble caused in the ink by a rapidly heated resistor [18, 19]. Thermal printheads were used for the studies shown in this paper.

The ceramic suspension used as ink in DIP consists of a suspension comprised of ceramic particles, dispersant, and functional additives, that is, surfactant, binder, and humectant. Depending on the specific requirements of the utilized printhead these ensure the necessary adjustment of rheological suspension properties like viscosity and surface tension. A further prerequisite for the ink development results from the nozzle diameter. As picolitre sized droplets are ejected through the fine nozzles of the printhead, the particle size needs to be controlled to prevent clogging of nozzles. Lejeune et al. [20] and Magdassi [18] have recommended the ratio of nozzle diameter to particle size to be larger than 50 or 100, respectively. Furthermore, for efficient and defect-free build-up on the one side and stabilization of dispersed particles against agglomeration, flocculation, and subsequent sedimentation on the other side high solids content (>20 vol%) is recommended [21].

Oxidic high-performance ceramics, in particular alumina (Al_2O_3) and yttrium stabilized zirconia (3Y-TZP), are distinguished by high flexural strength, wear resistance, and fracture toughness as well as confirmed biocompatibility. Based on these characteristics they have been used for many years in the field of endoprosthetics, for example, as hip joint ball or as matrix material for dental prosthesis like crowns and frameworks [22]. In recent years, zirconia has even been used for dental implants [23, 24]. The steadily rising demand for ceramic materials is due to aesthetic aspects and frequently occurring biological reactions, inflicted by application of metallic implants. Metallic hip joint parts (ball and acetabulum made of titan- or cobalt-chrome-alloys) may cause friction at the metal/metal pairing, generating undesirable biological reactions, for example, local and systemic metal intoxications.

Alumina and zirconia are bioinert; that is, after the implantation, no chemical or biological interactions between implant and surrounding tissue take place. Based on clinical studies it becomes more and more apparent that loosening of zirconia dental implants consistently takes place, like it has been observed in the early 1990s on monolithic alumina hip joint acetabula [25, 26]. The occurring loosening can be explained by the inert behaviour of the ceramic surface and the insufficient stimulation of the bordering bone tissue [25, 26]. For an enhancement of the cell adhesion and differentiation strategies for bioactivation have to be located. As the microstructure of a material significantly influences the biologic reaction at the interface [27–29], it is reasonable to change the microstructure of a surface in such a way that the cells could respond favourably with a change into osteoblasts (bone-building cells) to enhance the bone engraftment. Since no literature has been found to confirm response of cells to surface modification alone of alumina or zirconia further research has to be done to verify this thesis. With a high resolution printhead potential microstructures for this field of research could be produced by DIP.

Functionally graded materials (FGMs) are combinations of two or more different materials with a continuously varying distribution across the geometry of a part. In contrast to conventional composites FGMs are characterized by very smooth transitions between different materials, which substantially improve material properties or open up entirely new applications [32]. However, conventional forming technologies as slip casting or pressing are limited concerning their possibility to define and control such gradient material transitions [33]. In contrast DIP permits precise, accurate placement of single picolitre sized droplets and is thus eminently suitable to realize complex shaped geometries with functional material gradation.

The aim of this paper is to show the different possibilities of direct inkjet printing of ceramic suspensions, like printing of oxide or nonoxide ceramics, featuring microstructures, laminates, three-dimensional specimens, and dispersion ceramics. Ceramic suspensions are characterized regarding their particle size distribution, rheological properties (viscosity and dynamic surface tension), and solids content. The printed and sintered samples are analysed by SEM.

This paper provides an overview on work concerning direct inkjet printing originated at the Institute of Mineral Engineering of RWTH Aachen University. This concerns recapitulation of previously published work (on Si_3N_4, $MoSi_2$, complex shaped structures of zirconia, and three-dimensional zirconia specimens for ball-on-three-balls test) as well as innovative novel experimental work (regarding microstructures, laminates, and dispersion ceramics).

2. Materials and Methods

A modified office type drop-on-demand thermal inkjet printer (HP DeskJet 930c, Hewlett Packard, Palo Alto, USA) was used for all samples unless stated otherwise. The modifications allowed layerwise build-up of parts from cross-sections. The printed layers were subsequently dried and the substrate lowered owing to the installation of a z-axis thus ensuring a consistent distance between the printhead and the substrate or the uppermost layer. Figure 1 shows a schematic of the printing system. This printer uses thermal printheads, of which only the black ink cartridge (HP51645A) was used to eject the ceramic suspensions. After draining and rinsing the cartridges, they were completely dried to prevent dilution with residual water. Subsequently they were refilled with a minimum of 25 mL of ceramic suspension and the remaining air was evacuated. The printhead provides 600 dpi spatial resolution by use of 304 nozzles with ~30 μm nozzle diameter each.

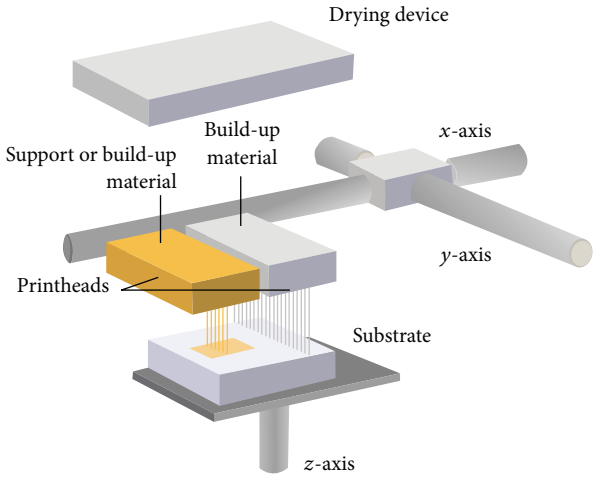

Figure 1: Schematic of the printing system (after [30]).

2.1. Materials Printed

2.1.1. Oxide Ceramics. Zirconia and alumina inks were prepared for DIP. The aqueous zirconia starting suspension had 40 vol% of solids content of 3Y-TZP (TZ-3YS-E, Tosoh, Tokyo, Japan) and 4 vol% of dispersant (Dolapix CE64, Zschimmer & Schwarz GmbH & Co. KG, Lahnstein, Germany). To prepare the suspension the submicrometer-sized 3Y-TZP powder with a specific surface area of $(7 \pm 2)\ m^2/g$, a mean particle size of 0.6 μm and a sintered density of 6.05 g/cm^3 [39] were attrition-milled (30 min, 1200 rpm) in aqueous media using 1 mm zirconia beads [31]. For the alumina starting suspension an alumina powder (CT 3000 LS SG, Almatis, Ludwigshafen, Germany) with a specific surface area of 7.8 m^2/g, a mean particle size of 0.5 μm, and a sintered density of 3.95 g/cm^3 was dispersed in distilled water with dispersant Dolapix CE64 and milled using a laboratory agitator bead mill (MicroCer, Netzsch-Feinmahltechnik GmbH, Selb, Germany) with zirconia grinding beads (diameter 0.2-0.3 mm). These basic zirconia and alumina suspensions were diluted in order to achieve ceramic inks with final solids content of 27 vol% [21, 34, 36] and 31.1 vol%, respectively (Table 1). Further organic additives like humectants (Glycerol 85%, Hedinger, Stuttgart, Germany) and drying accelerators (Ethanol, Merck KGaA, Darmstadt, Germany) were added to increase the compatibility with the chosen thermal printhead [21, 30, 35, 39].

In order to print complex shaped structures of zirconia with enclosures and/or undercuts a supportive carbon based suspension was developed. This supportive ink was an aqueous dispersion of submicrometer sized, thermal type carbon black particles (Arosperse 15, Evonik Chemicals, Essen, Germany) with an average particle size of 0.28 μm. An alkali free carboxylic acid ester based dispersant was used (Dolapix ET85, Zschimmer & Schwarz GmbH & Co. KG, Lahnstein, Germany). The suspension was ball-milled for 36 h using Al_2O_3 beads of 5 mm diameter prior to jetting [36].

The 3Y-TZP and alumina ink as well as a pigment based reference ink (HP45) were characterized at 20°C in terms of particle size distribution, viscosity, and surface tension. The density of the 3Y-TZP ink was determined using a pycnometer (25 mL, Brand, Wertheim, Germany). The particle size distribution was measured according to the full Mie theory using the low-angle laser light scattering method (Mastersizer 2000, Malvern Instruments, Malvern, UK). Furthermore, the viscosity was determined at a shear rate of 1000/s using a rotational rheometer (Viscolab LC10, Physica, Germany) with a double gap concentric measuring system. The surface tension was analyzed according to the bubble pressure method (Proline t15, SITA Messtechnik, Dresden, Germany) for a bubble lifetime of 0.5 s [21, 34].

Table 1: Zirconia (3Y-TZP) and alumina ink composition [30].

Material	Content (vol%) zirconia	Content (vol%) alumina
3Y-TZP powder	27.0	—
Al_2O_3 powder	—	31.1
Distilled water	39.0	50.3
Organic additives	33.0	18.6
Inorganic binder	1.0	0

Printing of aqueous oxide ceramic suspensions was carried out by layerwise deposition using a modified drop-on-demand inkjet printer as described above. Printed structures contained single drops for printability evaluation [21], channel structures [30, 35], bridge frameworks [36], dental crowns [39], and molar teeth [40]. Furthermore test specimens with defined dimensions were produced to measure mechanical properties like characteristic strength, Weibull modulus, and fracture toughness.

Before sintering the printed components were first dried at 80°C for 6–12 h. The organic residue was pyrolized at 550°C for 3 h and the parts were manually removed from the substrate. Subsequently they were sintered in a powder bed at 1450°C for 2.5 h. [30, 34, 39, 41].

To determine the density of the sintered samples the principle of Archimedes with distilled water as immersion liquid was used, while green density was calculated by measuring volume and weight. A ball-on-three-balls test was carried out using a universal testing machine (Zwick Z010, Zwick/Roell, Ulm, Germany) with a jig especially designed at ISFK (Leoben, Austria) on two sets of rectangular shaped specimens ($3 \times 4 \times 0.3\ mm^3$ and $2 \times 2 \times 0.3\ mm^3$) [42–44]. Fracture toughness was determined for $3 \times 6 \times 30\ mm^3$ specimens by a four-point-bending unit (type 1186, Instron, Darmstadt, Germany) [30]. The characteristic strength σ_0 and Weibull modulus m were calculated with a specific software (PEST/CARES, NASA, Cleveland, Ohio, USA) [45] using the maximum-likelihood method [46]. The microstructure of sintered parts was characterized by SEM (Leo 440i, Leo Elektronenmikroskopie GmbH, Oberkochen, Germany) and TEM (Philips CM30, Royal Philips N.V., Eindhoven, Netherlands).

2.1.2. Nonoxide Ceramics. As examples of nonoxide ceramics silicon nitride (Si_3N_4) and molybdenum disilicide ($MoSi_2$) were used to realize structural and functional parts by DIP. The basis of the aqueous suspensions was α-Si_3N_4 powder (SN-E10, UBE Industries, Tokyo, Japan) with a specific surface area of 10 m^2/g and a mean particle size of 0.5 μm and $MoSi_2$-powder (Grade C, H. C. Starck GmbH, Goslar, Germany) with a specific surface area of 1.5 m^2/g and a mean particle size of 2.8 μm. To allow liquid phase sintering of Si_3N_4, yttrium aluminum garnet (YAG, Treibacher Industrie AG, Althofen, Austria) was used as sintering additive. Si_3N_4 and $MoSi_2$ were separately dispersed in aqueous media and ball-milled, using a laboratory agitator bead mill with ZrO_2 grinding beads as mentioned above. This was necessary to meet the requirements of the printheads regarding particle size as described above. Solids content of the Si_3N_4- and $MoSi_2$-suspensions was 30.2 and 26.7 vol%, respectively. After ball milling, the suspensions were stabilized and adjusted to the required physical and rheological ink properties of the printhead. The detailed ink composition and procedure were described elsewhere [37, 38].

Layerwise printing of aqueous nonoxide ceramic suspensions was carried out using the modified drop-on-demand inkjet printer described above. Printed structures contained pillar arrays and gearwheels of Si_3N_4 as well as $MoSi_2$ heating elements. Furthermore, bulk parts with defined dimensions were realized to evaluate mechanical properties (characteristic strength, Weibull modulus, fracture toughness, and hardness).

After printing the green bodies were submitted to a debinding process. Si_3N_4 specimens were treated in air for 2 hours at 600°C while $MoSi_2$ was debinded for 2 hours at 600°C in argon atmosphere to prevent oxidation. Si_3N_4 was pressureless sintered in a resistance heated furnace (HPW 250, FCT, Rauenstein, Germany) for 2 hours at 1780°C under flowing nitrogen. To avoid decomposition of the Si_3N_4 parts they were sintered in a powder bed consisting of Si_3N_4, sintering additives, and boron nitride. $MoSi_2$ samples were fired for 15 minutes at 1700°C under flowing argon.

The microstructure of green and sintered parts was characterized by SEM. The density of the sintered samples was determined using the principle of Archimedes with distilled water as immersion liquid, while green density was calculated by determining volume and weight. Hardness was determined by use of Vickers indentation with an indenter load of 19.8 N and a dwelling time of 10 s. Fracture toughness (KIc) was calculated from median cracks emerging from the Vickers imprint according to the ICL method [47]. The strength analysis was performed on disc-shaped specimens (thickness (3 ± 0.05) mm, diameter (12 ± 0.1) mm) using the ball-on-three-balls (B3B) test [42–44]. The B3B test was performed with a universal testing machine (type 1186, Instron, Darmstadt, Germany). The characteristic strength σ_0 and Weibull modulus m were calculated with a specific software (PEST/CARES, NASA, Cleveland, Ohio, USA) [45] using the maximum-likelihood method [46].

2.2. Printing Strategies

2.2.1. 2D-3D Patterns. As DIP uses a high resolution printhead (600 dpi), it is possible to produce potential microstructures for research in the field of bioactivation of surfaces. To start with, microstructures, either with pillar arrays or with hollows, were chosen to determine the best environmental conditions for cell growth. Based on a cell size of about 100 μm, distances between primary structure elements (pillar/pillar or hollow/hollow) from 100 μm to 300 μm were printed with the alumina suspension to observe cell growth.

2.2.2. Laminates of ZrO_2 and ZTA. A suspension of zirconia toughened alumina was prepared by grinding aqueous suspensions of alumina (CT3000 LS SG, Almatis, Ludwigshafen, Germany) and zirconia (TZ-3YS-E, Tosoh, Tokyo, Japan) individually in an agitator bead mill as described above at 2500 rpm for 7 hours. The resulting suspensions were mixed to achieve a ratio of $Al_2O_3 : ZrO_2$ of 60 : 40 and further additives like dispersant (Dolapix CE64, Zschimmer & Schwarz GmbH & Co. KG, Lahnstein, Germany), humectant (Glycerol 85%, Hedinger, Stuttgart, Germany), and drying accelerator (Ethanol, Merck KGaA, Darmstadt, Germany) were added to ensure compatibility of the rheological properties with the printhead, resulting in a final solids content of 27 vol%.

Small specimens of 3 × 4 mm^2 consisting of successively printed layers of ZTA and 3Y-TZP (each consisting of 10 layers) were alternately printed with the abovementioned modified printer using different printheads for each suspension. After drying the samples were sintered at 1550°C for 2 hours. The microstructure of the samples was analyzed using SEM.

2.2.3. Functionally Graded Materials. Commercial alumina suspension (BA15PSH, Baikowski Group, Annecy, France) and zirconia powder (TZ3YS-E, Tosoh Corporation, Yamaguchi, Japan) were conditioned to aqueous inks by high energy milling and adding different additives, such as ethanol, ethylene glycol, binder, and an antifoaming agent. Solids content was adjusted to 21 vol% for both ceramic inks. Composition and detailed preparation procedure have been reported elsewhere [21]. Three-dimensional structures were built up using two different printheads for alumina and zirconia. Subsequently, single drops of the materials were precisely combined on the substrate. The printing system was based on a conventional powder bed printer (Z510, Z-Corporation, Burlington, USA), which permits multicolour printing. The printhead for yellow colour was used for alumina ink, while zirconia ink was printed by the cyan colour printhead. Rectangular parts, based on coloured model files, were printed to demonstrate the potential of DIP for the fabrication of FGM parts. However, the printer, which was used in this study, is limited to the production of colour gradients in two directions, as no file format with true volumetric colouring was available. Optical documentation and analysis of structures was carried out by photography and scanning electron microscopy.

Table 2: The properties of the 3Y-TZP, Al_2O_3, and HP45 inks at 20°C [31].

	3Y-TZP	Al_2O_3	HP45
Calculated density, ρ (g/cm^3)	2.35 ± 0.05	1.93 ± 0.05	1.06 ± 0.05
Particle size, d_{50} (nm)	280 ± 4	328 ± 5	65 ± 1
Particle size, d_{90} (nm)	890 ± 14	523 ± 8	81 ± 1
Viscosity, η (mPas)	15.4 ± 0.1	5.8 ± 0.1	2.9 ± 0.1
Surface tension, σ (mN/m)	42.0 ± 0.3	66.6 ± 0.3	53.0 ± 0.3

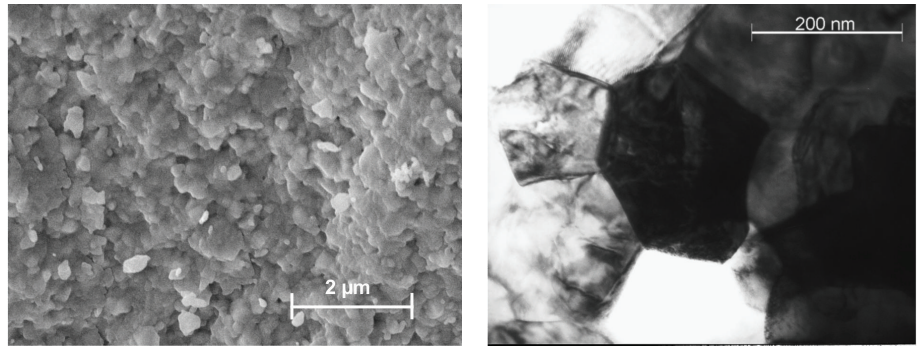

(a) (b)

Figure 2: SEM micrograph showing the fracture surface of a printed and sintered 3Y-TZP part (a); TEM micrograph of a microstructure of printed and sintered 3Y-TZP (b) [30].

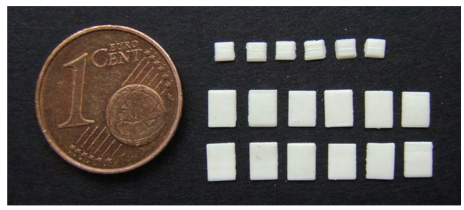

Figure 3: Printed and sintered 3Y-TZP samples with dimensions 2 × 2 × 0.3 mm^3 (above) and 3 × 4 × 0.3 mm^3 (below) [34].

3. Results and Discussion

The properties of the 3Y-TZP and alumina ink as well as a pigment based reference ink (HP45) in terms of density, particle size distribution, viscosity, and surface tension are depicted in Table 2. Results of laser scattering showed a medium particle size of about 280 nm and 328 nm, as well as a characteristic size of 890 nm and 523 nm for the d_{90} value for zirconia and alumina, respectively. However, the agglomerate size fits the requirements of the printhead and was in the range of a printable suspension for thermal inkjet printing processes [18, 30]. Although the viscosities of the ceramic inks were higher than the viscosity of the reference ink, they were still within the printable region of thermal printheads that are capable of ejecting fluids with a viscosity up to 30 mPas [18]. In terms of surface tension both suspensions were within the region of the reference ink (42.0 mN/m and 66 mN/m versus 53.0 mN/m), and both their densities were higher by factor ~2.

For zirconia, after heat treatment, precise, dense three-dimensional structures in mm scale were obtained. Up to 97% of the theoretical density was achieved. The linear shrinkage was isotropic and of about 20%. No process-dependent defects could be observed as shown in Figure 2(a). The SEM micrograph displayed a fine and homogeneous microstructure. Grain size was below 1 μm and a nanosized porosity was present [30, 31, 36, 39]. A TEM micrograph in Figure 2(b) shows the grain size and shape of a printed structure after sintering [35].

The investigations of the mechanical properties on a small number of printed 3Y-TZP specimens (Figure 3) yielded a flexural strength of up to 1366 MPa with a Weibull modulus of 5.3 for the smaller specimens (2 × 2 × 0.3 mm^3) and 1393 MPa with a Weibull modulus of 10.4 for the 3 × 4 × 0.3 mm^3, respectively [34].

Furthermore, the fracture toughness was 8.9 MPam$^{0.5}$. In terms of Weibull modulus (m), the inkjet printed 2 × 2 × 0.3 mm^3 specimens showed an uncommonly low m in contrast to that of the 3 × 4 × 0.3 mm^3 specimens. This suggested a wider critical flaw size distribution in this set. In order to clarify the origin of failure in all these sets, a fractographic analysis was performed on some of the broken specimens. Due to the analysis it was thus supposed that in absence of other microstructural defects or processing damage, even the smallest inaccuracy on the surface subjected to tensile stress during B3B-testing is critical [34]. These values were obtained without any optimization of the microstructure [30].

Complex shaped structures with high accuracy, for example, a "box with two movable matches" (Figure 4(a)), a channel structure (Figure 4(b)), or a bridge framework (Figure 5)

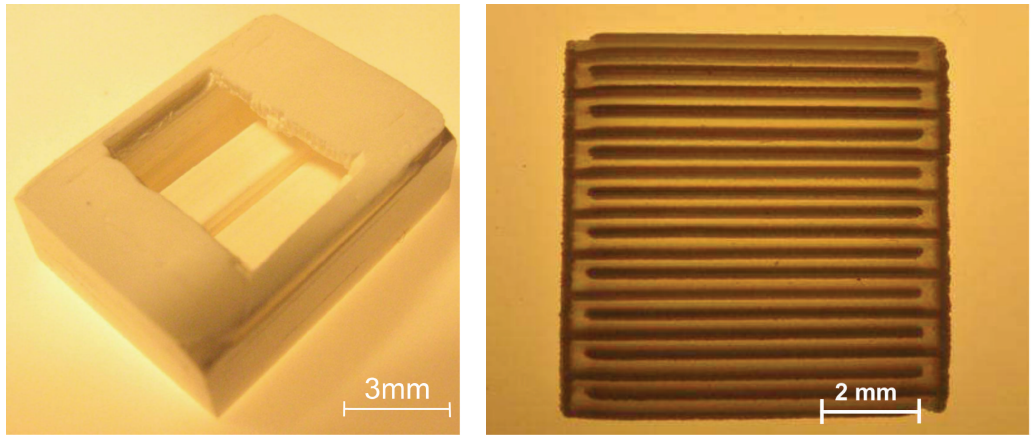

(a) (b)

Figure 4: A sintered "box with two movable matches" made by 3Y-TZP (a) [35]; printed and sintered 3Y-TZP channel structure (b) [30, 35].

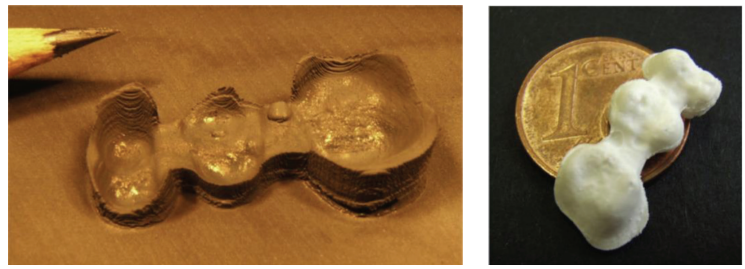

(a) (b)

Figure 5: Produced by DIP: the supportive base made of carbon black (a) and the sintered 3Y-TZP bridge framework (b) [36].

[36], were produced by DIP. On the one hand, the channel structure with a wall thickness of 200 μm demonstrates the accurateness which this process is capable of [35]. On the other hand, when the printing unit is equipped with a single printhead, complex shaped structures can be constructed with overhangs, undercuts, and enclosures. Since only one cartridge can be used at once, here it was first filled with the supportive ink and the base was completely built up. Afterwards it was replaced by another cartridge filled with the ceramic ink and the framework was printed onto the base. Therefore the optimum distance between the printhead and substrate surface could not be maintained in case of printing the ceramic ink. The larger the distance is, the longer the flight of droplets lasts. This misleads the position of the drop impact on the substrate and therefore reduces the accuracy of the printed structure. However, in this study, inaccuracies, due to the distance between the printhead and the substrate, were compensated, because of the fact that the supportive carbon framework acted as a mold [36].

In case of the "matchbox" (Figure 4(a)) it was possible to subdivide the printing procedure in more than two steps. Because of that it was also possible to establish the undercut and the enclosure of the matches [35]. As both inks were aqueous, mixing with each other is a crucial point of interest when a system with multiple printheads is used. However, in this specific case the base was deposited and completely dried before the ceramic ink was deposited onto it. As a result no mixing of both phases was observed [36].

3.1. Nonoxide Ceramics. Developed aqueous inks of Si_3N_4 and $MoSi_2$ were printable after the adjustment of physical properties and the additive system. Clogging of nozzles or feed channels of the printheads was only occasionally observed, demonstrating effectiveness of high-energy milling and particle stabilization. Multilayer samples were successfully printed, resulting in a green density of (1.77 ± 0.21) g/cm^3 for Si_3N_4, which corresponds to more than 50% of the theoretical density. $MoSi_2$ samples possessed a green density of (2.94 ± 0.31) g/cm^3, which is marginally below 50% of the theoretical density. Sintered Si_3N_4 samples exhibited a density of (3.17 ± 0.05) g/cm^3, which corresponds to a relative density of 96.4% [37]. SEM analysis (Figure 6(a)) illustrates the homogeneous microstructure which confirms the density measurements. For $MoSi_2$ a relative density of only 87.9% ((5.55 ± 0.15) g/cm^3) could be obtained. Nevertheless, the microstructure contains low porosity as shown in Figure 6(b). However, amorphous SiO_2 can be identified at triple points due to the poor wetting behavior towards the $MoSi_2$ matrix. SiO_2 was formed because $MoSi_2$ was oxidated during the printing process especially at high drying temperatures.

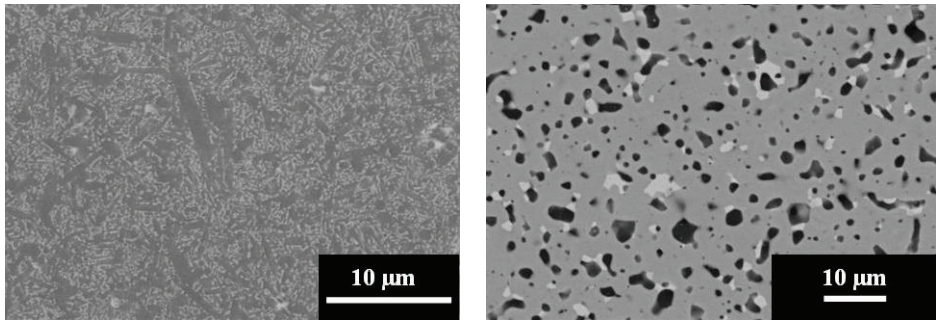

(a) (b)

Figure 6: SEM micrograph of plasma etched Si_3N_4 microstructure (a). SEM micrograph of polished $MoSi_2$ microstructure (b).

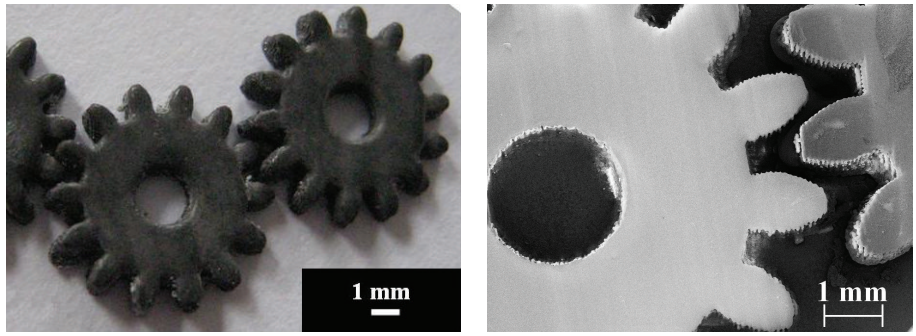

(a) (b)

Figure 7: Printed Si_3N_4 gearwheels (green) (a). SEM picture of sintered Si_3N_4 gearwheels (b) [37].

This is an explanation for the reduced density compared to monophase $MoSi_2$.

The characteristic strength which could be obtained was 643.8 MPa for Si_3N_4 and 677.6 MPa for $MoSi_2$, with a Weibull modulus of 1.8 and 3.3, respectively. The low Weibull modulus of both series is a result of a wide range of critical flaws, which may be attributed to blocked or malfunctioning nozzles of the printheads. High characteristic strength on the one hand and low Weibull moduli on the other hand indicate that the reliability of the DIP process for the build-up of nonoxide ceramic parts has to be further enhanced. Hardness and fracture toughness of Si_3N_4 were determined as 15.1 GPa and 8.7 $MPam^{0.5}$, respectively, while in the case of $MoSi_2$ values of 10.8 GPa and 4.7 $MPam^{0.5}$ were achieved.

Si_3N_4 is used as material for structural ceramic parts with severe mechanical load. Prototype miniature gear wheels have been realized by successively printing 10 layers with a thickness of 8 μm, respectively (Figure 7(a)). While the surface of the sintered parts is flaw-free, the contours seem imperfectly rounded (Figure 7(b)). This, however, is not caused by errors during the DIP process but was induced by the transformation of the 3D model file to cross-sectional slices, which are necessary for the printing system [37].

Besides the field of structural ceramics, potential applications for Si_3N_4 are in the field of mechanical sensors (e.g., cantilevers), which is why pillar arrays, as demonstrated in Figure 8(a), were printed. By use of the DIP technology it is possible to place single droplets exactly on top of each other, to realize pillars or similar structures with heights up to 500 μm. The homogeneity of distance between single pillars as well as their uniformity is clearly noticeable [38]. Other functional parts which are interesting concerning the application of nonoxide ceramics are heating elements, for instance. Figure 8(b) shows a printed $MoSi_2$ heating element, consisting of 50 single layers, with good shape accuracy, although single misplaced drops were occasionally identified [38].

3.2. 2D-3D Patterns. As shown in Figure 9, micropillar arrays were printed with alumina ink.

To observe cell growth, primary structure elements (pillar/pillar or hollow/hollow) were printed with distances from 100 μm to 300 μm. These distances were chosen based on the fact that the cell size is of about 100 μm. To guarantee that cells on these substrates had the same microstructured environment all over the surface, it was crucial to ensure accuracy in distance between those microstructures. In Figure 10 it is evident that DIP is capable of producing such accurate structures.

3.3. Laminates of ZrO_2 and ZTA. Figure 11 shows a SEM micrograph of the cross-section of a printed multimaterial layered specimen perpendicular to the printing direction. The

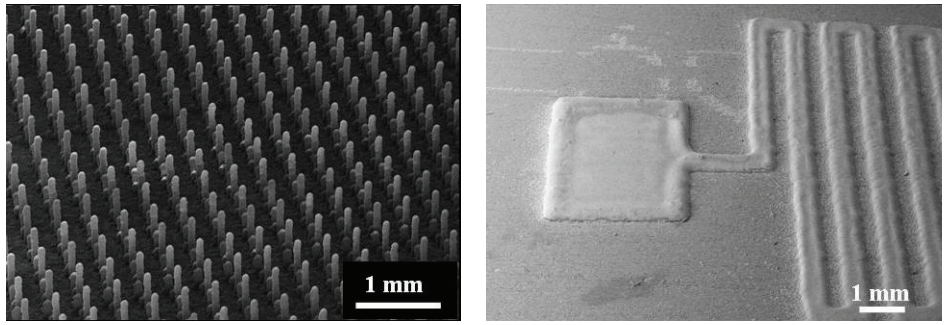

(a) (b)

Figure 8: SEM picture of Si_3N_4 micropillar array (a) [38]. Prototype of $MoSi_2$ heating element (b) [38].

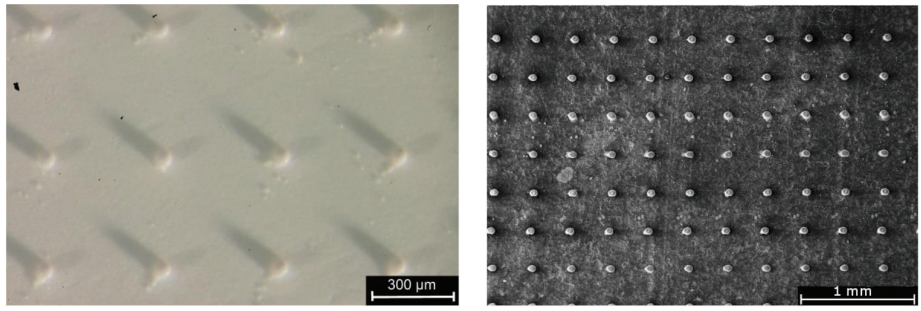

(a) (b)

Figure 9: Printed Al_2O_3 pillar arrays on a disc shaped Al_2O_3 substrate (a); SEM micrograph of a printed Al_2O_3 pillar array on a carbon substrate (b).

sample consists of successively printed layers of ZTA and 3Y-TZP (each consisting of 10 layers). While a clear distinction between 3Y-TZP (lighter) and ZTA (darker) is shown, the micrograph also clearly features the areas where clogged nozzles for ZTA caused grooves which were subsequently filled with 3Y-TZP. Further magnification shows good bonding between layers of the same material as well as at the interface between different materials (ZTA/3Y-TZP) (Figure 12). No cracks along the interface or delamination were detected.

3.4. Functionally Graded Materials. Both ceramic inks were reliably jettable and long term stable. Problems like nozzle clogging or kogation on heating elements were not observed, which is a prerequisite for flawless part production by DIP [48]. Exemplary rectangular FGM parts were produced by printing graded colour models of cyan (=ZrO_2) and yellow (=Al_2O_3) colours. Figure 13 shows the predefined colour gradient (a) and a central section of the surface of the resulting material gradient (b). The presented structure consists of 5 layers, which were printed on top of each other. The process was realized by the modified 3D printing system placing droplets of Al_2O_3 and ZrO_2 ink in direct juxtaposition. After deposition on the substrate the ink was immediately dried, which is why only a marginal mixing of droplets occurred. Nevertheless, it was possible to create smooth material transitions by using this colour printing mode, as shown in the corresponding SEM micrograph (Figure 13(c)).

The colour gradation was transformed into an almost stepless material transition. The lower limitation of step size is defined by the diameter of single droplets, as long as they are placed next to each other. By overlapping the droplets, even smoother transitions may be achievable. Compared to previous studies, where solids content was adjusted to values considerably above 25 vol%, the amount of solids of the inks was reduced to 21 vol% in the present study [41]. Contrary to descriptions in literature and to our own experience, this did not cause any drying problems like cracks or bulged layers [21]. The reason for this finding may be found in the printing system, which has been used in the actual study. The amount of ink, which is ejected by the printheads of this adapted powder bed printer, is reduced as compared to other printing systems, which have been used previously. This corresponds to reduced drying periods, which compensates the higher amount of volatile ink components, which evaporate during the drying process.

4. Conclusions

Small zirconia specimens of different shapes ("box with two movable matches") (Figure 4(a)), channel structure (Figure 4(b)), bridge framework (Figure 5), and rectangular test specimen (Figure 3) were successfully produced by DIP using a thermal inkjet printer. The prepared aqueous zirconia

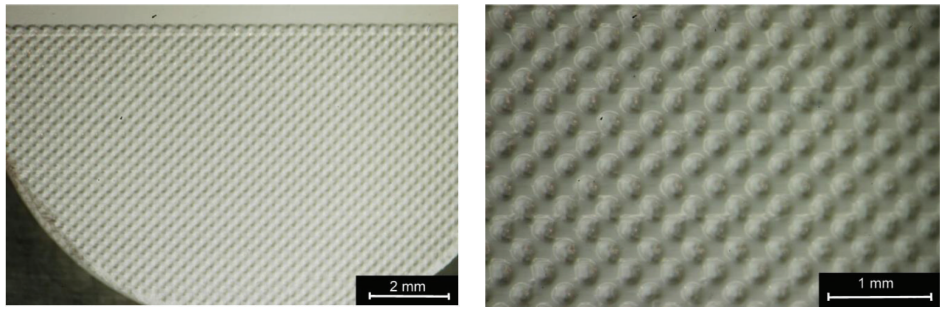

(a) (b)

Figure 10: Printed hollows with an Al_2O_3 suspension on a disc shaped Al_2O_3 substrate (a); magnification of the same printed structure (b).

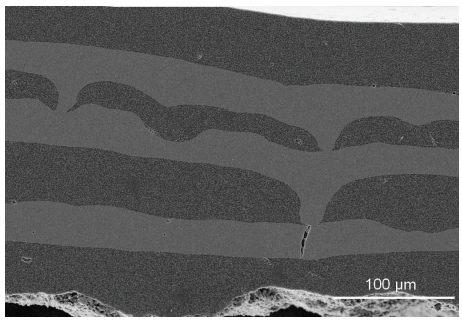

Figure 11: SEM micrograph of the cross-section of a printed multimaterial layered specimen.

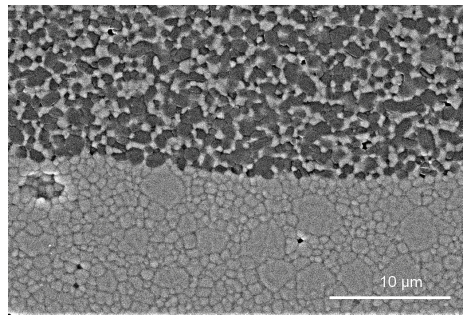

Figure 12: SEM micrograph of the cross-section at the interface of ZTA and 3Y-TZP.

suspension was characterized in terms of particle size distribution, viscosity, density, and surface tension, satisfying all physical requirements for the process. The suspension yielded solids content of 27 vol% and mechanical tests displayed a high B3B flexural strength (1393 MPa; $3 \times 4 \times 0.3\,\text{mm}^3$) and a fracture toughness of up to $8.9\,\text{MPam}^{0.5}$ without any optimization of the microstructure. Additionally, DIP allowed theoretical densities of about 97% to be achieved. It is apparent that the technology is suitable for the production of defect-free, high-strength ceramic components [34].

Furthermore, it has been shown that DIP is a promising technique to establish complex and accurate shaped structures with wall thicknesses of about 200 μm, as well as undercuts and enclosures. Additionally, it was possible to produce accurate structures as needed for in vitro cell tests with the aim of bioactivation of surfaces. Further steps, based on the subsequent observed cell reaction, should include the optimization of the chosen microstructure or even combinations of pillar arrays and printed hollows. Additional interest should be focused on the implementation of an additional y-axis, more parallel working printheads, and a specific printing software to satisfy the nozzle cleaning and deposit drying requirements [36].

Printed laminates of ZrO_2 and ZTA showed good bonding between layers of the same material as well as at the interface between different materials (ZTA/3Y-TZP). Further research should look into the mechanical properties of these layered samples as well as the use of different layer thicknesses or even interlocking structures to further enhance the mechanical properties.

Aqueous inks of Si_3N_4 and $MoSi_2$ with high solids content were developed and used to produce structural and functional parts by layerwise build-up via DIP. High green and sintered densities of printed components resulted in excellent mechanical characteristics. Low Weibull moduli for both materials, however, imply that further optimization of the process technology and material parameters is required. Enhanced reliability would unlock the enormous potential of DIP for the fast and flexible production of complex-shaped nonoxide ceramic parts [37, 38].

FGM structures were realized via DIP by specifically combining highly concentrated aqueous alumina and zirconia inks. The inks were ejected from different printheads on a modified powder bed printer, which allows the combination of single drops on a substrate. Graded structures starting from 100% alumina and 0% zirconia were built up to 0% alumina and 100% zirconia with a smooth material transition. The smoothness of transition is only limited by the droplet size, where a specific overlapping of single droplets could even increase this smoothness. The enormous potential of DIP for the production of FGM was confirmed in our study. The direct deposition of single, picolitre sized droplets, offers possibilities concerning spatially precise material composition, which are not attainable in this way by other shaping techniques at present. Limitations are not process but

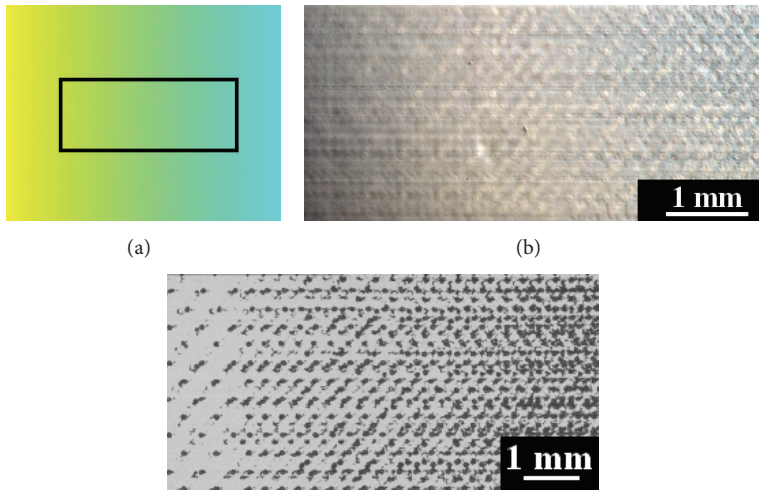

(a) (b)

(c)

FIGURE 13: Colour gradient from yellow (=Al_2O_3) to cyan (=ZrO_2) (a), surface of resulting printed green layers of Al_2O_3 and ZrO_2 (b), and corresponding SEM micrograph (c).

software related. A file format which includes compositional information inside the volume of a model is necessary to realize three-dimensional parts with material variations in each of the three spatial dimensions simultaneously. This is of utmost interest for many applications, such as bioceramics, where mechanical stress may differ significantly at different positions of one part. The possibility to locally adapt the material composition to this stress, using DIP, may result in substantially increased efficacy and efficiency.

Conflict of Interests

The authors declare that there is no conflict of interests regarding the publication of this paper.

Acknowledgments

The research was kindly supported by the Deutsche Forschungsgemeinschaft (DFG, TE 146/25-1) and in terms of an AiF sponsorship Program of the industriellen Gemeinschaftsforschung (IGF) by the Bundesministerium für Wirtschaft und Technologie (IGF-no. 493 ZN of the Forschungsgemeinschaft der Deutschen Keramischen Gesellschaft e.V.), which is gratefully acknowledged. The authors acknowledge Heraeus Kulzer (Hanau, Germany) for their kind support as well. Raul Bermejo, Marco Deluca, and Robert Danzer (ISFK, Montanuniversität Leoben, and Materials Center Leoben Forschung GmbH, Austria) are gratefully acknowledged for the ball-on-three-balls tests of zirconia specimens.

References

[1] "Standard terminology for additive manufacturing technologies," ASTM F2792-12a, 2012.

[2] E. Sachs, M. Cima, P. Williams, D. Brancazio, and J. Cornie, "Three dimensional printing. Rapid tooling and prototypes directly from a CAD model," *Journal of Engineering for Industry*, vol. 114, no. 4, pp. 481–488, 1992.

[3] U. Gbureck, T. Hölzel, U. Klammert, K. Würzler, F. A. Müller, and J. E. Barralet, "Resorbable dicalcium phosphate bone substitutes prepared by 3D powder printing," *Advanced Functional Materials*, vol. 17, no. 18, pp. 3940–3945, 2007.

[4] C. Bergmann, M. Lindner, W. Zhang et al., "3D printing of bone substitute implants using calcium phosphate and bioactive glasses," *Journal of the European Ceramic Society*, vol. 30, no. 12, pp. 2563–2567, 2010.

[5] D. L. Bourell, H. L. Marcus, J. W. Barlow, and J. J. Beaman, "Selective laser sintering of metals and ceramics," *International Journal of Powder Metallurgy*, vol. 28, no. 4, pp. 369–381, 1992.

[6] A. Gahler, J. G. Heinrich, and J. Günster, "Direct laser sintering of Al_2O_3-SiO_2 dental ceramic components by layer-wise slurry deposition," *Journal of the American Ceramic Society*, vol. 89, no. 10, pp. 3076–3080, 2006.

[7] A. M. Waetjen, D. A. Polsakiewicz, I. Kuhl, R. Telle, and H. Fischer, "Slurry deposition by airbrush for selective laser sintering of ceramic components," *Journal of the European Ceramic Society*, vol. 29, no. 1, pp. 1–6, 2009.

[8] M. Lindner, S. Hoeges, W. Meiners et al., "Manufacturing of individual biodegradable bone substitute implants using selective laser melting technique," *Journal of Biomedical Materials Research A*, vol. 97, no. 4, pp. 466–471, 2011.

[9] F. Doreau, C. Chaput, and T. Chartier, "Stereolithography for manufacturing ceramic parts," *Advanced Engineering Materials*, vol. 2, no. 8, pp. 493–496, 2000.

[10] T. Chartier, C. Chaput, F. Doreau, and M. Loiseau, "Stereolithography of structural complex ceramic parts," *Journal of Materials Science*, vol. 37, no. 15, pp. 3141–3147, 2002.

[11] N. S. Leyland, J. R. G. Evans, and D. J. Harrison, "Lithographic printing of ceramics," *Journal of the European Ceramic Society*, vol. 22, no. 1, pp. 1–13, 2002.

[12] K. Cicha, Z. Li, K. Stadlmann et al., "Evaluation of 3D structures fabricated with two-photon-photopolymerization by

using FTIR spectroscopy," *Journal of Applied Physics*, vol. 110, no. 6, Article ID 064911, pp. 1–5, 2011.

[13] I. Grida and J. R. G. Evans, "Extrusion freeforming of ceramics through fine nozzles," *Journal of the European Ceramic Society*, vol. 23, no. 5, pp. 629–635, 2003.

[14] A. Bellini, L. Shor, and S. I. Guceri, "New developments in fused deposition modeling of ceramics," *Rapid Prototyping Journal*, vol. 11, no. 4, pp. 214–220, 2005.

[15] J. A. Lewis, J. E. Smay, J. Stuecker, and J. Cesarano, "Direct ink writing of three-dimensional ceramic structures," *Journal of the American Ceramic Society*, vol. 89, no. 12, pp. 3599–3609, 2006.

[16] K. Sun, T. S. Wei, B. Y. Ahn, J. Y. Seo, S. J. Dillon, and J. A. Lewis, "3D printing of interdigitated Li-ion microbattery architectures," *Advanced Materials*, vol. 25, no. 33, pp. 4539–4543, 2013.

[17] A. M. Sukeshini, P. Gardner, F. Meisenkothen et al., "Aerosol jet printing and microstructure of SOFC electrolyte and cathode layers," *ECS Transactions*, vol. 35, no. 1, pp. 2151–2160, 2011.

[18] S. Magdassi, *The Chemistry of Inkjet Inks*, World Scientific Publishing, River Edge, NJ, USA, 2010.

[19] U. Hilleringmann, *Mikrosystemtechnik*, Teubner, Wiesbaden, Germany, 1st edition, 2006.

[20] M. Lejeune, T. Chartier, C. Dossou-Yovo, and R. Noguera, "Ink-jet printing of ceramic micro-pillar arrays," *Journal of the European Ceramic Society*, vol. 29, no. 5, pp. 905–911, 2009.

[21] E. Özkol, J. Ebert, and R. Telle, "An experimental analysis of the influence of the ink properties on the drop formation for direct thermal inkjet printing of high solid content aqueous 3Y-TZP suspensions," *Journal of the European Ceramic Society*, vol. 30, no. 7, pp. 1669–1678, 2010.

[22] H. S. On, D. Edelhoff, and H. Fischer, "Vollkeramische Brückensysteme—Möglichkeiten und Grenzen," *Quintessenz Team-Journal*, vol. 34, pp. 435–441, 2004.

[23] H. J. Wenz, J. Bartsch, S. Wolfart, and M. Kern, "Osseointegration and clinical success of zirconia dental implants: a systematic review," *International Journal of Prosthodontics*, vol. 21, no. 1, pp. 27–36, 2008.

[24] M. Hisbergues, S. Vendeville, and P. Vendeville, "Zirconia: established facts and perspectives for a biomaterial in dental implantology," *Journal of Biomedical Materials Research B: Applied Biomaterials*, vol. 88, no. 2, pp. 519–529, 2009.

[25] K. Hayashi, T. Inadome, H. Tsumura, T. Mashima, and Y. Sugioka, "Bone-implant interface mechanics of in vivo bio-inert ceramics," *Biomaterials*, vol. 14, no. 15, pp. 1173–1179, 1993.

[26] J. Malmström, E. Adolfsson, L. Emanuelsson, and P. Thomsen, "Bone ingrowth in zirconia and hydroxyapatite scaffolds with identical macroporosity," *Journal of Materials Science: Materials in Medicine*, vol. 19, no. 9, pp. 2983–2992, 2008.

[27] J. G. B. Nebe, F. Lüthen, R. Lange, and U. Beck, "Cellular activity and biomaterial's surface topography," *Materials Science Forum*, vol. 539–543, no. 1, pp. 517–522, 2007.

[28] J. B. Nebe, L. Müller, F. Lüthen et al., "Osteoblast response to biomimetically altered titanium surfaces," *Acta Biomaterialia*, vol. 4, no. 6, pp. 1985–1995, 2008.

[29] J. Park, S. Bauer, K. von der Mark, and P. Schmuki, "Nanosize and vitality: TiO_2 nanotube diameter directs cell fate," *Nano Letters*, vol. 7, no. 6, pp. 1686–1691, 2007.

[30] J. Ebert, E. Özkol, R. Telle, H. Fischer, and K. Uibel, "Direct inkjet printing: a versatile method of complex shape manufacturing," in *Proceedings of the 10th International Conference of the European Ceramic Society*, pp. 466–469, Göller, Baden-Baden, Germany, 2007.

[31] E. Özkol, "Rheological characterisation of aqueous 3Y-TZP inks optimized for direct thermal ink-jet printing of ceramic components," *Journal of the American Ceramic Society*, vol. 96, no. 4, pp. 1124–1130, 2013.

[32] Y. Miyamoto, W. A. Kaysser, and B. A. Rabin, *Functionally Graded Materials: Design, Processing and Applications*, Kluwer Academic, Dodrecht, The Netherlands, 2nd edition, 1999.

[33] X. He, H. Du, W. Wang, W. Jing, and C. Liu, "Fabrication of ZrO_2-SUS functionally graded materials by slip casting," *Key Engineering Materials*, vol. 368–372, pp. 1823–1824, 2008.

[34] E. Özkol, A. M. Wätjen, R. Bermejo et al., "Mechanical characterisation of miniaturised direct inkjet printed 3Y-TZP specimens for microelectronic applications," *Journal of the European Ceramic Society*, vol. 30, no. 15, pp. 3145–3152, 2010.

[35] J. Ebert, E. Özkol, A. Zeichner, B. Cappi, and R. Telle, *Tintenstrahldrucken als Multifunktionstechnologie—Herstellung von keramischen Mikrokomponenten*, Institut für Wissenschaftliche Veröffentlichungen, Jahresmagazin—Reihe Ingenieurwissenschaften Werkstofftechnologien, 2008.

[36] E. Özkol, W. Zhang, J. Ebert, and R. Telle, "Potentials of the "direct inkjet printing" method for manufacturing 3Y-TZP based dental restorations," *Journal of the European Ceramic Society*, vol. 32, no. 10, pp. 2193–2201, 2012.

[37] B. Cappi, E. Özkol, J. Ebert, and R. Telle, "Direct inkjet printing of Si_3N_4: characterization of ink, green bodies and microstructure," *Journal of the European Ceramic Society*, vol. 28, no. 13, pp. 2625–2628, 2008.

[38] B. Cappi, J. Ebert, and R. Telle, "Rheological properties of aqueous Si_3N_4 and $MoSi_2$ suspensions tailor-made for direct inkjet printing," *Journal of the American Ceramic Society*, vol. 94, no. 1, pp. 111–116, 2011.

[39] J. Ebert, E. Özkol, A. Zeichner et al., "Direct inkjet printing of dental prostheses made of zirconia," *Journal of Dental Research*, vol. 88, no. 7, pp. 673–676, 2009.

[40] E. Özkol, *Evaluation of the direct inkjet printing method for the fabrication of three-dimensional ceramic components [Dissertation]*, Fakultät für Georessourcen und Materialtechnik der Rheinisch-Westfälischen Technischen Hochschule Aachen, 2012.

[41] E. Özkol, J. Ebert, K. Uibel, A. M. Wätjen, and R. Telle, "Development of high solid content aqueous 3Y-TZP suspensions for direct inkjet printing using a thermal inkjet printer," *Journal of the European Ceramic Society*, vol. 29, no. 3, pp. 403–409, 2009.

[42] A. Börger, P. Supancic, and R. Danzer, "The ball on three balls test for strength testing of brittle discs: stress distribution in the disc," *Journal of the European Ceramic Society*, vol. 22, no. 9-10, pp. 1425–1436, 2002.

[43] A. Börger, P. Supancic, and R. Danzer, "The ball on three balls test for strength testing of brittle discs—part II: analysis of possible errors in the strength determination," *Journal of the European Ceramic Society*, vol. 24, no. 10-11, pp. 2917–2928, 2004.

[44] R. Danzer, W. Harrer, P. Supancic, T. Lube, Z. Wang, and A. Börger, "The ball on three balls test—strength and failure analysis of different materials," *Journal of the European Ceramic Society*, vol. 27, no. 2-3, pp. 1481–1485, 2007.

[45] N. N. Nemeth, J. M. Manderscheid, and J. P. Gyekenyesi, "Ceramics analysis and reliability evaluations of structures," (CARES) NASA Technical Paper 2916, Glenn Research Center, Cleveland, Ohio, USA, 1989.

[46] W. Weibull, "A statistical theory of the strength of materials," *Handlingar*, vol. 151, no. 1, pp. 1–45, 1939.

[47] G. R. Anstis, P. Chantikul, B. R. Lawn, and D. B. Marshall, "A critical evaluation of indentation techniques for measuring fracture toughness. I. Direct crack measurements," *Journal of the American Ceramic Society*, vol. 64, no. 9, pp. 533–538, 1981.

[48] J. H. Lim, K. Kuk, S. J. Shin et al., "Investigation of realiability problems in thermal inkjet printhead," in *Proceedings of the 42nd Annual International Realiability Physics Symposium*, vol. 1, pp. 251–254, April 2004.

Hindawi Publishing Corporation
Advances in Mechanical Engineering
Volume 2014, Article ID 648562, 9 pages
http://dx.doi.org/10.1155/2014/648562

Research Article

Mathematical Model for the Selection of Processing Parameters in Selective Laser Sintering of Polymer Products

Ana Pilipović,[1] Igor Drstvenšek,[2] and Mladen Šercer[1]

[1] *Faculty of Mechanical Engineering and Naval Architecture, University of Zagreb, Ivana Lučića 5, 10000 Zagreb, Croatia*
[2] *Faculty of Mechanical Engineering, University of Maribor, Smetanova ulica 17, 2000 Maribor, Slovenia*

Correspondence should be addressed to Ana Pilipović; ana.pilipovic@fsb.hr

Received 2 January 2014; Accepted 24 February 2014; Published 27 March 2014

Academic Editor: Cynthia Gomes

Additive manufacturing (AM) is increasingly applied in the development projects from the initial idea to the finished product. The reasons are multiple, but what should be emphasised is the possibility of relatively rapid manufacturing of the products of complicated geometry based on the computer 3D model of the product. There are numerous limitations primarily in the number of available materials and their properties, which may be quite different from the properties of the material of the finished product. Therefore, it is necessary to know the properties of the product materials. In AM procedures the mechanical properties of materials are affected by the manufacturing procedure and the production parameters. During SLS procedures it is possible to adjust various manufacturing parameters which are used to influence the improvement of various mechanical and other properties of the products. The paper sets a new mathematical model to determine the influence of individual manufacturing parameters on the polymer product made by selective laser sintering. Old mathematical model is checked by statistical method with central composite plan and it is established that old mathematical model must be expanded with new parameter beam overlay ratio. Verification of new mathematical model and optimization of the processing parameters are made on SLS machine.

1. Introduction

Additive manufacturing allows production of parts of very complex shapes, the making of which had been limited until these procedures were developed. Additive procedures are being intensively developed from day to day. Here the number of available materials is limited. Material properties differ a lot from the properties of the materials of finished products. Therefore, it is necessary to know the mechanical properties of the product material [1]. In selecting the processing procedures it is necessary to take into consideration four criteria: the desired material, size and number of products, time of manufacturing, and cost of production [2].

Prototypes made by selective laser sintering (SLS) are increasingly used as products, which means that they have to have high dimensional accuracy. However, accuracy is difficult to predict, since it depends on many parameters: accuracy of STL model in conversion from CAD model, cutting into layers, machine resolution, beam offset, layer thickness, material shrinkage, laser beam speed, laser power, temperature of working platform, and hatch distance.

Laser parameters can be used to affect the sintering procedure and the properties of the manufactured product. The quality of the surface, mechanical properties, dimensional accuracy, and time of manufacturing are the most common reason for the need to change the parameters. The parameters can be changed separately for the contour (external layers), that is, the product hatching (product interior). Improved connection of particles (sintering), as well as the mechanical properties, is affected by the energy density of the laser beam not only on the external layers, but also in the interior. According to many past studies the energy density depends on the power and speed of the laser beam and on the hatch distance or on the laser beam diameter, which is calculated according to the following equation: [3–8]

$$ED = \frac{P}{v \cdot h}, \qquad ED = \frac{P}{v \cdot d}, \tag{1}$$

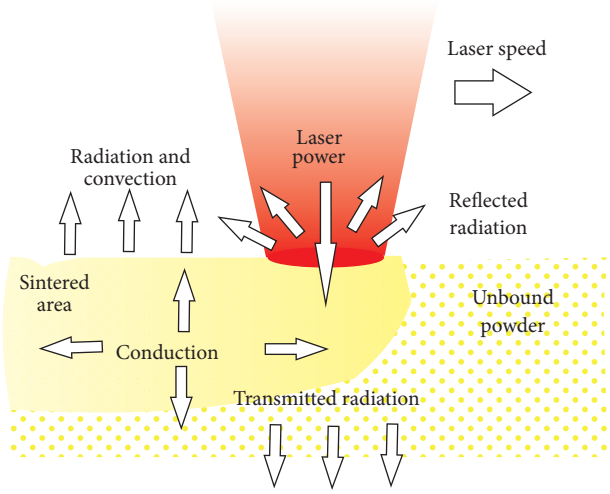

Figure 1: Impact of laser beam on the material [12].

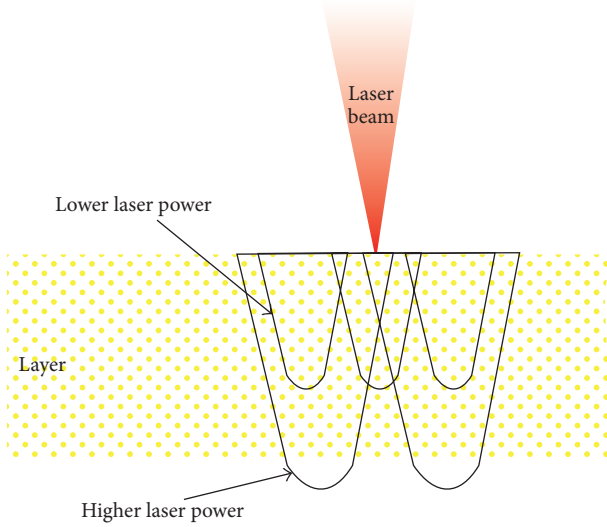

Figure 2: Power selection depending on the layer thickness.

where ED [J/mm^2] is the energy density, P [W] is the laser power, v [mm/s] is the laser beam speed, h [mm] is the hatch distance, and d [mm] is the laser beam diameter.

The value of the laser power during the sintering procedure depends on the type of material and the thickness of layer which is applied by the levelling roller. Laser power and laser beam speed during the making of the contour are somewhat lower in relation to the power and speed during the making of the hatching of individual layer. By changing the laser beam speed, the energy input into the material and the time of product manufacturing are changed as well [5–9].

2. Selective Laser Sintering

In SLS procedure the laser beam is directed by a mirror and marks the cross-section of the product on the powdery material located on the working base. Under the action of the laser beam thermal energy the powdery material softens and this results in mutual sintering of material particles and fusion of the newly applied layer of powder with the previously sintered layer [5, 10, 11].

Apart from the melting of new powder particles, in the next layer the laser beam has to sinter at the same time this new layer with the already existing one. Because of different thicknesses of the layers and the possibility of using several types of materials of different thermal conductivity on SLS equipment, it is necessary to ensure adequate energy density (ED) input by the laser beam in order to sinter the material at all and to connect this one with the previous layer (Figure 1). Since the layer thickness on the machine Formiga P100 is 0.1 mm the laser beam melts a somewhat thicker layer of powder and does it every time in every layer. In melting the powder volume is reduced. It is also necessary to set appropriate power for the layer thicknesses in order to avoid excessive sintering (Figure 2).

When applying the finish layer of the product, the levelling roller is used to apply several protective layers of powder (5 mm). The working chamber with the product is left in the machine for about 2 h, in order to let it cool gradually. The product is not yet suitable for handling, so it is left in powder outside the machine to let it cool completely to the room temperature. This influences the dimensional accuracy and reduction of heat deformations. Cooling of the product should take as long as the production does. After the product has cooled it can be taken out and cleaned from excess powder [6, 11].

2.1. Laser Parameters. Laser parameters can affect the sintering procedure and the properties of the product. Surface quality, mechanical properties, dimensional accuracy, and time of manufacturing the product are the most common reasons for changing the parameters. Parameters can be adjusted separately for contour and separately for the interior (hatching) of the product. The hatching parameters are the same as the contour parameters with different settings [6].

Laser Power. The amount of laser power P [W] during the sintering process depends on the type of material and the thickness of the layer which is applied by the levelling roller. In making of the contour the laser power is somewhat lower (approximately by 5 W) in relation to the power during the making of the layer hatching [6].

Laser Beam Speed (Scanning Speed). The speed of the laser beam v [mm/s] is also a parameter which can be regulated regarding the making of the contour or the product hatching. In making of the contour the speed of the laser beam is lower than in making of the hatching. With the change in the laser beam speed the energy input in the material and the time of making of the product are changed as well [6].

Laser Beam Diameter. In SLS procedures the laser beam is directed downwards with a certain diameter and it radiates the powder surface. The beam diameter d of the Formiga P100 machine of the company *EOS* is 0.42 mm. However,

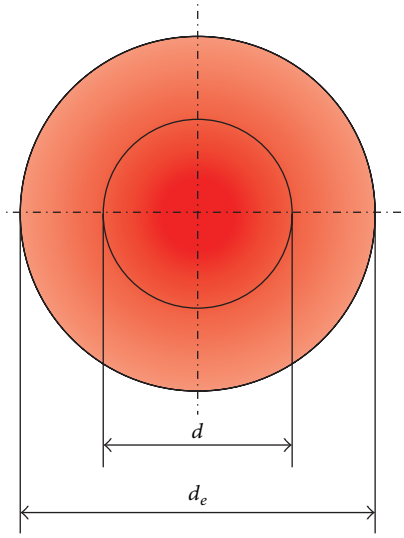

Figure 3: Physical d and effective d_e diameter of the laser beam [6].

the diameter of the area in which the particles are sintered is somewhat larger than the physical diameter of the beam (effective sintering diameter d_e) (Figure 3) [6].

Since the laser power and the speed of the laser beam are different in making of the contour, that is, hatching of the product, there is also difference in d_e of the contour, that is, of the hatching ($d_{ek} \neq d_{ej}$). For easier presentation, the effective and physical diameters of the laser beam are presented as a circle. Their actual appearance depends on x and y rotation of the scanning mirror [6].

Hatch Distance. Hatch distance h is presented in Figure 4. If the hatch distance is greater than the laser beam diameter between the laser runs some unsintered material remains.

3. Experimental Part

3.1. Tensile Properties Depending on the Adjustment of Parameters for the Contour of the Product. Parameters can be adjusted separately for the contour and separately for the product hatching. In the first phase of verifying the previous equation the parameters have been changed (Table 1) for the product contour and the influence of these parameters on tensile strength, yield strength, and elongation at break has been determined. The test (Figure 5) leads to the conclusion that mechanical properties vary slightly, concluding that due to the larger surface (i.e., volume) the hatching parameters rather than the contour parameters have greater influence on the product properties. The test specimens have been made with a layer thickness of 0.1 mm.

For determining the mechanical properties the *Messphysik Beta 50-5* testing machine is used. The control unit is an EDC 100, with a maximum loading force of 50 kN. The testing was carried out at the temperature of 23°C. For determining the tensile properties the test specimen is clamped by the jaws of the tensile testing machine and extended with force F, at speed v = 5 mm/min, as defined by standard ISO 527:2012.

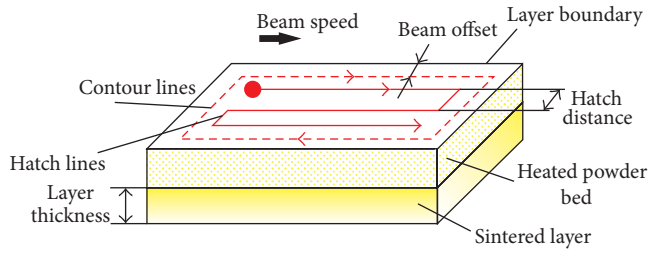

Figure 4: Hatch distance [13].

For the testing of flexural properties, the test specimen has to be supported by two supports and loaded in the middle by force F according to standard ISO 178: 2011. The testing speed was v = 5 mm/min.

3.2. Properties Depending on the Adjustment of Parameters for the Hatching of the Product. According to the available literature the main hatching parameter which affects the product properties is the energy density ED, which is calculated according to (1).

Due to contradictory opinion in the studied literature preexperiments were carried out and they are used to determine the dependence of single parameters.

For the experiment the central composite plan which allows modelling of polynomial of the second order and the shape of the response surface has been selected. The experiment determined the influence of three parameters (laser power, speed of the laser beam, and hatch distance) on mechanical properties (tensile and flexural strength) of the product obtained by SLS procedure. Software program *Design Expert* by module ANOVA (variance analysis) has been used.

The experiments were carried out with material PA 12, that is, PA 2200, with other processing parameters as follows:

(i) chamber temperature 172°C;

(ii) layer thickness 0.1 mm;

(iii) beam offset 0.15 mm;

(iv) material shrinkage along x axis 3.4%, along y axis 3.4%, and along z axis at 0 mm 2.2% to z axis at 300 mm 1.6%;

(v) alternating scanning direction;

(vi) included compensation of laser beam speed.

Before the experiment, a preexperiment was performed to determine the lower and upper limit of the following factors.

A: laser power, P = 5–25 W.

B: laser beam speed, v = 1000–3333 mm/s.

C: hatch distance, h = 0.15–1.6 mm.

It is necessary to carry out 19 experiment conditions (condition in the centre was repeated five times). The levels of factors (Table 2) have been determined according to the

Table 1: Relation of parameters for setting the contour of the product and mechanical properties.

Number	Laser power P, W	Laser speed v, mm/s	Tensile strength R_m, MPa	Tensile stress at break R_p, MPa	Tensile strain at break ε_p, %
1	16	1000	47.01	45.01	29.13
2	16	1500	46.87	44.89	32.04
3	14	1500	47.67	44.73	27.18
4	15	1500	47.99	44.28	33.98
5	17	1500	47.93	43.74	32.04
6	18	1500	47.88	43.55	33.01
7	19	1500	47.90	42.35	31.07
8	20	1500	47.18	43.95	26.21
9	16	2000	46.93	45.44	29.13

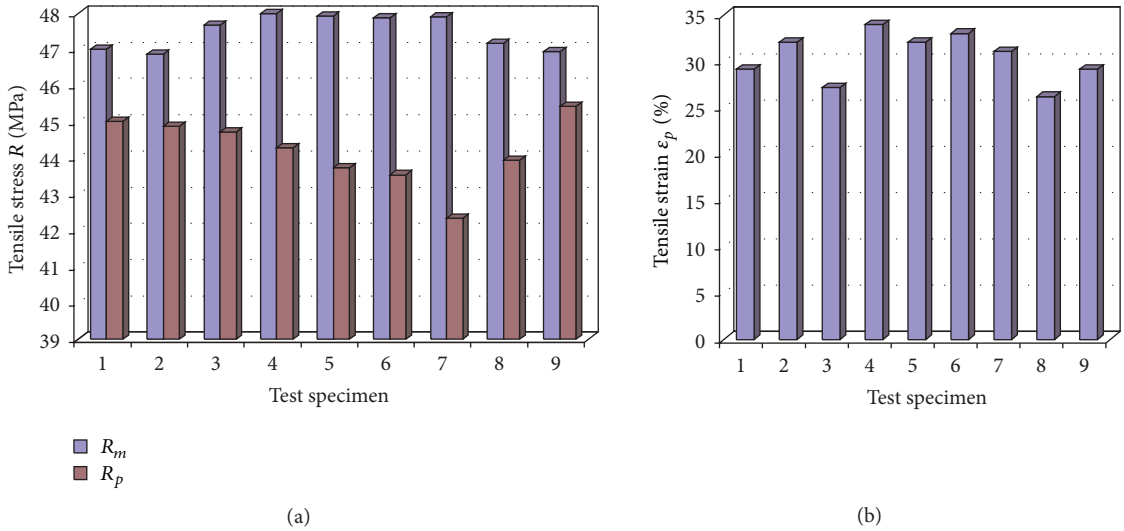

Figure 5: Tensile properties depending on the adjustment of parameters for the contour of the product: (a) tensile stress and (b) tensile strain.

Table 2: Levels of factors.

Levels	Laser power P, W	Laser beam speed v, mm/s	Hatch distance h, mm
−1.682	5	1023	0.16
−1	9	1500	0.45
0	15	2200	0.88
1	21	2900	1.30
1.682	25	3377	1.59

experiment condition matrix for the central composite experiment plan with two factors. Table 3 shows the results of the mean values of the mechanical properties. The linear curve for all properties has been selected as the approximation curve.

The experiment under number 11 was immediately excluded from the analysis since it is not possible to make the test specimen with these parameters, that is, such low energy density.

Experiments numbered 3 and 15 have been excluded from further analysis since the analysis showed that the response in these points does not correspond to the model; that is, there are too large deviations of the strength values from other data.

3.2.1. Tensile Strength. Table 4 shows the results of the processing for tensile strength R_m. In this case factor C, the hatch distance, is a significant factor (i.e., it affects the change of the tensile strength). In order for a certain factor to affect the change, the value in Table 4 in the last column should be smaller than 0.05.

Table 5 shows the basic statistical data about the model. The R-squared (r^2) is the measure of deviation from the arithmetic mean which is explained by the model. The closer r^2 is to 1, the better the model follows the data. The calculation is done according to [14]

$$r^2 = 1 - \frac{\text{SSDresidual}}{\text{SSDmodel} + \text{SSDresidual}}, \quad (2)$$

where r^2 is the R-squared and SSD is the sum of square deflection.

From the table it can be concluded that the deviation from the model is very large; that is, there is only 0.01% that the corresponding analysis follows the model.

Table 3: Measuring results.

Run	Factor A: laser power P (W)	Factor B: laser beam speed v (mm/s)	Factor C: hatch distance h (mm)	Tensile strength R_m (MPa)	Flexural strength σ_{fm} (MPa)
1	15	2200	0.88	3.76	8.00
2	9	1500	1.30	2.12	3.56
3	**15**	**2200**	**0.16**	**36.1**	**45.09**
4	5	2200	0.88	2.05	3.39
5	21	1500	1.30	3.50	7.59
6	15	2200	0.88	4.08	8.45
7	21	2900	1.30	2.43	6.55
8	15	2200	0.88	3.80	8.23
9	15	2200	0.88	3.85	8.12
10	21	2900	0.45	19.01	33.00
11	**9**	**2900**	**1.30**		
12	25	2200	0.88	5.12	9.57
13	9	1500	0.45	18.56	32.67
14	15	2200	0.88	4.00	8.01
15	**21**	**1500**	**0.45**	**43.1**	**62.32**
16	15	3377	0.88	3.08	7.31
17	9	2900	0.45	5.15	9.88
18	15	2200	1.59	1.95	3.20
19	15	1023	0.88	8.52	15.60

Table 4: Results of the variance analysis—tensile strength.

	Sum of squares	Degrees of freedom DF	Mean square	F value	Risk of rejection of H_0 (Prob. > F)
Model	245.43	3	81.81	5.32	0.0146
A	28.11	1	28.11	1.83	0.2014
B	34.71	1	34.71	2.26	0.1589
C	238.93	1	238.93	15.53	0.0020
Residual	184.60	12	15.38		
Lack of fit	184.53	8	23.07	1238.77	<0.0001 significant
Pure error	0.074	4	0.019		
Cor total	430.03	15			

Prob. > F: is the risk of rejection of hypothesis H_0.
Cor Total: is the sum of squares in model.

Table 5: Overview of statistical data about the model for tensile strength.

	Tensile strength
Standard deviation	3.92
Mean	5.69
Coefficient of determination (R-squared (r^2))	0.5707

Table 6: Regression coefficients for tensile strength.

Factor	Coefficient estimate	Standard error	95% Cl	
			Low	High
Intercept	6.27	0.99	4.11	8.43
A—laser power	1.62	1.2	−0.99	4.24
B—laser beam speed	−1.81	1.2	−4.42	0.81
C—hatch distance	−5.53	1.4	−8.58	−2.47

Figure 6 shows the dependence of the tensile strength on the speed of the laser beam and the hatch distance. The power which was shown by the experiment to have the least effect on the tensile strength was taken as a constant and amounts to $P = 21$ W. Graphical presentation of the dependence of tensile strength on the laser power and the hatch distance is similar to the diagram in Figure 6 and has not been presented separately.

From Figure 6 it may be concluded that with the decrease in the speed of the laser beam and the hatch distance the tensile strength is increased, although the R-squared shows that the model does not fully follow the data; that is, the tensile strength is also affected by some other influencing factors that have not been included in this preexperiment.

Table 7: Coded values for factors A, B and C.

Laser power—A		Laser beam speed—B		Hatch distance—C	
Actual value, W	Coded value	Actual value, mm/s	Coded value	Actual value, mm	Coded value
9	−1	1500	−1	0.45	−1
11	−0.67	1733	−0.67	0.59	−0.67
13	−0.33	1967	−0.33	0.73	−0.33
15	0	2200	0	0.88	0
17	0.33	2433	0.33	1.02	0.33
19	0.67	2667	0.67	1.16	0.67
21	1	2900	1	1.30	1

Table 8: Results of the variance analysis—flexural strength.

	Sum of squares	Degrees of freedom DF	Mean square	F value	Risk of rejection of H_0 (Prob. > F)
Model	734.93	3	244.98	5.85	0.0106
A	103.38	1	103.38	2.47	0.1420
B	88.90	1	88.90	2.12	0.1706
C	714.38	1	714.38	17.07	0.0014
Residual	502.16	12	41.85		
Lack of fit	502.02	8	62.75	1810.00	<0.0001 significant
Pure error	0.14	4	0.035		
Cor total	1237.10	15			

Table 9: Overview of statistical data about the model for flexural strength.

	Flexural strength
Standard deviation	6.47
Mean	10.82
Coefficient of determination (R-squared (r^2))	0.5941

According to the regression coefficients mentioned in Table 6, the model for tensile strength can be described by (3) in the coded form and with (4) in actual factors:

$$y = 6.27 + 1.62 \cdot A - 1.81 \cdot B - 5.53 \cdot C \quad (3)$$

$$y = 19.257 + 0.271 \cdot \text{power} - 2.579 \cdot 10^{-3} \cdot \text{speed} - 13.003 \cdot \text{hatch}. \quad (4)$$

For example, for $A = 21$ W (coded value = 1), $B = 2667$ mm/s (coded value = 0.67), and $C = 0.45$ mm (coded value = −1), expected value of the tensile strength will be 12.21 MPa.

Table 7 presents the coded values of the experiment factors for the tested area.

3.2.2. Flexural Strength. Table 8 shows the results of processing for the flexural strength. The table leads to the conclusion that in this case as well the only influencing factor is the hatch distance, whereas the laser power and the laser beam speed have the same impact. However, as in the case of tensile strength the deviation from the model is too large and some other model or some other parameters that can reduce the deviation are necessary. Table 9 shows the statistical data.

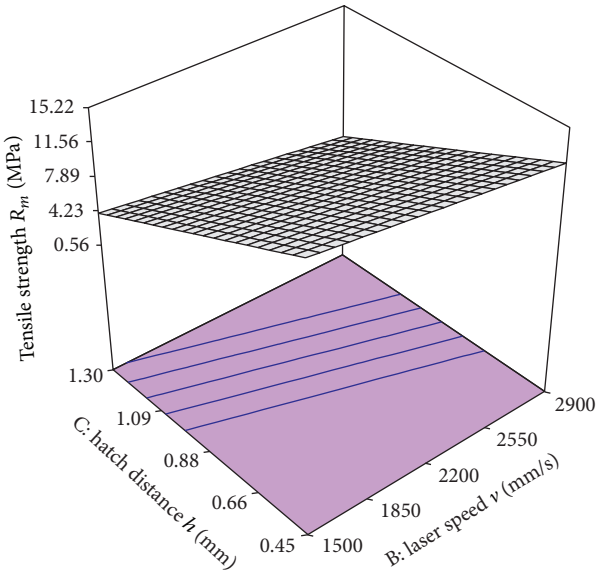

Figure 6: Dependence of tensile strength on the laser beam speed and the hatch distance at constant power.

Figure 7 shows the dependence of the flexural strength on the laser beam speed and the hatch distance. In this case as well the constant power $P = 21$ W has been taken. The graphical presentation of the dependence of the flexural strength on the laser power and the hatch distance is similar to the diagram in Figure 7 and has not been presented separately.

It may be concluded from the figure that by reducing the laser beam speed and the hatch distance the flexural strength

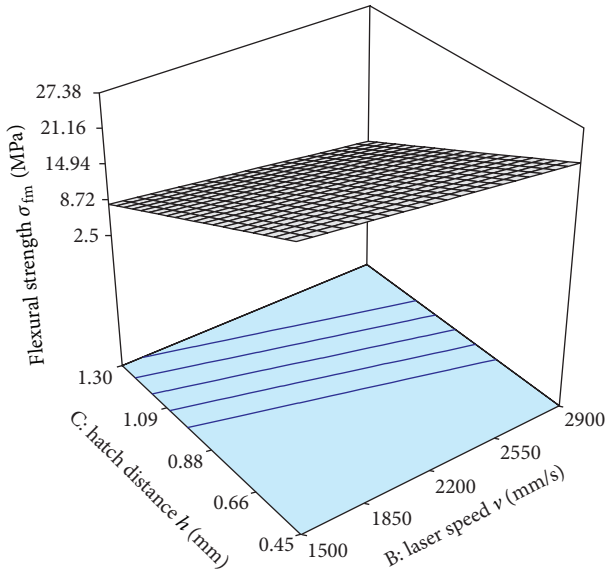

Figure 7: Dependence of flexural strength on the laser beam speed and the hatch distance at constant power.

is increased, although in this case as well the R-squared shows that the model does not fully follow the data, that is, that the flexural strength is also affected by other influencing factors that have not been included in this preexperiment.

According to the regression coefficients mentioned in Table 10, the model for flexural strength can be described by (5) in the coded form and by (6) in the actual factors:

$$y = 11.83 + 3.12 \cdot A - 2.89 \cdot B - 9.56 \cdot C, \tag{5}$$

$$y = 32.79 + 0.52 \cdot \text{power} - 4.13 \cdot 10^{-3} \cdot \text{speed} - 22.48 \cdot \text{hatch}. \tag{6}$$

For example, for $A = 21$ W (coded value = 1), $B = 1500$ mm/s (coded value = −1), and $C = 0.45$ mm (coded value = −1), expected value of the flexural strength will be 27.4 MPa.

The coded values of the experiment factor for the flexural strength are the same as for the tensile strength according to Table 7.

In order to reduce the deviation from the model and for the tensile and flexural strength many analyses have been carried out, but not one has proven to be appropriate, which leads to the conclusion that the parameters depend on each other, that is, that for the mechanical properties of the product there are factors which failed to be included in this model.

4. The Influence of Processing Parameters on the Product Properties

It was found from the conducted preexperiment that the parameters depend on each other and that there are still some other factors that affect the mechanical properties of the product, so that it may be concluded that it is necessary to set a new equation for the calculation of the energy density. The

Table 10: Regression coefficients for flexural strength.

Factor	Coefficient estimate	Standard error	95% Cl	
			Low	High
Intercept	11.83	1.64	8.26	15.39
A—laser power	3.12	1.98	−1.20	7.43
B—laser beam speed	−2.89	1.98	−7.21	1.43
C—hatch distance	−9.56	2.31	−14.60	−4.52

equation of the energy density ED should be expanded by the beam overlay ratio x which includes in itself the diameter of the laser beam and the hatch distance:

$$ED = \frac{P}{v \cdot h} \cdot x, \tag{7}$$

where ED [J/mm^2] is the energy density, P [W] is the laser power, v [mm/s] is the laser beam speed, h [mm] is the hatch distance, and x is the beam overlay ratio which is calculated according to

$$x = \frac{d}{h}, \tag{8}$$

where d [mm] is the laser beam diameter. On the machine Formiga P100 where measurements were conducted d is constant ($d = 0.42$ mm).

Figure 8 explains the new proposed equation for the influence of the parameters on the properties of the product; that is, it shows the scheme of scanning the powder particles by laser beam with the marked laser beam diameter d and the hatch distance h. At $h < d$ (Figure 8(a)) there is excessive overlay (greater factor x), where the value of energy density is also too high, and this results in the reduction of mechanical properties; however, at $h > d$ (Figure 8(b)) there remains unsintered powder and a mesh-like structure is achieved, so that a better case is the higher beam overlay ratio, that is, smaller hatch distance. Also, the beam overlay ratio should not be too large since this results in longer time of production.

Based on the conducted experiments it is proposed to take on the machine Formiga P100 the value of energy density $ED = 0.05$ J/mm^2 for the manufacturing of products of good mechanical properties with a layer thickness of 0.1 mm. The new equation is confirmed by the orientation of the test specimens of 0°, 90° with a height of 10 mm and 80 mm for flexural properties and 150 mm for tensile properties.

However, it is difficult to select which value of laser power, laser beam speed, and hatch distance should be taken into consideration in order to obtain adequate energy density ED. Thus, Figure 9 shows the proposal of selecting the parameter in energy density 0.05 J/mm^2 for Formiga P100, which can be also implemented for other machines used for SLS procedure.

5. Conclusion

During the process of making the product, using the selective laser sintering, it is possible to set various parameters that affect the properties of the final product. During the

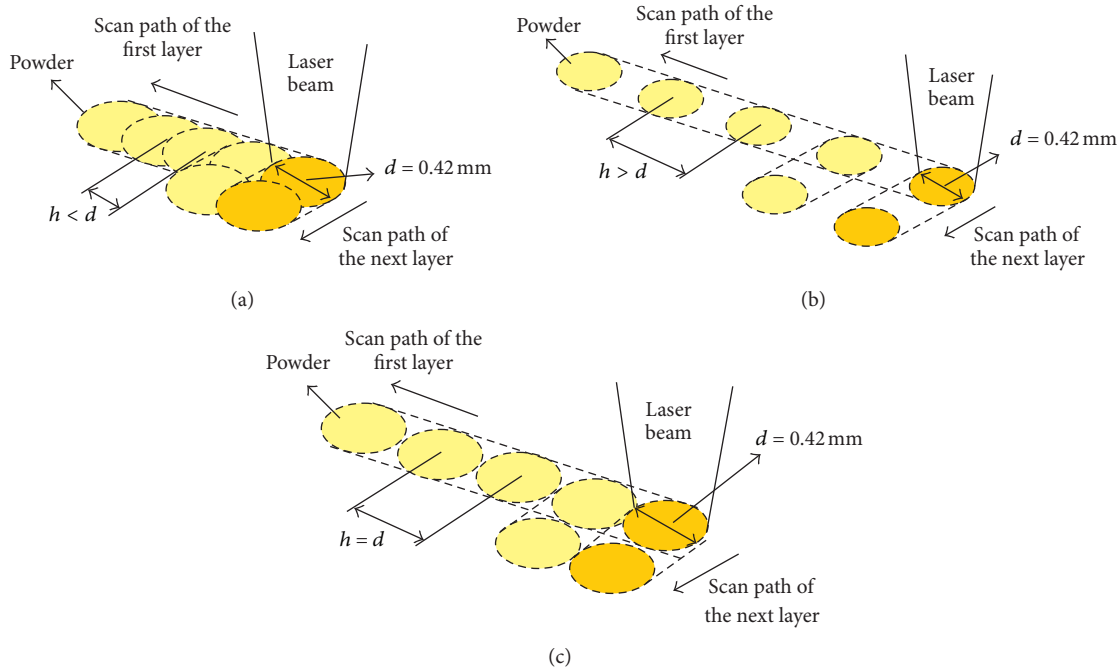

FIGURE 8: Scheme of the powder particles sintering: (a) $h < d$, (b) $h > d$, and (c) $h = d$.

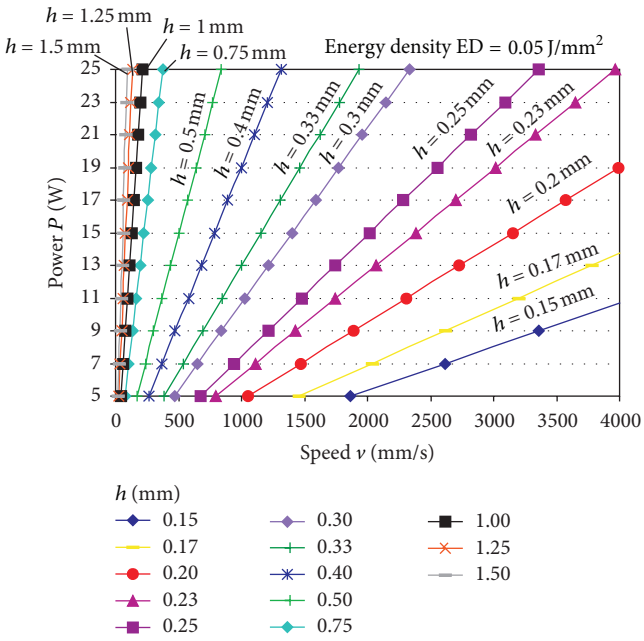

FIGURE 9: Determination of SLS procedure parameters at layer thickness 0.1 mm and energy density $ED = 0.05$ J/mm^2.

manufacturing one can thus adjust separately the parameters that make the contour and separately those that make the hatching of the product. From the conducted analysis it can be noticed that the mechanical properties are more affected by the parameters for adjusting the hatching of the product.

Past experiments were based on the equation for the hatching which connects the energy density with the laser power, laser beam speed, and hatch distance.

By implementing the central composite plan of experiment an analysis has been made and one can notice that in mechanical properties the only influencing factor is the hatch distance. However, in mechanical properties there is great deviation from all the models and R-squared does not follow fully the data ($r^2 = 0.5$). In order to reduce the deviation from the models and for tensile and flexural strength many analyses have been carried out, but none has proven adequate, which leads to the conclusion that the parameters (power, speed, and hatch distance) depend on each other, that is, that the only relevant parameter for the product property is energy density and that there are factors that are not included in this model (e.g., laser beam diameter, beam shift, shrinkage coefficient, manufacturing strategy, etc.).

Regarding the working principle of the SLS procedure (Section 2), apart from the parameters of power, speed, and hatch distance, the properties are also affected by the laser beam diameter, so that the previous equation for the calculation of energy density has to be expanded by the new factor, overlay ratio x.

If the hatch distance is smaller than the laser beam diameter ($h < d$) the overlay factor and the energy density are too large and the mechanical properties are reduced; there are excessive deviations from the nominal dimensions, and also the manufacturing time is longer. In the reverse case, when the hatch distance is greater than the laser beam diameter ($h > d$), there remains unsintered material and mesh-like structure is achieved. Such structure in some products has a positive property (e.g., lower mass), but all the products

should be additionally reinforced by some procedures, since the mechanical properties are not satisfactory.

Conflict of Interests

The authors declare that there is no conflict of interests regarding the publication of this paper.

Acknowledgments

This work is part of the research financed by the Croatian Science Foundation and project IPA III c, Additive Technologies for the SMEs (AdTecSME). It is also included in the project Increasing Efficiency in Polymeric Products and Processing Development, which is part of program Rapid Production—From Vision to Reality—supported by the Ministry of Science, Education and Sports of the Republic of Croatia. The authors would like to thank the Croatian Science Foundation, European Union, and the Ministry for the financing of this project.

References

[1] A. Pilipović, P. Raos, and M. Šercer, "Experimental analysis of properties of materials for rapid prototyping," *The International Journal of Advanced Manufacturing Technology*, vol. 40, no. 1-2, pp. 105–115, 2009.

[2] B. Valentan, T. Brajlih, I. Drstvenšek, and J. Balič, "Development of a part-complexity evaluation model for application in additive fabrication technologies," *Strojniški Vestnik—Journal of Mechanical Engineering*, vol. 57, no. 10, pp. 709–718, 2011.

[3] N. Raghunath and P. M. Pandey, "Improving accuracy through shrinkage modelling by using Taguchi method in selective laser sintering," *International Journal of Machine Tools & Manufacture*, vol. 47, no. 6, pp. 985–995, 2007.

[4] B. Caulfield, P. E. McHugh, and S. Lohfeld, "Dependence of mechanical properties of polyamide components on build parameters in the SLS process," *Journal of Materials Processing Technology*, vol. 182, no. 1–3, pp. 477–488, 2007.

[5] A. Pilipović, B. Valentan, T. Brajlih et al., "Influence of laser sintering parameters on mechanical properties of polymer products," in *Proceedings of the 3nd International Conference on Additive Technologies (iCAT '10)*, DAAAM International, 2010.

[6] Ö. İlkgün, *Effects of production parameters on porosity and hole properties in laser sintering rapid prototyping process [M.S. thesis]*, The Graduate School of Natural and Applied Sciences of Middle East Technical University, Ankara, Turkey, 2005.

[7] M. Schmidt, D. Pohle, and T. Rechtenwald, "Selective laser sintering of PEEK," *CIRP Annals—Manufacturing Technology*, vol. 56, no. 1, pp. 205–208, 2007.

[8] C. Yan, Y. Shi, J. Yang, and J. Liu, "Preparation and selective laser sintering of nylon-12 coated metal powders and post processing," *Journal of Materials Processing Technology*, vol. 209, no. 17, pp. 5785–5792, 2009.

[9] A. Pilipović, *Analysis of properties of material for rapid prototyping [diploma work]*, Faculty of Mechanical Engineering and Naval Architecture, Zagreb, Croatia, 2006.

[10] D. Godec, M. Šercer, and M. Rujnić-Sokele, "Influence of hybrid mould on moulded parts properties," *Rapid Prototyping Journal*, vol. 14, no. 2, pp. 95–101, 2008.

[11] I. Drstvenšek, N. I. Hren, T. Strojnik et al., "Applications of rapid prototyping in cranio-maxilofacial surgery procedures," *International Journal of Biology and Biomedical Engineering*, vol. 2, no. 1, pp. 29–38, 2008.

[12] A. Franco, M. Lanzetta, and L. Romoli, "Experimental analysis of selective laser sintering of polyamide powders: an energy perspective," *Journal of Cleaner Production*, vol. 18, no. 16–17, pp. 1722–1730, 2010.

[13] K. Senthilkumaran, P. M. Pandey, and P. V. M. Rao, "Influence of building strategies on the accuracy of parts in selective laser sintering," *Materials & Design*, vol. 30, no. 8, pp. 2946–2954, 2009.

[14] M. Rujnić-Sokele, "Influence of the stretch blow molding processing parameters on PET bottles properties," *Polimeri*, vol. 28, no. 4, pp. 213–292, 2007.